

Investigation of particle movement in irregularly shaped channels in inertial fluidics for scale up applications in bioprocessing

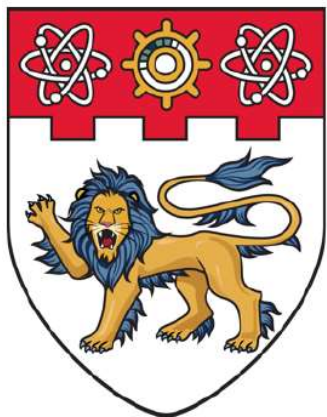
Moloudi, Reza

2019

Moloudi, R. (2019). Investigation of particle movement in irregularly shaped channels in inertial fluidics for scale up applications in bioprocessing. Doctoral thesis, Nanyang Technological University, Singapore.

<https://hdl.handle.net/10356/81393>

<https://doi.org/10.32657/10220/49092>



**NANYANG
TECHNOLOGICAL
UNIVERSITY**

SINGAPORE

**INVESTIGATION OF PARTICLE MOVEMENT IN
IRREGULARLY SHAPED CHANNELS IN INERTIAL
FLUIDICS FOR SCALE UP APPLICATIONS IN
BIOPROCESSING**

REZA MOLOUDI

SCHOOL OF MECHANICAL AND AEROSPACE ENGINEERING

2019

**INVESTIGATION OF PARTICLE MOVEMENT IN
IRREGULARLY SHAPED CHANNELS IN INERTIAL
FLUIDICS FOR SCALE UP APPLICATIONS IN
BIOPROCESSING**

REZA MOLOUDI

SCHOOL OF MECHANICAL AND AEROSPACE ENGINEERING

A thesis submitted to the Nanyang Technological University
in partial fulfilment of the requirement for the degree of
Doctor of Philosophy

2019

Statement of Originality

I hereby certify that the work embodied in this thesis is the result of original research, is free of plagiarised materials, and has not been submitted for a higher degree to any other University or Institution.

.....7 Jan 2019.....

Date

.....R. Moloudi.....

Reza Moloudi

Supervisor Declaration Statement

I have reviewed the content and presentation style of this thesis and declare it is free of plagiarism and of sufficient grammatical clarity to be examined. To the best of my knowledge, the research and writing are those of the candidate except as acknowledged in the Author Attribution Statement. I confirm that the investigations were conducted in accord with the ethics policies and integrity standards of Nanyang Technological University and that the research data are presented honestly and without prejudice.

Jan 7, 2019

Date

A handwritten signature in black ink, consisting of a stylized 'Y' and 'C' followed by a horizontal line, written over a dotted line.

Prof. Yang Chun, Charles

Authorship Attribution Statement

This thesis contains material from papers published/submitted in the following peer-reviewed journals where I was the first and/or corresponding author.

Chapter 3 is published as Reza Moloudi, Steve Oh, Chun Yang, Majid Ebrahimi Warkiani, and May Win Naing. Inertial particle focusing dynamics in a trapezoidal straight microchannel: Application to particle filtration. *Microfluidics and Nanofluidics*, 22:33 (2018).

The contribution of co-authors are as follows:

- I designed the experiment and carried out all of the laboratory works at the Bio-Manufacturing Lab (SIMTech) and also analyzed the data. I prepared the manuscript draft.
- The manuscript was revised by Dr. Steve Oh, Prof. Chun Yang, Dr. Majid. E. Warkiani and Dr. May Win Naing.

Chapter 4 is published as Reza Moloudi, Steve Oh, Chun Yang, Kim Leng Teo, Alan Tin-Lun Lam, Majid Ebrahimi Warkiani, and May Win Naing. Inertial-Based Filtration Method for Removal of Microcarriers from Mesenchymal Stem Cell Suspensions. *Scientific Reports*, 8, 12481 (2018).

The contribution of co-authors are as follows:

- I designed the experiment and carried out the laboratory works, and analysis related to cell/microcarrier separation at the Bio-Manufacturing Lab (SIMTech) and also analyzed the data. I prepared the main manuscript draft.
- Mr. Kim Leng Teo, Dr. Alan Tin-Lun Lam performed trilineage stem cell differentiation.
- The manuscript was revised by Dr. Steve Oh, Prof. Chun Yang, Dr. Majid. E. Warkiani and Dr. May Win Naing.

Chapter 5 is published as Reza Moloudi, Steve Oh, Chun Yang, Kim Leng Teo, Alan Tin-Lun Lam, Majid Ebrahimi Warkiani, and May Win Naing. Scaled-up Inertial Microfluidics: Retention System for Microcarrier-based Suspension Cultures. *Biotechnology Journal*, 14, 1800674 (2019).

The contribution of co-authors are as follows:

- I designed the experiment and carried out the laboratory works, and analysis related to cell-microcarrier retention at the Bio-Manufacturing Lab (SIMTech) and Stem Cell lab (BTI). I also analyzed the data and prepared the main manuscript draft.
- Mr. Kim Leng Teo, Dr. Alan Tin-Lun Lam assisted microcarrier cell culture and performed flow cytometry.
- The manuscript was revised by Dr. Steve Oh, Prof. Chun Yang, Dr. Majid. E. Warkiani and Dr. May Win Naing.

Chapter 6 is submitted as Reza Moloudi, Ali Mashhadian, Steve Oh, Chun Yang, Kim Leng Teo, Alan Tin-Lun Lam, Majid Ebrahimi Warkiani, and May Win Naing. Separation of Particulates Matter Contamination from Manufactured Cell Products by Inertial Microfluidics.

The contribution of co-authors are as follows:

- I designed the experiment and carried out the laboratory works, and analysis related to cell/particulates separation at the Bio-Manufacturing Programme (SIMTech) and also analyzed the data. I prepared and revised the main manuscript draft.
- Mr. Ali Mashhadian performed numerical modelling and wrote the numerical part.
- Mr. Kim Leng Teo, Dr. Alan Tin-Lun Lam performed trilineage differentiation and flow cytometry.

The manuscript was revised by Dr. Steve Oh, Prof. Chun Yang, Dr. Majid. E. Warkiani and Dr. May Win Naing.

.....7.Jan.2019
Date

.....R. Moloudi
Reza Moloudi

Abstract

Particle separation is a vital step in many analytical chemistry, biomedical diagnosis, and environmental applications. Inertial microfluidics has emerged in recent years as a promising tool for a wide range of flow cytometric tasks including cell separation, cell counting and mechanical phenotyping. In inertial fluidics, a transverse inertia-induced lift force across streamlines is inherently accompanied with higher order of magnitude convection mass transfer (channel Reynolds number >10), in contrast to microdevices working mainly based on diffusion mass transport phenomenon (Stokes flow) or low-Re flows, increasing throughput significantly. Emerging inertial focusing technique as an alternative method to microfiltration has brought remarkable benefits such as a continuous and clog-free system with lower maintenance costs. These features along with its relative ease of scalability to reach a relevant industrial scale will facilitate its potential adoption in various industries such as waste water treatment and bioprocessing. Of particular interest, dealing with a broader range of particle sizes up to one order of magnitude larger than cell sizes ($a > 50\text{ }\mu\text{m}$) in bioprocessing requires scaled-up channels to avoid clogging. However, Dean-coupled inertial focusing has not been studied in detail when the channel hydraulic diameter is greater than $D_H \approx 0.3\text{ mm}$.

Moreover, with the advancement of cell therapy industry in recent years, cell purification at downstream processing introduces some new challenges. While removing particulates from manufactured cell products, using routine membrane technologies similar to protein manufacturing industry do not work as well. This work focuses on the design and development of a membrane-less filtration and separation device using inertial focusing for a large range of particle sizes. To this end, inertial focusing is investigated in straight and mainly curved channels due to their scalability, throughput and efficiency.

Inertial focusing is profoundly reliant on the cross-sectional shape of channel and it affects not only the shear field but also the wall-effect lift force near the wall region. The wall-effect lift force is known as a determining factor for cross-lateral migration that leads to a reduced number of equilibrium positions. In order to investigate this, a rectilinear channel

with trapezoidal cross-section is designed to break down the symmetrical condition in conventional rectangular microchannels for a broad range of channel Re number ($20 < \text{Re} < 800$). The altered axial velocity profile and consequently new shear force arrangement leads to a cross-laterally movement of equilibration toward the longer side wall; however, the lateral focusing starts to move backward toward the middle and the shorter side wall, depending on particle clogging ratio, channel aspect ratio, and slope of slanted wall, as the channel Reynolds number further increased ($\text{Re} > 50$). Finally, a trapezoidal straight channel along with a bifurcation was designed and used for continuous filtration of a broad range of particle size ($0.3 < K < 1$) exiting through the longer wall outlet with $\sim 99\%$ efficiency ($\text{Re} < 100$). Nonetheless, though the linear structure of channel can be scaled out relatively easy to reach higher volumetric throughput, it inherently suffers from low particle concentration. Thus, further investigations focused on a curvature-induced secondary flow in conjunction with inertial lift.

The mechanism of Dean-coupled inertial focusing inside scaled-up rectangular and trapezoidal spiral channels (i.e., 5-10x bigger than conventional microchannels) is studied with an aim to develop a continuous and clog-free microfiltration system for bioprocessing. Scaling up channel hydraulic diameter one order of magnitude from ~ 0.1 mm (micron scale) to ~ 1 mm (millimeter scale) quenches the inertia of flow for a given channel Re number ($\text{Re} \leq 500$), resulting in deterioration of Dean-coupled inertial focusing ($D_H > \sim 1$ mm). Accordingly, different scaled-up trapezoidal spirals are developed to (i) filter cell-microcarrier complex (retention device) and (ii) separate microcarriers from cell suspensions. Further biological experimentation validates the applicability of the developed devices.

Since particulate contamination in GMP-grade biological products only exists at low concentrations, membrane-based filtration can eliminate large particulates without clogging. However, due to limitation on minimum screen size, particulates smaller than ~ 70 μm pass through the filter and end up in the manufactured cell products. To alleviate the particulates contamination, a scalable hybrid method using a combination of sieve and inertial-based separator is proposed as a generic method to remove particulates

contamination larger than cell sizes ranging from visible to subvisible. Hence, a large-aspect-ratio trapezoidal spiral channel is established and then implemented to remove subvisible particles down to 25 μm from a mesenchymal stem cell suspension possessing a diverse cell size ($10\ \mu\text{m} \leq a < 30\ \mu\text{m}$). Though the inertial-based separator can reduce the particulate burden in manufactured cell products, it is not a hundred percent reliable when the size of the particulate overlaps with that of cells. Thus, a combination of methods using inertial focusing together with active methods such as dielectrophoresis is needed to manipulate multi biophysical markers such as size and electrical properties.

Acknowledgements

I would like to express my sincere gratitude towards:

A*STAR Graduate Academy, for offering the prestigious SINGA scholarship.

Prof. Charles Chun Yang, for giving his thoughtful critique, advice and support throughout my project.

Dr. May Win Naing, for her endless support, advice, enthusiasm and kindness throughout the entire project. It really has been a true honor and privilege to work under her supervision. Without her support, it would not have been possible to conduct this research.

Dr. Steve Kah-Weng Oh, Dr. Majid Ebrahimi Warkiani and Dr. Thomas Hai-Qing Gong, for their support and advice.

Mr. Ahmad Amirul Bin Abdul Rahim, Dr. Deepak Choudhury, Dr. Liu Dan, Dr. Ying Ying Wu, Ms. Chaw Su Thwin and Ms. Seah Yen Peng Daphne from SIMTech-A*STAR, for rendering their help during the period of my attachment.

Prof. Shaul Reuveny, Dr. Allen Chen, Dr. Alan Lam, Mr. Teo Kim Leng, Ms. Eileen Sim, Ms. Fahima Jaleel khan from BTI-A*STAR, for useful discussion and cell culture training.

Table of Contents

Abstract	i
Acknowledgements	iv
Table of Contents	v
List of Tables	x
List of Figures	xi
Abbreviations	xx
Chapter 1 Introduction	1
1.1 Background and Motivation	1
1.2 Objective and Scope	4
1.3 Outline of the thesis	4
Chapter 2 Literature Review	7
2.1 Introduction	7
2.2 Inertial particle equilibrium phenomenon	8
2.3 Fundamental inertial forces	9
2.3.1 Shear-gradient lift force	12
2.3.2 Wall-Induced lift force	14
2.3.3 Secondary drag force	16
2.3.4 Miscellaneous lift forces	17
2.4 Inertial microfluidics channel structures	18
2.4.1 Straight channel	18
2.4.2 Curved channel	29
2.5 Downstream processing of stem cell therapy manufacturing and challenges	45
2.5.1 Stem cell therapy manufacturing	45
2.5.2 Microcarrier-based bioreactor	46

2.5.3 Particulates type in cell therapy industry	47
2.6 Summary	49
Chapter 3 Inertial Particle Focusing Dynamics in a Trapezoidal Straight Microchannel	51
3.1 Introduction.....	51
3.2 Theoretical Background.....	53
3.3 Materials and Methods.....	55
3.3.1 Design and Fabrication	55
3.3.2 Sample Preparation	55
3.3.3 Numerical Simulation	56
3.3.4 Experimental Setup and measurement.....	56
3.4 Results and Discussion	57
3.4.1 Inertial focusing in the trapezoidal straight channel with AR of 2	57
3.4.2 Inertial focusing in the trapezoidal straight channel with AR of 4.....	61
3.4.3 Particle filtration	65
3.5 Summary	69
Chapter 4 Inertial-Based Filtration Method for Removal of Microcarriers from Mesenchymal Stem Cell Suspensions	71
4.1 Introduction.....	71
4.2 Design Principle.....	73
4.3 Material and methods.....	76
4.3.1 Channel fabrication.....	76
4.3.2 Cell culture.....	77
4.3.3 Microcarrier and sample preparation	77
4.3.4 Device characterization.....	78
4.3.5 Cell characterization	79

4.4 Results and discussion	82
4.4.1 Microcarrier focusing dynamics in the scaled-up spirals	82
4.4.2 Removal of microcarriers from mesenchymal stem cell suspension.....	86
4.5 Summary	90
Chapter 5 Scaled-up Inertial Microfluidics: Retention System for Microcarrier-based Suspension Cultures.....	91
5.1 Introduction.....	91
5.2 Material and methods.....	94
5.2.1 Design and fabrication	94
5.2.2 Sample preparation	94
5.2.3 Cell culture.....	94
5.2.4 Cell-microcarrier characterization assay.....	95
5.2.5 Numerical simulations	96
5.2.6 Experimental setup.....	96
5.3 Results and discussion	97
5.3.1 Particle focusing dynamics in the scaled-up rectangular spiral channel.....	97
5.3.2 Particle focusing dynamics in the scaled-up trapezoidal spiral channel.....	102
5.4 Re-D _H operation map	105
5.5 Microcarrier concentration and/or filtration	107
5.6 Microcarrier-based suspension culture retention system.....	112
5.7 Summary	114
Chapter 6 High-throughput Separation of Particulates Matter Contamination from Manufactured Cell Products Using Inertial Microfluidics.....	115
6.1 Introduction.....	115
6.2 Material and methods.....	118

6.2.1 Microchannel design and fabrication.....	118
6.2.2 Cell culture and biological assays.....	118
6.2.3 Experimental setup and sample preparation	119
6.3 Results and discussion	121
6.3.1 Particle focusing.....	121
6.3.2 Removal of particulates using the trapezoidal spiral channel.....	123
6.3.3 Validation of harvested MSCs	126
6.4 Summary	128
Chapter 7 Conclusions and Future Work.....	129
7.1 Conclusions.....	129
7.1.1 Inertial focusing in trapezoidal straight channels	129
7.1.2 Inertial-based filtration method for removal of microcarriers from mesenchymal stem cell suspensions.....	130
7.1.3 Scaled-up inertial microfluidics: Retention system for microcarrier-based suspension cultures.....	130
7.1.4 Separation of particulates matter contamination from manufactured cell products by inertial microfluidics.....	131
7.2 Future Work	132
References.....	135
Appendices.....	147
Appendix A. Supplementary Information: inertial particle focusing dynamics in a trapezoidal straight microchannel	147
Appendix B. Supplementary Information: Inertial-based filtration method for removal of microcarriers from mesenchymal stem cell suspensions.....	152
Appendix C. Supplementary Information: Scaled-up Inertial Microfluidics: Retention System for Microcarrier-based Suspension Cultures.....	155

Appendix D. Supplementary Information: High-throughput Separation of Particulates Contamination from Manufactured Cell Products Using Inertial Microfluidics	164
--	-----

List of Tables

Table 2-1 Application of inertial microfluidics using a straight channel structure.....	25
Table 2-2 Application of Dean-coupled inertial microfluidics using a spiral, double spiral and U-shaped channel structure	41

List of Figures

Figure 2-1 (a) Experimental distribution of neutrally-buoyant particles over circular cross section for $D/a=9$ and $Re=134$ (b) corresponding probability function [63]..	8
Figure 2-2 Trains of particle for $D/d=19$ at $Re=1200$ in a circular channel [64]....	9
Figure 2-3 Schematic Rubinow and Keller force (Magnus effect) [68]	10
Figure 2-4 Spherical particle (a) Leading (b) lagging the fluid flow and its respective direction of Saffman forces [68].....	11
Figure 2-5 Curvature of velocity profile effect on particle and the corresponding shear-gradient lift force towards wall	12
Figure 2-6 Three different non-dimensional lift force based on (a) matched asymptotic theory and finite-sized particle approaching to (b) centerline (c) wall [75].....	13
Figure 2-7 Wall-induced lift force towards channel centerline	15
Figure 2-8 Schematic representation of secondary flow in a curved channel	17
Figure 2-9 (a) Particle focusing quality in rectangular channels with $AR=1/10-1$ as a function of particle Re number and clogging ratio $K=a/LC$ (unfocused particle flows are represented by circles, partially focused particle streams are represented by squares, and focused particle streams are represented by triangles. Filled markers represent flows with $Re>100$) (b) particle filtration in a low aspect ratio microchannel when particles equilibrated along sidewalls [37]	19
Figure 2-10 Lateral and cross-lateral particle migration in a square microchannel for different particle clogging ratios $K=a/H$ [98]	20
Figure 2-11 (a) Two-stage model of particle ordering in a high aspect ratio microchannel reveals effects of rotation-induced lift forces on particles located in corners, which conduct them towards center-wall equilibrium positions (b) Positive and negative lift coefficients for 10,15.5 and 20 μm as a function of Re in a low AR 50 $\mu m \times 100 \mu m$ channel [39] (c) dynamic of particle equilibrium positions by increasing Re flow for different clogging ratio K [79]	21

Figure 2-12 (a) High AR channel for cell/particle filtration [99] (b) modulated AR for complete separation of microparticles [36] and (c) single point particle focusing in a straight channel manipulating channel AR [101]. (d) variation of cross-sectional shape along the length for single focusing [102] and (e) particle/cell separation [103].	23
Figure 2-13 (a) Trapping larger particle/cell inside a chamber by utilizing vortices [105] (b) vortex-aided inertial microfluidic design by siphoning larger particle continuously [108] (c) continuous inertial separation of microparticles based on contraction-expansion structure inducing secondary flow (fluorescent image shows separation resolution between large (15 μm , white arrow) and small microparticle (7 μm , dark arrow)) [110] (d) enhancing inertial separation resolution by using high AR channel before the contraction-expansion segment [41].	27
Figure 2-14 (a) A 3-inlet co-flow system using inflection point focusing while larger particles migrated towards center under the influence shear-gradient force [115] (b) migration of 18.7 μm (green) spiked in whole blood from side streams towards sheath flow at center under the shear-induced diffusion lift force arouse from high concentration gradient [117] (c) Dimensionless Peclet-like number vs. particle Re number showing oscillatory inertial focusing at low $R_p < 0.1$ [116].	29
Figure 2-15 (a) A semicircle microchannel exploited to classify particles of a suspension [89] (b) inertial focusing by using a straight, symmetric and asymmetric microchannel [25] (c) discriminated routs of inner (blue) and outer (red) focused particles traveling along a single turn [122]	30
Figure 2-16 (a) Double spiral chip was functionalized for filtering of microparticles [123, 124] independently (b) segregating 1.9 μm (colored purple) from 7.32 μm (colored green) particles completely where flowing at $De = 0.47$ [33] shown by superimposed fluorescent images. (c) spiral microchannel for separating different-sized particles (10, 15 and 20 μm particle)[125]	33
Figure 2-17 (a) spiral microchannel designed for separating multi-particle size and its width is increasing along the spiral route (b) Focusing map based on particle diameter to channel height Vs. De number while solid square shows focused point and circle is representative of unfocused points [88].	34

Figure 2-18 (a) Schematic counter-rotating Dean flow in a curved and low aspect ratio cross-section of microchannel while shows (b) main flow velocity distribution (c) effect of De number for decreasing (top) and increasing (bottom) condition on streak width which display the distance normalized by particle diameter from inner wall; the gray part shows the streak width is more than 3.8 particle size [126] (d) particle equilibrium location across the channel cross-section for different flow condition and particle sizes [84]	35
Figure 2-19 (a) Spiral chip with trapezoidal cross section for separating leukocytes from RBCs [48] (b) schematic particle equilibrium position within a trapezoidal cross-section for different flow condition [49] (c) high throughput CTC enrichment by using slanted trapezoidal spiral [44] (d) fluorescently labeled particle equilibrium position inside a rectangular and trapezoidal spiral for varying flow rates [49]. ..	38
Figure 2-20 (a) Images of spiral chip separating 2.1 μm and 4.8 μm particle diameter while the small particle size is below the critical threshold for inertial focusing ($a/H=0.042 < 0.07$) (b) Separation of 4.8 μm from 2.1 μm particle diameter by using spiral while 4.8- μm particles equilibrate close to inner wall in a particle-free zone of 2.1 μm particle diameter [131]. (c) Separation of E.coli ($K\sim 0.01$) from 3x diluted blood in a spiral channel using sheath flow, 500 μm (W) \times 80 μm (H) [47].	39
Figure 2-21 (a) Nucleolus-stained hMSCs on Synthemax II hydrogel microcarriers after 4-5 days in culture and (b) its phase-contrast image (Corning). Scale bars are 100 μm	45
Figure 2-22 Cytodex 3 breakage in a 500-mL spinner flask (Corning) with 120 rpm rotational velocity at day 7. The medium is sterilized DI water.	47
Figure 2-23 Different sources of particulates in cell therapy.....	48
Figure 3-1 Schematic representations of shear-gradient lift force (F_s), wall-induced lift force (F_w) and cross-laterally wall-effect lift force (F_{CL}) in (a) a rectangular and (b) a trapezoid microchannel. (c) Rectangular and trapezoid straight microchannels designed; slope of the slanted wall is $\tan(\alpha)$	54
Figure 3-2 Photograph of the Experimental setup	57

Figure 3-3 (a) Normalized axial velocity and vorticity profile at $Re=100$ for channels with rectangular and trapezoidal cross-sections with $\tan(\alpha)=0.2$. All contours are plotted under the same condition to be comparable qualitatively. Dash lines show zero-shear rate boundary where direction of shear-gradient lift force alternates. (b) The corresponding normalized axial velocity profile for the rectangular and the trapezoidal channel at the middle of channel height coincided with dash lines at ω_x contour. It shows that the deviation of maximum velocity toward the longer side wall is enhanced by increasing channel AR from 2 to 4. (c) Normalized axial velocity profiles of trapezoid straight microchannels for increased slopes of the slanted wall at the middle of channel height. 59

Figure 3-4 (a) Fluorescent images of 10- μm ($K\sim 0.2$) and 15- μm ($K\sim 0.3$) microparticles display lateral distribution of particles in the trapezoidal channel with $AR=2$ and $\tan(\alpha)=0.2$, (b) corresponding intensity line scan of 15- μm particles across the channel width (Letter L and S show the longer and the shorter side wall of the trapezoidal channel, respectively). 60

Figure 3-5 Fluorescent images and the corresponding intensity line scans of the rectangular channel (a-b) and the trapezoid with $\tan(\alpha)=0.2$ (c-d) for 20- μm particles ($K\sim 0.4$). (e) Fluorescent images of various particle sizes in the trapezoid channel with $\tan(\alpha)=0.45$ and the corresponding line scans for (f) 20- μm particles ($K\sim 0.4$) and (g) 45- μm particles ($K\sim 0.9$), displaying lateral distribution of particles in the trapezoidal channel. The channel aspect ratio of all channels is $AR=4$ (Letter L and S show the longer and the shorter side wall of the trapezoidal cross-sections, respectively)..... 63

Figure 3-6 (a) Top and side view of the particle focusing ($K\sim 0.9$) in the trapezoid channel with $\tan(\alpha)=0.45$ and (b) the corresponding schematic particle movements by increasing Re . (c) Transient lateral particle focusing along the channel length and the corresponding line scans for $Re\sim 545$ and $K\sim 0.9$. It demonstrates a two-step lateral movement while it first moves toward the longer side wall and then starts shifting back toward the smaller side wall (Letter L and S show the longer and the shorter side wall of the trapezoidal cross-sections, respectively). 65

- Figure 3-7** (a) Lateral focusing and filtration of particles through the longer wall outlet in the trapezoid straight channel ($\tan(\alpha) \sim 0.45$ and $AR \sim 4$), and (b) the corresponding samples collected from the shorter wall (SW) outlet and the longer wall (LW) outlet at $Re \sim 88$ (0.4 mL/min). (c-e) Concentration of various particle sizes (15 μm , 20 μm and 45 μm) collected from the SW outlet and the LW outlet. (f) Efficiency of particle filtration vs. flow rate..... 67
- Figure 3-8** (a) Transition of lateral focusing from the middle of channel cross-section toward the shorter side wall as the Re number increases. (b) Concentration of samples collected from the SW and the LW outlet and (c) the corresponding efficiency (Letter **LW** and **SW** show the longer and the shorter wall outlet of the trapezoidal cross-section ($\tan(\alpha) \sim 0.45$ and $AR \sim 4$), respectively). 69
- Figure 4-1** Schematic model showing filtration of microcarriers from cell suspensions. (a) The microcarrier-cell suspension is driven to the channel using a peristaltic pump. (b) Channel cross-section A-A before bifurcation. Microcarriers equilibrate near the inner wall (IW) by the balancing forces shown schematically whereas cells are mainly circulated by secondary flow and harvested through the outer wall (OW) outlet. 74
- Figure 4-2** (a) Axial velocity profile (+X direction) and vortices structure (Helicity contour) in the rectangular and trapezoidal channels with $\tan(\alpha) = 0.0375$. (b) Secondary flow distribution and (c) its maximum positive secondary flow velocities, whose direction from outer wall to inner wall, reduce notably at different loops of the scaled-up rectangular and trapezoidal spiral channel at flow rate of 30 mL/min, but the trapezoidal spiral shows relatively higher positive secondary velocity (+Z direction) and as a result larger drag force to drive particles to the inner wall..... 76
- Figure 4-3** Microcarrier focusing dynamics at the last loop of spiral channel in (a) the trapezoid with $H = 500 \mu\text{m}$ $\tan(\alpha) = 0.075$, (b) $H = 700 \mu\text{m}$ and $\tan(\alpha) = 0.075$, (c) $H = 500 \mu\text{m}$ $\tan(\alpha) = 0.0375$ and (d) $H = 500 \mu\text{m}$, rectangular cross-section ($\tan(\alpha) = 0.0$). (e) Filtration of microcarriers from the inner wall outlet at 30 mL/min using trapezoidal spiral $H = 500 \mu\text{m}$ $\tan(\alpha) = 0.0375$. It demonstrates complete removal of microcarriers for high microcarrier volume fraction of 1.68%, while collecting 70% of carrier fluid from the outer wall outlet. Focusing and partial

focusing refer to particle band width (BW) $< \sim 4a$ and $\sim 4a < \text{BW} < \sim 10a$, respectively.

..... 85

Figure 4-4 Collected samples from (a) the inner wall (IW) outlet and (b) the outer wall (OW) outlet (scale bar is 200 μm). (c) monolayer culture in a 6-well plate in day 5 and (d) PrestoBlue assay displays semi-quantitative growth of harvested BM-hMSCs compared to control sample. (e) Viability of harvested BM-hMSCs from the OW outlet at pass (I,II) and the IW outlet at pass (II) compared to initial viability. (f) Yield gains from the OW outlet at first and second pass and loss from the IW outlet at second pass. (g) Multipotency assay of harvested BM-hMSCs using Red-oil solution, alizarin red and alcian blue to stain lipid droplets (adipocytes, left panel), calcium deposits (osteoblasts, central panel), and extracellular matrix proteins (chondrocytes, right panel) respectively. 89

Figure 5-1 (a) Schematic variation of particle clogging ratios in a rectangular spiral and a trapezoidal spiral with large slant ($H_{\text{outer wall}}/H_{\text{inner wall}}=1.8$); it shows that a broader particle size range can be entrapped close to the outer wall of trapezoidal spiral. The particle clogging ratio can potentially increase to $K \sim 1$ without clogging the channel. (b) Schematic structures of Dean vortices of rectangular and trapezoidal spirals for low and high Dean magnitude. The Dean vortex structure in rectangular spiral channels can be altered by an increase in Dean magnitude itself and/or a transformation of the cross-section to a trapezoid. 93

Figure 5-2 (a) Schematic outline of the scaled-up spiral with rectangular and trapezoidal cross-sections compared to a conventional spiral. (b) Specifications of curvature ratios for conventional and scaled-up spirals. (c) Dean profile of the scaled-up spirals for different Re numbers. Rapid reduction of Dean magnitude occurs due to significant enlargement of the radius of curvature as a result of scale-up. (d) The impact of scaling up channel cross-sections on the curvature ratio (δ). 98

Figure 5-3 (a) Particle focusing of $K=0.35$ (175 μm , bright field) and $K=0.2$ (100 μm , fluorescence) are shown at successive loops of the rectangular spiral. (b) Dimensionless axial velocity V_x and helicity density contours at the first loop. Increase in flow rate and corresponding Dean magnitude transforms the axial

velocity profile while the core of maximum velocity is noticeably skewed toward the outer wall. The helicity density function (H_d) shows the Dean vortex structure of the spiral channel precisely. The evolution of H_d when the channel De number increases from ~ 22.7 to ~ 68 displays movement of Dean vortex cores toward the outer wall. 101

Figure 5-4 (a) Particle focusing of $K=0.35$ ($175\ \mu\text{m}$, bright field) and $K=0.2$ ($100\ \mu\text{m}$, fluorescence) at successive loops of the trapezoidal spiral. Interestingly, $K=0.35$ particles migrate fast toward the outer wall at first loop for $Re \approx 200$ under the dominating shear-gradient lift force while further traveling to the downstream spiral loops causes particle mixing despite the reduction of Dean magnitude by 40%. (b) Evolution of dimensionless axial velocity and Dean vortex contour of the trapezoidal spiral by increasing De number. (c) Dimensionless shear rate field of partial of axial velocity with respect to height of the trapezoid at the first loop (to find out the boundary where the sign of shear rate alternates, its range is lowered). Increasing Dean to ~ 70 results in formation of a dipole near the outer wall. 103

Figure 5-5 Particle focusing map. The square and triangular markers represent the rectangular and trapezoidal channels respectively. Solid markers show focusing (particle band width $< \sim 4a$), markers with pattern depict partial focusing ($\sim 4a < \text{particle band width} < \sim 6a$) and plain markers display non-focusing (Only inside the Green zone focusing can be developed for millimeter scale channels). The focusing map here considered focusing either near the inner wall or the outer wall. 106

Figure 5-6 Impact of microcarrier volume fraction of (a) 0.42% (b) 0.84% (c) 1.7% (d) 3.4% on particle focusing at different loops of the trapezoidal spiral for $Re \geq 200$. The particle focusing at 5th loop is ruined even for $Re \approx 300$ when $V_f \geq 0.42\%$ whereas the particle-free region remains at the inner half of the channel cross-section for the first loop. 108

Figure 5-7 (a) Image of the fabricated single-loop trapezoidal spiral channel (the microchannel was filled with a red dye for visualization). (b) Microcarrier focusing behavior at the bifurcation for different flow regimes and microcarrier (MC) volume fractions of 0.42%, 0.84%, 1.7% and 3.4%. (c) Pictures of samples collected from

the inner outlet and the outer outlet for 1.7% MCs feed (the concentrated MC sample has a blue color due to the trypan blue-dyed MCs). (d) The rejection factor for different microcarrier volume fractions when flow rate is 24 mL/min (n=3).....	109
Figure 5-8 (a) Optical images of the fabricated spiral channels display the footprint of the trapezoidal spiral with 6 loops versus that of single loop. (b) Inertial migration of $\approx 43 \mu\text{m}$ fluorescent particles (Polysciences, USA) toward the outer wall at bifurcation in the single-loop trapezoidal spiral. Particles are mainly filtered from the outer outlet at a flow rate of 24 mL/min.	111
Figure 5-9 (a) 7-day cell growth profile of human Bone Marrow-derived Mesenchymal Stem Cells cultured on Cytodex 3 microcarriers in spinner flasks. (b) Histograms of cells' surface markers expression harvested at day 7.....	113
Figure 6-1 (a) Schematic diagram illustrates removal of particulates from manufactured cell suspensions using inertial microfluidics. (b) The optical picture of fabricated trapezoidal spiral channel with large AR=10 mounted on the fluorescence microscope. (c) The relatively smaller cells are trapped at vortex cores while the larger particles equilibrate near the inner wall (IW) due to the interplay between shear-gradient lift force (F_S), wall-effect lift force (F_{CL}), wall-induced lift force (F_W) and secondary drag force (F_D).	120
Figure 6-2 (a) Inertial focusing of fluorescent particles in the trapezoidal spiral channels H160-290 μm -W1600 μm and (b) the corresponding intensity line scans for 25- μm particles. It shows that the transition takes place at flow rates higher than 6 mL/min. (c) Intensity line scans of different-sized particles at flow rate of 6 mL/min ($Re \sim 109$).	122
Figure 6-3 (a) Inertial focusing of $\sim 30\text{-}\mu\text{m}$ fluorescent particles in the presence of MSCs for various concentrations at flow rate of 6 mL/min ($Re \sim 109$). It shows the effect of cell-particle interactions on inertial focusing. Separation performance of the chip using 0.8×10^6 MSCs/mL spiked with (b) $\sim 30\text{-}\mu\text{m}$ particles at two different flow rates of 6 and 8 mL/min and (c) various particle sizes at flow rate of 6 mL/min. (d) viability of MSCs before and after sorting and (d) the corresponding collected samples from the IW and OW outlet using the trapezoidal spiral channel at flow rate of 6 mL/min ($Re \sim 109$).	125

Figure 6-4 (a) Monolayer culture of MSCs after harvesting using the trapezoidal spiral channel and control sample at day 3. (b) Demonstration of trilineage differentiation of harvested MSCs to adipogenic, osteogenic and chondrogenic lineages. (c) Immunophenotype of harvested MSCs using the trapezoidal spiral; it shows the positive expression for CD90, CD105 and CD73..... 127

Abbreviations

a	Particle diameter [m]
AR	Channel aspect ratio
C	Particle confinement ratio
D	Channel diameter [m]
De	Dean number
D_H	Channel hydraulic diameter [m]
F_D	Secondary drag force [N]
F_L	Net inertial force [N]
F_S	Shear-gradient lift force [N]
F_W	Wall-induced lift force [N]
F_{CL}	Cross-laterally wall-effect lift force
f_L	Dimensionless net lift coefficient
G	Local shear rate [s^{-1}]
H	Channel height [m]
H_d	Helicity density [ms^{-2}]
K	Particle clogging ratio
L_C	Characteristic length scale [m]
R	Radius of channel curvature [m]
Re	Channel Reynolds number
Re_P	Particle Reynolds number
U	Flow field velocity [ms^{-1}]
U_{avg}	Mean flow velocity [ms^{-1}]
U_D	Secondary velocity [ms^{-1}]
U_{max}	Maximum channel velocity [ms^{-1}]
U_S	Particle slip velocity [ms^{-1}]
V_f	Particle volume fraction
W	Channel width [m]
δ	Channel curvature ratio
μ	Dynamic viscosity [$kgs^{-1}m^{-1}$]
ν	Kinematic viscosity [m^2s^{-1}]
ρ	Density [kgm^{-3}]
ω	Vorticity [s^{-1}]

Chapter 1 Introduction

1.1 Background and Motivation

Separation of cells and particles play significant roles in many multidisciplinary areas such as environmental assays, analytical chemistry and cell biology by manipulating the microscale environment containing fluid, particles and cells. In recent years, microfluidics is being utilized in many biomedical purposes particularly diagnostics, for instance blood screening, due to rapid sample processing and low volume of biofluids required [1].

Cell and particle handling is of interest in both standalone devices [2, 3] and modules in lab-on-a-chip applications [4, 5]. Generally, all cell/particle separation and filtration techniques are categorized into active and passive system while it is discriminated by a source of lateral force driving particles across streamline in a conduit. Active systems refer to external force field, including magnetophoretic [6, 7], dielectrophoretic [8-11], and acoustic force [12-17], which is applied on cells/particles; however, passive systems are a function of hydrodynamic drag force and non-intuitive lift force originate from flow and channel structures including curvature [18], barrier, weir, micropost, etc. [4, 5]. Fluorescence activated cell sorting (FACS) and magnetic actuated cell sorting (MACS) are two active techniques applying external force fields in association with biochemical markers [19] which are widely adopted in cell biology. However, these techniques are prohibitive for scale-up applications due to reagent costs, maintenance and requirement for trained personnel. Moreover, these techniques are dependent on quality of reagents [4, 5]. Hence, label-free methods exploiting physical characteristics of particles or cells such as size, density, shape, deformability, electrical polarizability, electrical impedance are seen as potential replacements to FACS and MACS [4, 20].

Moreover, particle separation at a real world-scale is a challenge. Traditionally, microfluidics is limited to small amounts of fluid processing, for example, sample processing for diagnostics. The low throughput of microfluidics has been a major impediment to many industrial and clinical applications such as isolating circulating tumor cells (CTCs) from peripheral blood for either diagnostics or specifically filtration [3]. Also, many cell types are affected by factors such as shear stress and it is important that processing techniques do not negatively affect their morphology, phenotype and potency; hence passive and label free methods are preferred. Methods such as hydrophoretic sorting [21], pinched flow fractionation (PFF) [22], hydrodynamic filtration [23], deterministic lateral displacement (DLD) [24] and inertial focusing [25] leverage on intrinsic hydrodynamic forces in order to avoid influencing cell recovery and probable side effects of external force fields. Despite the fact that sorting particles hydrodynamically is only a function of fluid flow structure, aforementioned methods such as PFF and DLD are inherently restricted to low-Reynolds flow ($Re < 10$), corresponding with low throughput [26]. However, inertial particle focusing performs based on significantly higher Re number of as big as two orders of magnitude ($Re \sim 100$) than that of the rest of microfluidic methods, leading to a high-throughput technology [2, 3, 27].

Given relative ease of parallelization of inertial microfluidics due to the label-free and passive characteristics, this paves the way for processing large volumes (\sim Liter/min) [2, 3]. Potentially, it may be possible to integrate inertial microfluidics with some external force fields such as acoustic waves and dielectrophoretic force [28, 29] to enhance throughput, efficiency and control; however, this most likely hampers the scalability of inertial focusing through scaling out or multiplexing microchannels. Therefore, inertial microfluidics is a promising method in terms of yield, purity and scalability [2]. However, the main hurdle is low volume fraction of suspended particles/cells which is approximately less than 0.5% [25, 30-34], requiring either predilution sample step or applying sheath flow simultaneously in many biological samples.

Although lateral migration of neutrally-buoyant particles was first discovered in a circular channel at macroscopic scale [30, 31], applying inertial focusing phenomenon in a rectangular microchannel resulted in unprecedented formation of two lateral particle streams adjacent to center of long walls. Consequently, it led to establishment of new techniques for particle sorting [35], separation [36] and filtration [37, 38] in a straight channel. Recently, a two-step model for inertial migration of particle in a rectangular channel was developed by Papautsky's group [39]. While this model is in agreement with square channel, which has four focusing points at the middle of each wall face, it cannot explain completely the reduction of focusing point in a rectangular channel. Therefore, it is necessary to break down the symmetrical axis in a square or rectangular channel by using a trapezoid to investigate further wall-effect lift forces and designing new straight channels for filtration and separation applications.

Other than straight channels, there are different structured channels exploited in inertial microfluidics, including spiral [33], serpentine [40] and contraction-expansion pattern [41]. Spiral microchannels have been extensively employed in many biological applications such as blood plasma extraction [34, 42], enrichment of circulating tumor cells (CTCs) from peripheral blood [43-45], membrane-less filtration [2], cell and protein separation [46] and isolation of bacteria from whole blood [47]. These broad utilizations of spiral microchannels are owing to strong differential focusing position as a function of particle size and high-throughput trait compared to the rest of structured channels. To increase separation resolution in a spiral channel, the rectangular cross-section was altered to a trapezoid [44, 45, 48-50]. This exclusive modification enhanced separation resolution, thereby increasing cell/particle concentration, and throughput.

Industries such as the bioprocessing and cell therapy industry commonly deal with a broad range of particle sizes that could reach one order of magnitude higher than cell sizes (i.e. $\sim 100\ \mu\text{m}$). However, most previous studies have been focused on micron-scale bioparticles/channels and therefore, it is important to investigate and

establish scale-up methods for Dean-coupled inertial focusing for greater particle sizes than 50 μm . This study will provide more insight into the inertial focusing within scaled-up channels that deal with large particle sizes ($\sim 100\ \mu\text{m}$) which has not been studied in open literature and demonstrate proof of concept filtration devices for microcarrier-cell culture in bioprocessing.

1.2 Objective and Scope

The objective of this work is to develop a high-throughput, continuous and membrane-less filtration device based on the principle of inertial focusing that possesses a potential to reach a relevant industrial scale (Liter per minute) for a broad range of particle sizes (greater than 50 μm). This requires scaling up channel hydraulic diameter ($D_H > 0.3\ \text{mm}$) to avoid channel clogging.

The scope of this project is to:

1. Investigate inertial particle focusing dynamics in trapezoidal channels.
2. Study effects of scaling up channel hydraulic diameter on Dean-coupled inertial focusing.
3. Design and develop a new proof-of-concept device and working methods to continuously separate or filter particles/cells which can be potentially applied in a broad range of applications as well as removal of particulates contamination in cell therapy industry.

1.3 Outline of the thesis

The remainder of this thesis is organized as follows:

Chapter 2 discusses the inertial particle focusing phenomenon and its emerging applications for cell and particle sorting in a microchannel. Principles of particle focusing and corresponding force analysis within inertial circumstances are described particularly for straight and curved channels. Different channel structures

of inertial microfluidics and their performances in cell/particle separation and filtration are discussed. Furthermore, a brief review on the cell therapy manufacturing process and particulates contamination are reported.

Chapter 3 investigates inertial particle focusing dynamics experimentally in a straight trapezoidal channel for a broad range of channel Re number ($20 < Re < 800$). A switching in equilibrium position of larger particle sizes ($K = a/H_{min} \sim 0.9$) laterally from longer side wall to shorter side wall is explored when the channel Re number increases to ~ 650 . Finally, a trapezoidal channel with large slanted wall is designed for filtration of a broad range of particle sizes ($0.3 < K < 1$) when Re is less than 100.

Chapter 4 demonstrates microcarrier focusing dynamics in scaled-up trapezoidal spiral channels. The numerical model highlights a critical effect of slanted wall which contributes to enhancing secondary flow. An ultra-low-slope trapezoidal spiral is found experimentally that outperforms regarding focusing near the inner wall. As a result, it is applied to remove microcarriers from stem cell suspensions. Biological assays were carried out to validate the morphology and potency of the cells post process.

Chapter 5 provides an insight into scaling up inertial microfluidics. A systematic experiment was carried out to establish the $Re-D_H$ map showing the critical threshold of channel hydraulic diameter for Dean-coupled inertial focusing. Furthermore, a trapezoidal channel using inflection point focusing was developed with remarkably lower footprint and higher throughput. Accordingly, a proof-of-concept microcarrier-cell retention device is showcased that is potentially capable of continuously running during microcarrier cell culture for either medium exchange or removal of particulates.

Chapter 6 reports a hybrid method to separate particulates larger than cell sizes. Having been sieved, the cell suspension goes through an inertial separator to remove larger particulates which cannot be pulled out by sieving due to the limitation on the

mesh size. A scaled-up trapezoidal spiral channel is established first. Removal of particulates down to 25 μm from mesenchymal stem cell suspensions is demonstrated. The trilineage differentiation and surface markers are expected prove the validity of the proposed method.

Chapter 7 presents the conclusions of this research and briefly addresses some future work.

Chapter 2 Literature Review

2.1 Introduction

Separation of particles and cells is a common step in environmental assays and numerous industrial and biomedical processes. Filtration, sedimentation and centrifugation techniques are frequently used to separate and classify particles and cells, but the performance of these approaches is generally poor when the differences in size between target and non-target particles are small [51]. Furthermore, clogging and fouling of device components is inevitable, and this fundamentally limits the efficiency and reliability of the filtration process [52].

The development of microfluidics in the past 15 years has led to a number of new methods for the separation and selection of micro-particles through precise control of fluid flow. Amongst existing microfluidic systems, inertial microfluidics (IMF) has experienced massive growth in many applications ranging from cell detection and isolation [53, 54], cytometry [55], multiplexed bio-assays [56-58] and also fluid mixing [59, 60]. As a passive technique, it manipulates cells and particles by taking advantage of hydrodynamic forces in microchannels with a variety of cross-sections (i.e., square, rectangular, triangular, trapezoidal and circular) without an externally applied field [27, 61]. There are also a plethora of active techniques such as magnetophoresis [6, 7], dielectrophoresis [8-10], and acoustophoresis [12-15]. Comprehensive and insightful reviews about these different techniques can be found in the literature [3, 18, 62].

This chapter reviews the main hydrodynamic lift forces that induce lateral migration of neutrally-buoyant particles followed by different channel structures of IMF and their mechanisms. Straight and spiral channels are highlighted due to higher throughput and yield as well as their potential of scaling up. Some of the demonstrated applications of IMF are also summarized. Next, an introduction to downstream processing of stem cell therapy is presented. And, unmet challenges in

purification of cell therapy products associated with particulates matter contamination will be addressed.

2.2 Inertial particle equilibrium phenomenon

Inertial particle focusing phenomenon was discovered in 1961 by Segre and Silberberg; when neutrally-buoyant spherical and rigid particles (~ 1 mm diameter) were suspended randomly in a Newtonian fluid and passed through a vertical tube at the order of 1 cm diameter, the particles migrated laterally across the streamline to form an annulus within the realm of laminar flow [30, 31]. They termed this the "*Tubular Pinch Effect*" (Figure 2-1). Matas et al. [63] further explored the effect of Reynolds number (Eq. 2.1), inertial term relative to viscous effect, on particle migration across the streamline. Their findings showed that higher Re results in bigger annular particle equilibrium.

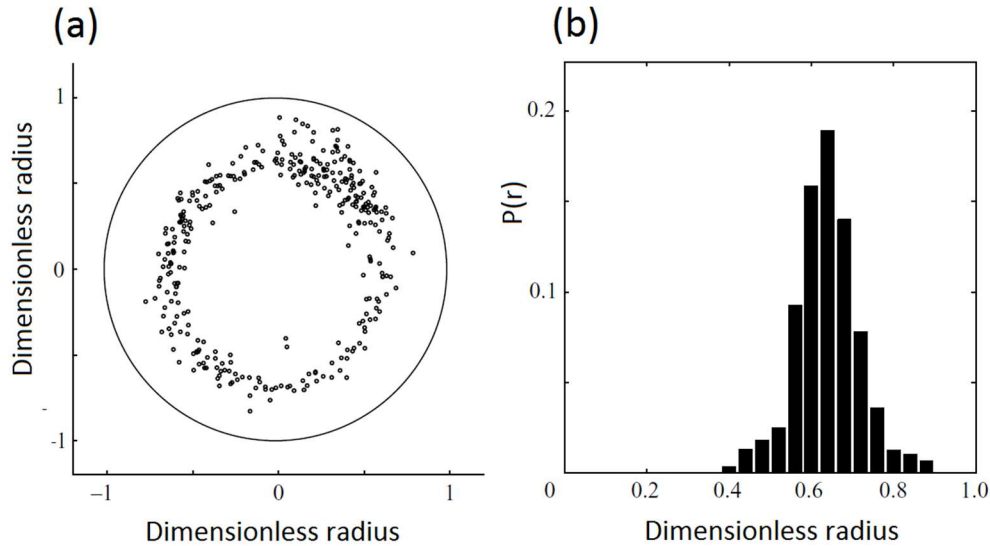


Figure 2-1 (a) Experimental distribution of neutrally-buoyant particles over circular cross section for $D/a=9$ and $Re=134$ (b) corresponding probability function [63]

$$Re = U_{max} D_H / \nu \quad (2.1)$$

where U_{max} is maximum axial velocity, D_H and ν are hydraulic diameter and kinematic viscosity of fluid, respectively.

In addition, Matas and his colleagues [64] observed another remarkable aspect of lateral migration of neutrally-buoyant particles which was inertially self-ordered particle trains (Figure 2-2) in the direction of flow ($Re > 200$) when the ratio of particle diameter to pipe diameter was at least 0.03. This particle ordering phenomenon was interpreted as evidence of the existence of a reverse flow behind and in front of particles, which originates from the rotation of particles in a flow, such that the particles are aligned along the main streamlines; recently it was proven as a particle-induced lateral transport phenomenon demonstrating particles as an active elements disturbing and modifying the flow [65].



Figure 2-2 Trains of particle for $D/a=19$ at $Re=1200$ in a circular channel [64]

In general, key factors required for capturing this phenomenon are: (1) neutrally-buoyant particle, (2) Newtonian fluid, (3) low volume fraction of particles in order of $\leq 1\%$, (4) relatively high shear rate in comparison to Stokes flow (Re number in order of 100) [25, 27, 30, 31, 37] and (5) comparable particle size to characteristic channel length $C=a/D_H > 0.07$ [25], where a is particle size and D_H is the hydraulic diameter.

2.3 Fundamental inertial forces

Following the observation of lateral particle migration, more profound investigations have been carried out to dissect and explain inertial focusing phenomenon theoretically. Generally, the transverse migration of a spherical rigid

particle originates from the nonlinearity of fluid inertia, i.e., unperturbed quadratic velocity flow field. To clarify this nonlinearity effect, by assuming lateral movement of particle towards the wall in a flow condition without advection transport, i.e., $Re \sim 0$, the particle would move towards the centerline if the direction of flow is reversed; however, this does not happen in the presence of fluid inertia due to the symmetry [27, 66, 67].

Study of lateral lift forces on a particle commenced with analytical asymptotic expansion method which described a lift force induced by particle rotation within a low Re number flow (Figure 2-3), or specifically low particle Reynolds number ($R_p = Re(\frac{a}{D_H})^2 \ll 1$) [61, 63], for which the force was $F_{RK} = \frac{\pi}{8} a^3 \rho \Omega \times U$ (a is particle diameter, ρ is density of fluid, Ω is angular velocity and U is the velocity of the fluid) as established by Rubinow and Keller [66]. This force is independent of viscosity, and there is a similarity between Rubinow-Keller force and Bernoulli's theorem describing that the low-pressure area close to a rotating body is formed where velocity is increased by the rotation of object and vice versa, then unbalanced pressure distribution around the peripheral object produces a lift force. However, the shear force on the basis of particle rotation results in a lift force towards the center of channel that contrasts with Segre and Silberberg's observations [68].

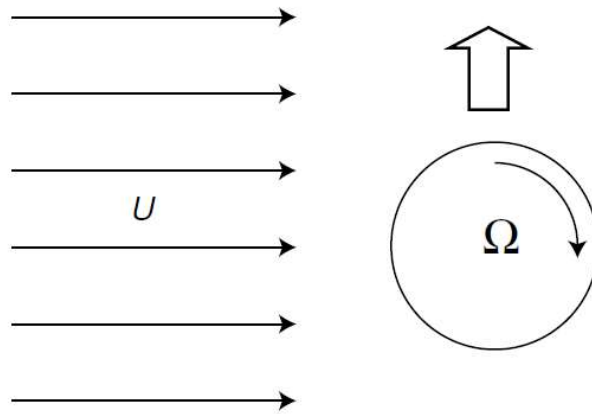


Figure 2-3 Schematic Rubinow and Keller force (Magnus effect) [68]

The second type of transverse lift force was derived by Saffman [69] who extended the Rubinow-Keller force through matched asymptotic expansion method while the particle was free from rotation and flowing in an unbounded shear flow (Figure 2-4). Although Saffman intended to describe the relationship between the physical characteristics of the particle, properties of the fluid such as viscosity and the relative velocity of particle to flow field ($F_{Saff} = 81.2U_s(a/2)^2\sqrt{G\rho/\mu}$ where U_s is particle slip velocity and G is shear rate), it was not applicable for neutrally-buoyant particle in Poiseuille flow due to lack of Stokeslet in the absence of external force fields. Thus, the Saffman lift force is only applicable for non-neutrally-buoyant particles, for instance, when particle-laden flows are driven through vertical tube under the influence of gravitational force field. In addition, Saffman force is one order of magnitude greater than Rubinow-Keller force since the nature of Saffman force is based on the interaction between particle slip velocity and fluid shear [61, 68].

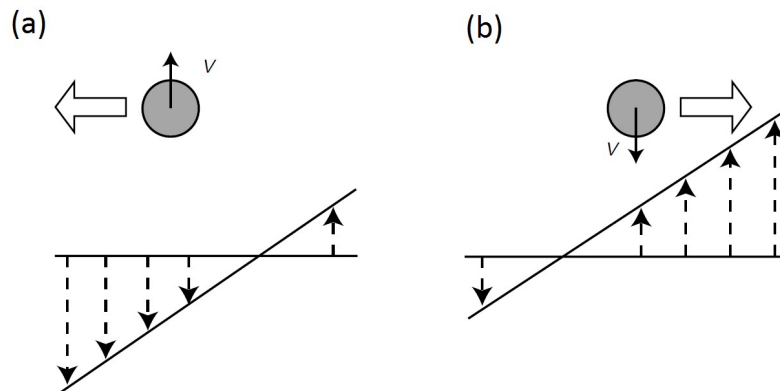


Figure 2-4 Spherical particle (a) Leading (b) lagging the fluid flow and its respective direction of Saffman forces [68]

Although primary attempts including the Saffman and Rubinow-Keller forces tried to clarify lateral migration of neutrally-buoyant particles, they were not able to prove this phenomenon. Subsequently, effects of shear gradient and quadratic flow as the main factor was theoretically uncovered by using the perturbation method which is described in the next section.

2.3.1 Shear-gradient lift force

To elucidate inertial focusing (Segre-Silberberg annulus), wall-particle interaction and parabolic velocity profile of pressure driven flow (Figure 2-5) were modeled by Ho and Leal [70], and Vasseur and Cox [71] for low particle-Reynolds-number flows using the regular perturbation method.

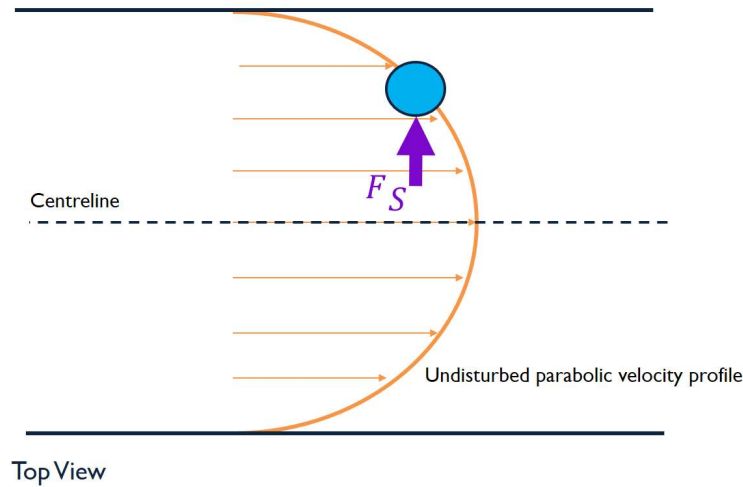


Figure 2-5 Curvature of velocity profile effect on particle and the corresponding shear-gradient lift force towards wall

Asmolov in 1999 [72] further advanced the perturbation method (matched asymptotic theory) to take into account the effect of wall and unperturbed quadratic velocity profile on particle migration when the Reynolds number is relatively high ($Re \sim 1000$) but particle Reynolds number is assumed negligible ($Re_p \ll 1$), which is the main intrinsic downside of perturbation method, on the other words neglecting finite-sized particle. The results revealed that wall-induced force is significant within a narrow region close to the wall whereas the main inertial force in the far field from wall originates from unperturbed parabolic velocity profile. The derived net inertial force scaled as follows:

$$F_L = f_L \rho G^2 a^4 \quad (2.2)$$

where G is local shear rate and f_L is lift coefficient factor which is a function of Re number and particle position across the channel [18] and it decreases by increasing Re number [73, 74]. Recently Papautsky's group has shown experimentally f_L in a channel with rectangular cross-section can be expressed as follows [39]:

$$f_L \propto \frac{W^2}{a^2 \sqrt{Re}} \quad W < H \quad (2.3)$$

where W and H are channel width and height, respectively. Therefore, the net inertial lift force F_L scales with a^2 ($F_L \propto a^2$). Although f_L is a function of local fluid flow, it can be approximated constant of 0.5 for a finite $Re < 100$ [27].

To investigate the effect of finite-sized particle and scale inertial lift force in contrast to point particle assumption in analytical perturbation theory, Di Carlo et al. [75] carried out finite element numerical simulation of a single suspended particle whose size was in the same order as the square channel height (particle clogging ratio $K=a/H$ ranging from ~ 0.2 to ~ 0.4). Experimental results showed that the equilibrium position approaches the centerline of duct when K increases. Numerical results clarified the effect of finite-sized particle on the scaled inertial force and demonstrated that a scaled inertial force based on perturbation method $f_L = F_L / (\rho U_{max}^2 a^4 / H^2)$ for different particle clogging ratios K (Figure 2-6a) collapses into a single curve when the scaled inertial force are $\rho U_{max}^2 a^3 / H$ and $\rho U_{max}^2 a^6 / H^4$ for a particle approaching the center and the wall respectively (Figure 2-6b&c).

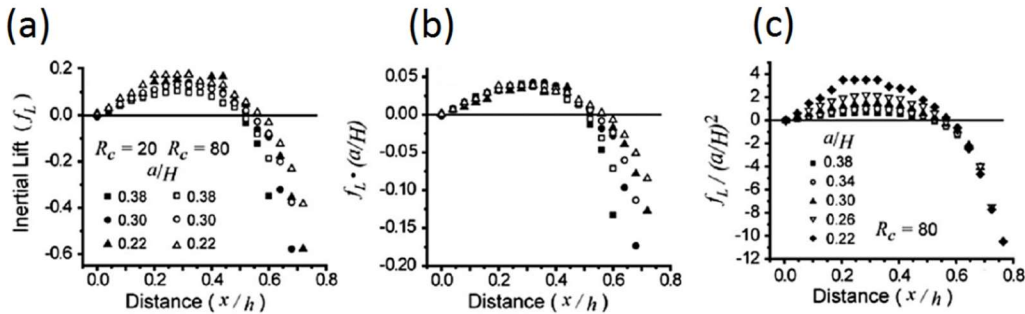


Figure 2-6 Three different non-dimensional lift force based on (a) matched asymptotic theory and finite-sized particle approaching to (b) centerline (c) wall [75]

More recently, it was demonstrated that the scaled lift force established by Di Carlo [75] complied with a perturbation series based on clogging ratio $K=a/H$ [67]. Direct measurement of particle migration velocity in a microchannel proved that the inertial lift force is a complex function of power law upon particle size ($F_L \sim c_4 a^4 + c_5 a^5$ where c_4 and c_5 are unmeasured asymptotic series coefficients) which was in agreement with asymptotic theory [76].

2.3.2 Wall-Induced lift force

Wall-induced lift force is triggered when the particle approaches the wall. The contribution of the wall to inducing force on particles is not straightforward and it should be noted that the parabolic nature of velocity profile inside the conduit cannot be established without the presence of the wall [61]. To eliminate the effect of quadratic velocity profile inducing shear-gradient lift force, the wall effect was experimented via Couette flow, applying a relative movement between two parallel plates. The relative velocity of particle to the nearest wall brought about wall repulsion due to lubrication effect, leading to particle equilibration at mid-plane in Couette flow [70, 77]. Direct numerical analysis of pressure and shear stress on the surface of particle demonstrated dominant effect of wall lubrication [77]. Consequently, a dissymmetry in pressure distribution around the particle adjacent to the wall pushes back the particle towards the center [26] which can be interpreted as a decelerated fluid flow between the particle and side wall, resulting in an increase in pressure based on Bernoulli's principle (Figure 2-7). Also, the other effect of the wall is the particle lags behind the mainstream fluid velocity [26, 27, 61], generating Saffman force towards channel center [78].

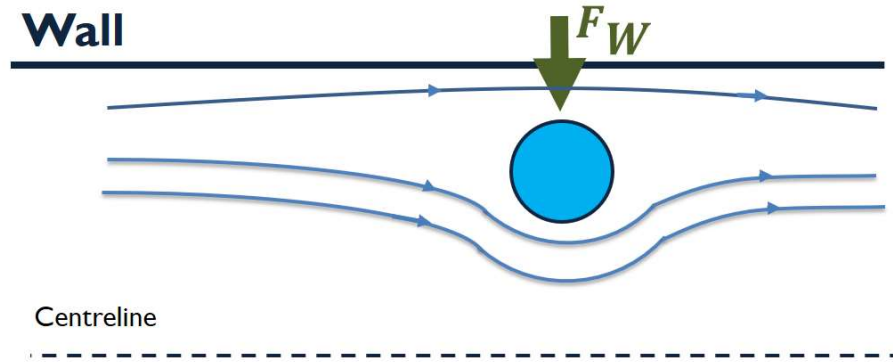


Figure 2-7 Wall-induced lift force towards channel centerline

Despite the fact that much effort has been made so far with regards to wall effects and its impacts on inertial focusing, the effect of altering the critical parameters as well as wall surface roughness and wall pattern are still not understood.

Although the root cause of particle migration under the influence of fluid inertia has been very well established, there does not exist a comprehensive and explicit inertial lift force modeling in multiphase flow. Recently, Liu et al. carried out a complex DNS numerical model for analyzing force on a single spherical particle inside a rectangular channel [79, 80]. A correlation of inertial lift force with local flow field parameters was numerically developed in a rectangular channel [80] where it was applied to complex structural geometries such as double spiral and serpentine; however, this inertial lift force model has not been validated for spiral channels yet. Intriguingly, inertial particle focusing for double spiral [81] and serpentine channel [40, 82] were numerically simulated without the aid of inertial lift force model, showing lack of fundamental understanding of the mechanism.

2.3.3 Secondary drag force

Generally, secondary flow refers to the induced flow which is perpendicular to the mainstream flow raised by altering either channel geometry cross-section (contraction-expansion) or channel curvature (serpentine, spiral, etc.) which are termed structured channels (Section 2.4.2). The contribution of secondary flow is intuitive secondary drag force (F_D) that is scaled based on Stokes drag for low Re number flows and can be described as:

$$F_D = 3\pi\mu a U_D \quad (2.4)$$

where U_D is the secondary flow velocity, a is the particle diameter and μ is the dynamic viscosity of the fluid.

Secondary flow velocity in a structured channel is not only a function of flow condition (Re number) but also it depends on channel geometry. For traditional secondary flow in a curved channel which is called Dean flow (Figure 2-8), the strength of secondary flow is determined by curvature ratio $\delta = D_H/2R$ and fluid inertia (Re) where D_H is the hydraulic diameter of channel cross-section and R is the radius of channel curvature [83-86]. The Dean number is described:

$$De = Re\sqrt{\delta} \quad (2.5)$$

Exploiting secondary flow drag in combination with inertial lift force leads to reduction of particle equilibrium positions within a structured channel. Both inertial lift force and secondary drag force is a function of particle size, so the interplay between these forces forms distinct size-dependent equilibrium positions within a channel cross-section which can be utilized for particle/cell separation based on object size [25, 33, 40, 41, 75, 87, 88].

The average secondary velocity in a curved channel was approximated numerically based on Dean number as follows [89]:

$$\bar{U}_D = 1.8 \times 10^{-4} De^{1.63} \quad (2.6)$$

The corresponding drag force can be approximated based on Stokes drag force (Eq. 2.4)

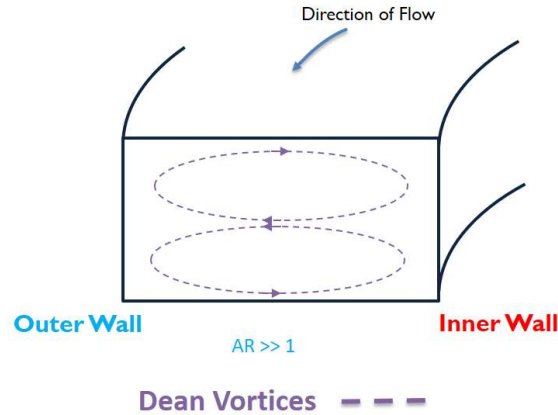


Figure 2-8 Schematic representation of secondary flow in a curved channel

2.3.4 Miscellaneous lift forces

Deformability of particles induces additional lateral forces that result in distinctive deformable- and size-dependent equilibrium positions in superposition with inertial lift forces. Deformability-induced lift force originates from a nonlinearity caused by matching of velocities and stresses at the deformable particle interface [90]. For instance, while healthy red blood cells are deformable, malaria infected red blood cells become stiff and this physical difference allows for diagnosis using inertial focusing [91]. Also, the deformability together with difference in cell size have also been used to classify and isolate cancer cells such as modMCF7 when placed inside a rectangular channel, the cancer cells shifted towards the channel centerline [90].

Furthermore, fluid properties as well as non-linear dynamic viscosity of non-Newtonian fluid [92] and particle shape [93-95] can affect the particle equilibrium positions. However, the impact of these miscellaneous forces is limited and cannot

be extensively used for many practical and high-throughput separation applications. An important limitation is the low-concentration particle suspensions ($V_f < 0.5\%$) required for inertial focusing. This limitation dictates the dilution of real sample; thus, it even eliminates the non-Newtonian characteristics of biofluids such as blood [2, 25, 34, 42, 96].

2.4 Inertial microfluidics channel structures

With the advent of soft lithography, applying inertial particle ordering phenomenon in a non-circular channel resulted in establishing a new method in microfluidics which is reliant on inertial effect of fluid flow ($Re > 10$) in contrast to traditional microfluidics, which works mainly based on Stokes flow ($Re \sim 0$). Herein, various channel structures are introduced and the straight and curved microfluidic channels as well as spirals are comprehensively discussed along with applications. The literature review is mainly focused on particle focusing mechanism and its application in particle ordering, filtration, and separation.

2.4.1 Straight channel

Lateral migration of neutrally buoyant particle under the influence of inertia is a function of channel cross-section. It was observed first in a circular tube at macroscale while particles were focused annularly 0.6 times away from channel center [30, 31]. Chun and Ladd [97] investigated numerically, using Lattice-Boltzmann method, the effects of inertial force in a square cross-section on lateral migration of particles for a wide range of Re ($100 < Re < 1000$). For a particle clogging ratio of $K \sim 0.11$, they showed 8 distinct focused particle streams at corners and centers of each wall faces at $Re = 100$. They demonstrated the particle trains under specific flow conditions which had been observed experimentally by Matas et al. in a circular channel [64]. However, Di Carlo et al. [25] for the first time illustrated experimentally four particle equilibrium positions facing the center of each wall in a square channel by using fluorescent particle (particle clogging ratio $K = 0.18$) and confocal microscopy. Comprehensive particle focusing in square and rectangular

channels with different aspect ratios ($AR=W/H$) and particle clogging ratios (K) was surveyed by Papautsky's group [37, 38]. They proved that the characteristic length scale (L_C) in rectangular channels is the narrowest dimension of channel cross-section where $K=a/L_C>0.07$ is the condition for inertial focusing (Figure 2-9a). The low-AR microchannel ($H>W$) was used for particle filtration using a trifurcated outlet when particles preferentially migrated across the width due to dominating shear-gradient lift force and equilibrated along the channel height (Figure 2-9b).

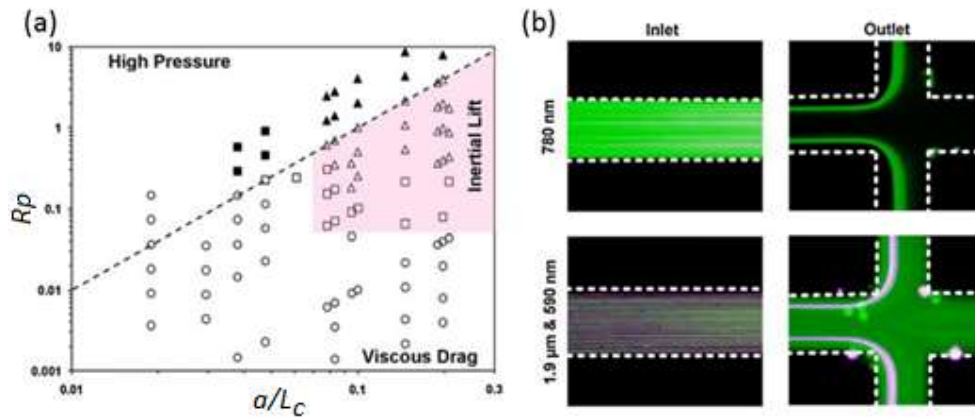


Figure 2-9 (a) Particle focusing quality in rectangular channels with $AR=1/10-1$ as a function of particle Re number and clogging ratio $K=a/L_C$ (unfocused particle flows are represented by circles, partially focused particle streams are represented by squares, and focused particle streams are represented by triangles. Filled markers represent flows with $Re>100$) (b) particle filtration in a low aspect ratio microchannel when particles equilibrated along sidewalls [37]

Choi et al. [98] demonstrated lateral and cross-lateral migration of neutrally-buoyant particles in a square microchannel. The three-dimensional position of the particles in the channel cross-section was illustrated by using a digital holographic microscope. Their results confirmed the formation of pseudo Segre-Silberberg annulus in a square channel (Figure 2-10b and e). More importantly, effect of particle clogging ratio ($K=a/H$) and Re number on cross-lateral migration was experimentally shown (Figure 2-10). Increasing K from critical ratio of 0.075 to 0.16 led to: (1) formation of equilibrium planes close to walls at relatively lower Re number of 12 (Figure 2-10b and e) and (2) cross-lateral migration of bigger particles ($K=0.16$) to the center of equilibrium planes in which located $\sim 0.2 H$ away from

each wall at higher Re of 120 (Figure 2-10f). Finding cross-lateral particle movement following the particle migration across the streamline by increasing particle Re number ($R_p = Re(a/H)^2$) from ~ 0.67 to ~ 3 shed lights for more complicated particle focusing in a rectangular channel.

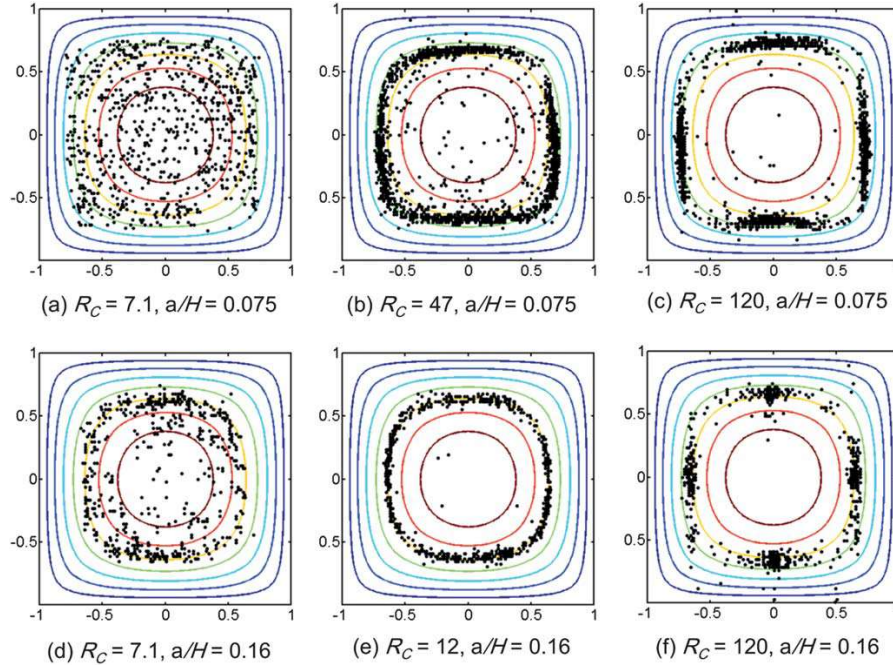


Figure 2-10 Lateral and cross-lateral particle migration in a square microchannel for different particle clogging ratios $K=a/H$ [98]

According to this observation, Zhou and Papautsky [39] conducted fundamental experiments to elucidate non-intuitive behavior of particle focusing in a rectangular microchannel to find out why only two stable equilibrium positions exist in high-AR or low-AR rectangular channels under a specific flow condition. They proposed a two-stage model, first particles migrate across the short wall due to higher shear-gradient lift force and then get balanced close to the wall with wall-induced lift force; afterwards, forces arisen from the particle rotation drive particles located near the corners towards the center of longer wall (Figure 2-11a).

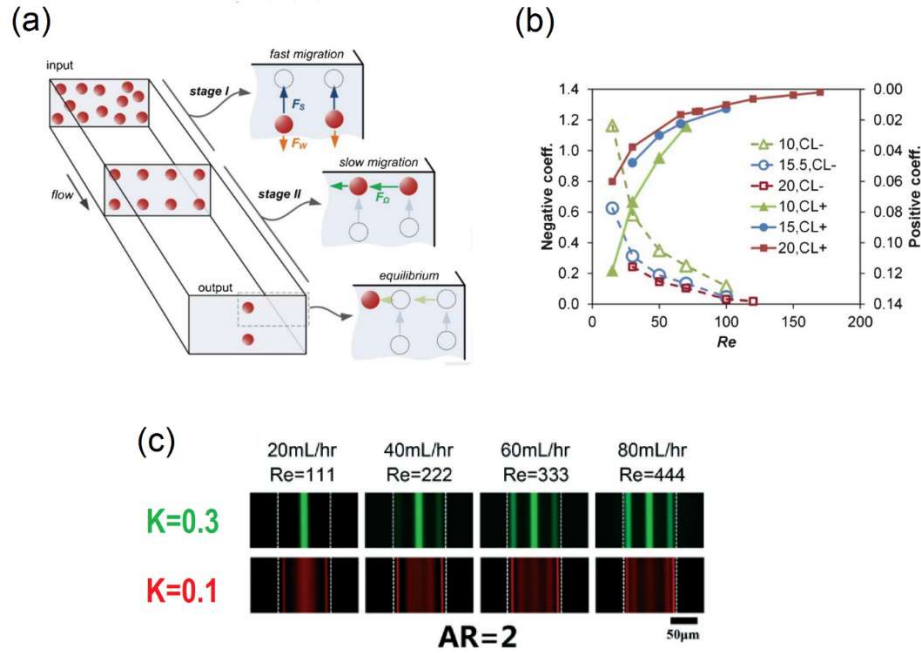


Figure 2-11 (a) Two-stage model of particle ordering in a high aspect ratio microchannel reveals effects of rotation-induced lift forces on particles located in corners, which conduct them towards center-wall equilibrium positions (b) Positive and negative lift coefficients for 10, 15.5 and 20 μm as a function of Re in a low AR 50 $\mu m \times 100 \mu m$ channel [39] (c) dynamic of particle equilibrium positions by increasing Re flow for different clogging ratio K [79]

For the first time, lift coefficients (f_L) were measured experimentally for both two migration stages separately. The lift coefficients were scaled by measuring focusing length (L_F) and particle migration distance (L_m) based on equation below:

$$f_L = \frac{3\pi\mu D_H^2}{2\rho U_{avg} a^3} \times \frac{L_m}{L_F} \quad (2.7)$$

where U_{avg} is the average flow velocity.

A general correlation was obtained for each shear-gradient lift coefficient (called negative f_L^-) and rotation-induced lift coefficient (called positive f_L^+) by applying regression analysis. Ultimately, superposing two types of f_L resulted in general formula to estimate required length for particle focusing as follows:

$$L = \frac{3\pi\mu D_H^2}{4\rho U_f a^3} \left(\frac{H}{f_L^-} + \frac{W}{f_L^+} \right), W > H \quad (2.8)$$

This equation can be easily tuned for square cross section by replacing $H=W$ or circular cross section by setting $W=0$ and H to diameter. They proved that the positive coefficients were one order of magnitude lower than negative coefficients (Figure 2-11b), so the term $\frac{W}{f_L^+}$ was recognized as a determining factor, addressing the significant role of rotation-induced lift forces to control the focusing length. However, the presented rotation-induced lift coefficient is not fully derived since it is not dimensionless coefficient and leave some factors absent:

$$f_L^+ \propto \frac{H^2}{a\sqrt{Re}} \text{ when } H > W$$

In 2015, a comprehensive numerical (DNS model) and experimental analysis was conducted to clarify the effect of Re number and particle clogging ratio K on particle equilibrium position inside a high-AR rectangular microchannels [79]. It was shown that increasing Re ($Re > 200$) results in unstable focusing positions (next to the center of shorter side walls) becoming stable equilibrium positions (Figure 2-11c, $K=0.3$). Even though many studies have been completed so far on inertial focusing, models such the two-stage migration for rectangular channels are not able to fully describe inertial focusing for non-rectangular channels such as trapezoidal channels. In addition, designing a trapezoidal channel to break down the symmetrical axes is of interest to observe the effect of rotation-induced lift force (or wall-effect lift) on particle equilibrium positions.

Increasing the AR of rectangular channel greater than ~ 5.6 with a blunt velocity profile along the channel width caused widening of particle streaks around the mid plane as a result of weakened wall-induced lift force [32]. Based on their two-stage particle migration in a rectangular channel [36], Zhou et al. designed different straight channels for filtration [37, 38, 99], separation [36, 100] and particle ordering [101]. A simple high-AR microchannel ($100 \times 50 \mu\text{m}^2$) was demonstrated for

cell/particle filtration. Bigger particles migrated faster towards the midplane because migration velocity scales as $U_m \propto a^2$, whereas smaller particles remained unfocused and were collected from side outlets (Figure 2-12a) [99]. A channel cross-section consisted of low AR and high AR was fine-tuned along the length for separating cells or particles based on their sizes (Figure 2-12b). Given that focusing length is a function of particle diameter ($L_F \propto a^{-2}$), smaller particles determined the focusing length for first low-AR channel, where primarily all particles were equilibrated close to channel height. Next, in high-AR channel, larger particles migrated faster towards width-centered equilibrium positions whereas smaller particles remained close to the height since migration velocity scales with second power of particle size ($U_m \propto a^2$), and they need more traveling time or longer channel length to be displaced [36].

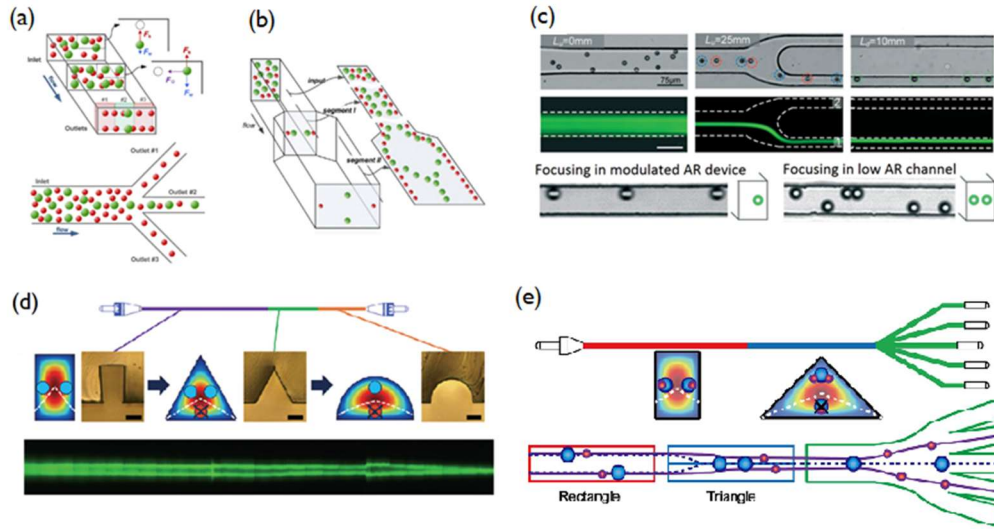


Figure 2-12 (a) High AR channel for cell/particle filtration [99] (b) modulated AR for complete separation of microparticles [36] and (c) single point particle focusing in a straight channel manipulating channel AR [101]. (d) variation of cross-sectional shape along the length for single focusing [102] and (e) particle/cell separation [103].

The manipulated channel AR was also used for single particle focusing stream in a straight microchannel (Figure 2-12c) [101]. The 3D particle focusing without the aid of sheath flow, external force and secondary drag in a structured channel not only has great advantages over traditional complex particle focusing module in

current flow cytometry machines but also it is superior against 2D particle focusing in a low-AR channel demonstrated by Di Carlo et al. [35]. In addition, since the shear rate profile is highly dependent on the shape of the cross-section of the channel, the channel cross-section was introduced recently as another key factor to inertial focusing while mapping focusing points of rectangular, triangular and/or half-circular channels onto a straight composite channel developed a single focusing point [102] (Figure 2-12d) and size-dependent lateral shift [103] (Figure 2-12e) for separation.

Table 2-1 summarizes various demonstrated applications of inertial microfluidics using straight channels.

Table 2-1 Application of inertial microfluidics using a straight channel structure

Application	Sample	AR	Re	Volumetric flow rate ($\mu\text{L}/\text{min}$)	Throughput (cells/min)	Yield	Purity	Remarks	Ref.
Filtration	particle	0.4	<50	-	-	-	-	Low AR	[38]
Filtration	particle	0.2-0.5	>100	-	-	-	-	Low AR	[37]
Filtration	particle/LNCaP cells/HPET cell	2	50	225	-	~99%	-	High AR	[99]
Filtration	Pathogenic bacteria cell	0.33	~40	100	10E6	>80%	-	0.5% diluted blood spiked with bacteria	[104]
Separation	particle/HPET cell	~0.5-2	40	-	-	~99%	~90%	Modulated AR	[36]
Separation	Particle/bovine WBCs	1.5	30	100	-	97%	86%	Modulated AR	[100]
Flow cytometry	cells	~0.43	-	9.7	6.5E6	-	-	1% v/v diluted blood	[35]
Flow cytometry	cells	1.5-0.6	~40	150	51000	95-100%	-	Modulated AR, Single point focusing	[101]
Flow cytometry	particles/cells	-	<100	-	-	-	99%	Non-rectangular	[102]
Separation	particles/cells	-	<100	50-160	-	-	>92%	Non-rectangular	[103]

Variation of AR along the channel length in rectangular channels has been demonstrated as a great technique to tune the straight channel based on induced secondary flows for particle separation. These devices are generally divided into two categories based on their working principles. In the first instance, the low AR channel ($H > W$) is used to focus different-sized particles close to the channel height (sidewalls). Following primary particle focusing, the channel is enlarged bringing about formation of vortices due to the variation of fluid inertia. Since shear-gradient lift force scales with a^3 , bigger particles undergo migration into the vortex and get trapped inside the chamber whereas smaller particles remain mainly focused, travelling along the main flow streamlines towards outlet at downstream (Figure 2-13a) [105-107]. To solve the batch processing drawback of this device, Wang et al. devised side outlets to siphon the trapped larger particles continuously from micro-vortex chambers [108, 109] (Figure 2-13b).

In another instance, an alternating AR, contraction and expansion series, is used while maintaining $AR \geq 1$ for all segments including orifice segments (Figure 2-13c) [41, 110-114]. To further enhance separation resolution, a high-AR microchannel ($W > H$) is employed to aide focusing of larger particles primarily before the contraction-expansion zone [41]. The larger particles migrate towards the center of channel width mainly. But, the multi-orifice structure induces two pairs of secondary flow which mostly affect the smaller particles, drifting them towards the side walls since the drag force is proportional to particle size ($F_D \sim a$) while larger particle streams are kept at the middle of the channel due to higher shear-gradient lift force ($F_L \sim a^3$) (Figure 2-13d) [41, 112-114].

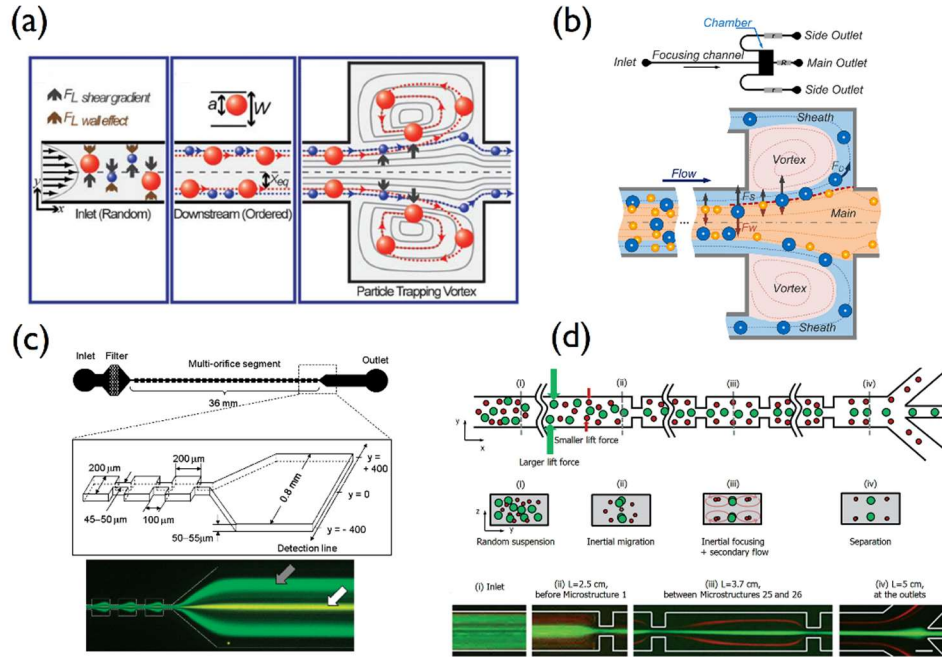


Figure 2-13 (a) Trapping larger particle/cell inside a chamber by utilizing vortices [105] (b) vortex-aided inertial microfluidic design by siphoning larger particle continuously [108] (c) continuous inertial separation of microparticles based on contraction-expansion structure inducing secondary flow (fluorescent image shows separation resolution between large (15 μm , white arrow) and small microparticle (7 μm , dark arrow)) [110] (d) enhancing inertial separation resolution by using high AR channel before the contraction-expansion segment [41]

Vortex-aided and contraction-expansion channel structures have been demonstrated for microparticle separation, blood fractionation, isolation of circulating tumor cells (CTCs). Generally, the best performance accomplished for those devices is limited to a low Re number of <50 and volumetric flow rate in order of $\sim 100 \mu\text{L}/\text{min}$. Although the linear structure and passive feature without the aid of sheath flow provide relatively ease of parallelization for achieving high-throughput systems, their complex design principles compared to straight channels make them more difficult to further modification of channel cross-section.

Lastly, using a sheath flow with different viscosity from the particle suspension could create a sharp shear gradient point inside the channel at the interface of two

adjacent fluids in which the direction of shear-gradient lift force switches, as a result an equilibrium point called “inflection point focusing” is formed [115]. By means of a 3-inlet co-flow channel while particle mixtures pumped through central inlet (Figure 2-14a) and manipulation of the viscosity ratio between the adjacent fluids, size-dependent particle equilibriums were established. The larger particle sizes were unexpectedly influenced by the shear-gradient force and migrated to the channel center under the conditions smaller particle sizes remained near the fluid interfaces. Nonetheless, this channel, like other previous straight channels reviewed, suffers from poor separation resolution and low particle volume fractions ($V_f \ll 0.5\%$). Curiously, using a similar co-flow system but switching the particle/cell mixture inlet from center to side streams (Figure 2-14b). Zhou et al. came up with the effect of shear-induced diffusion when the particle/cell concentration gradient is high. They showcased separation of 18.7 μm fluorescent polystyrene particles and cancer cell line (Hep G2) from whole blood diluted only 2x with $\sim 90\%$ efficiency and $\sim 97\%$ removal of blood cells.

A new type of inertial focusing principle was reported recently by Toner’s group. To overcome the infinity length required for focusing of submicron particle sizes due to low particle Re number ($Re < 0.01$), an oscillatory flow inside a channel, constantly alternating the flow direction, was introduced [116]. A focusing of 500 nm particle and bacterium were demonstrated. While its practical applications have yet to be examined, this method may be of interest for enrichment and isolation of submicron bioparticles, e.g. bacteria, platelet, exosome, at micro liter scale. A new dimensionless Peclet-like number (Pe) was scaled based on the ratio of inertial migration velocity versus diffusion rate, showing dominating inertial force over particle diffusion when $Pe \gg 1$ (Figure 2-14c).

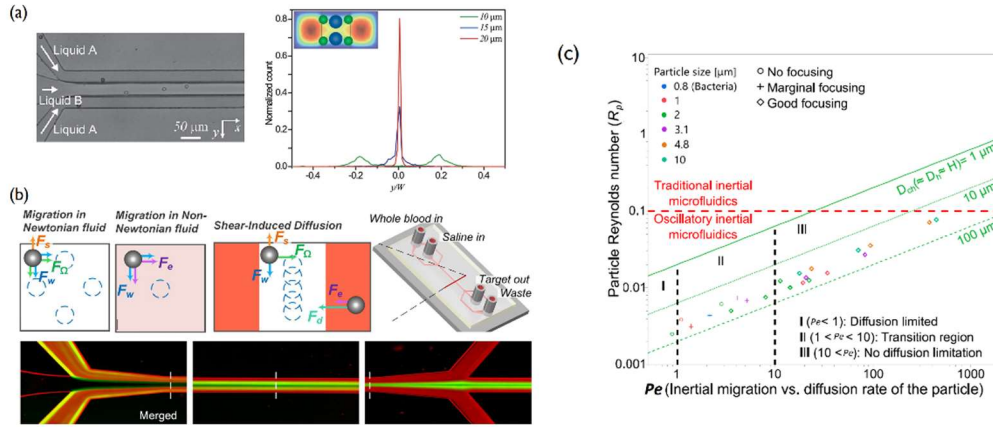


Figure 2-14 (a) A 3-inlet co-flow system using inflection point focusing while larger particles migrated towards center under the influence shear-gradient force [115] (b) migration of 18.7 μm (green) spiked in whole blood from side streams towards sheath flow at center under the shear-induced diffusion lift force arise from high concentration gradient [117] (c) Dimensionless Peclet-like number vs. particle Re number showing oscillatory inertial focusing at low $R_p < 0.1$ [116].

2.4.2 Curved channel

Generally, the curvature of a channel generates centrifugally-induced pressure gradient along the radius; consequently, it induces transverse motion of fluid at the midplane outwards while the slower-moving region near the outer wall moves inwards close to top and bottom wall [86]. Thus, a pair of vortices are developed in a vertical plane (Figure 2-15). The magnitude of secondary flow is characterized by non-dimensional Dean number ($De = Re \sqrt{D_H/2R}$) which is like Re number for a straight channel.

Although curved microchannels had been utilized as micromixers [118, 119] by exploiting Dean vortices, Ookawara et al. [89, 120] studied a curved (semicircle) microchannel for the first time to concentrate microparticles (Figure 2-15a). However, their design principle was only based on Dean vortices without recognizing the shear-gradient lift [25, 30]; while bigger particles mainly moved to

the outer wall whereas small particles remained dispersed. The channel cross-section was 200 μm wide and 170 μm high, with a 20 mm radius of curvature. This structure was employed to classify particles with an average diameter of 7, 10 and 20 μm in a suspension with 0.06 wt. %, operating at Re number ranging from 150 to 600. In another study, Gregoratto et. al [121] proposed a spiral microchannel for particle concentration which was adopted from Dean vortex-based micromixers [119] having extremely low AR of 1/15 to 1/8. A 3.5-fold concentration of 10 μm was achieved.

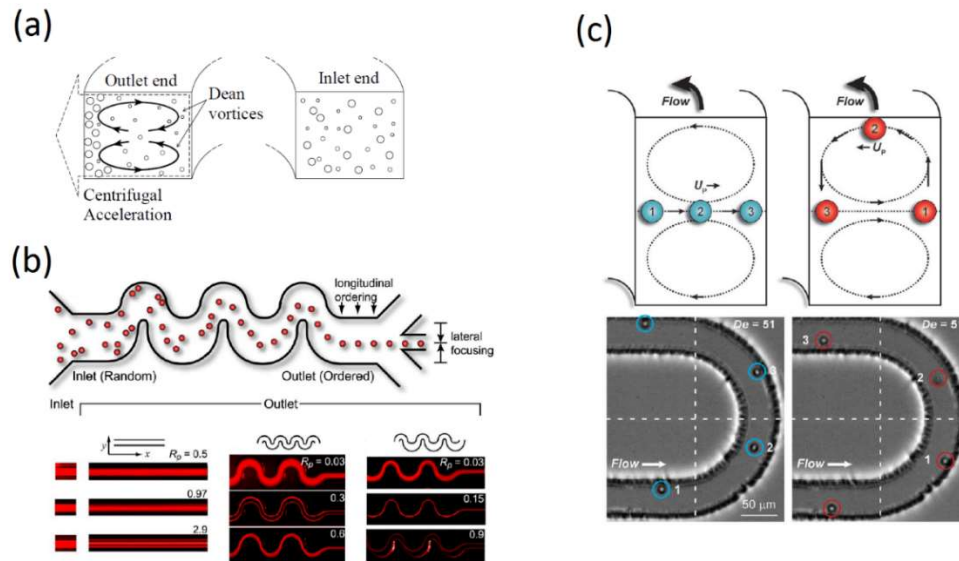


Figure 2-15 (a) A semicircle microchannel exploited to classify particles of a suspension [89] (b) inertial focusing by using a straight, symmetric and asymmetric microchannel [25] (c) discriminated routes of inner (blue) and outer (red) focused particles traveling along a single turn [122]

Particle and cell focusing by utilizing inertial lift and Dean drag force was exclusively explored by Di Carlo and his colleagues [25] in 2007 for the first time. They used an asymmetric microchannel (Figure 2-15b) and showed the effect of inertial force emerging under specific circumstances when particle size confinement ratio was $a/D_H > 0.07$ and particle Reynold number was in order of $R_P \sim 0.1$. The four stable equilibrium positions within a straight square channel were reduced to one when a curvature was introduced to the flow path, i.e. using secondary flow. Consequently, the interplay between secondary drag force and inertial lift force

determines the quality and quantity of focusing phenomenon. Also, changing straight microchannel to the asymmetric channel significantly decreased required particle Reynolds number from 2.9 to 0.15, thereby shortening focusing length from ≈ 1 cm to ≈ 3 mm. To experiment the effect of non-neutrally buoyant particles on inertial focusing, polystyrene particles (10 μm diameter and $\rho=1.05$ g/ml) were suspended in mediums with different densities (0.78 to 1.23 g/ml) from the particle density. Interestingly, no deviation was found concerning inertial focusing, implying that the only effective force in transverse plane is Dean drag force in comparison to the centrifugal or buoyancy force.

Theoretically, there is an optimal Reynolds number to achieve particle focusing since exceeding a critical threshold demolishes the balance between the inertial lift and the secondary drag force; therefore, dominating secondary drag forces switch the function of curved channel to mixing. Gossett and Di Carlo [122] designed an experiment in a single turn with a low-AR channel of 0.55 (30 μm wide and 54 μm high) to clarify the effects of secondary drag in concert with inertial force. They observed the formation of two focusing points close to long faces at low $De=4$, whereas gradual increase of De number to 43 led to first, transverse migration of particles from the inner wall across the width towards the outer wall followed by lateral migration of outer focused particles towards the inner wall as shown schematically in Figure 2-15c; this proves the dominating impact of secondary drag against weak centrifugal force. The weighted centrifugal forces were scaled at least one order of magnitude lower than Dean drag force; hence, the only influential radial force acting along with inertial lift forces is Dean drag force [88]. Moreover, the ratio of inertial lift to Dean drag forces was scaled as follows, considering finite-sized particle [122]:

$$R_f = \frac{F_L}{F_D} \sim \frac{2Ra^2}{D_H^3} \quad (2.9)$$

where R is the radius of curvature; this ratio (R_f) is a main factor in designing inertial microfluidics while the lowest critical value obtained experimentally is ~ 0.037 to achieve particle focusing.

A double spiral structure was first introduced by Seo et al. [123, 124] as a membrane-free filtration method based on particle size, but the proposed spiral was not able to perform separation (Figure 2-16a). The double spiral conduit (300 μm width and 100 μm height, $AR=3$) consisted of 12 turns. A microparticle solution of 10 μm and 6 μm run through the double spiral showed the migration of bigger particles moving (clogging ratio $K=a/H=0.1$) towards the inner wall whereas smaller particle ($K=0.06$) remained dispersed randomly. However, the low particle Re number in the order of 0.1 meant that the strong effect of shear-gradient lift and then inertial particle focusing phenomenon were not observed in this instance.

A spiral channel structure with the aid of sheath flow was utilized by Bhaghat et al. [33] for complete separation of microparticles (Figure 2-16b). Their design principle was based on inertial focusing and its interaction with Dean vortices to develop size-dependent equilibrium positions. They demonstrated focusing of larger particles' stream with $K=0.14$ close to the inner wall while smaller particles with $K=0.038$ were swept away towards the outer wall under the influence of Dean drag force without focusing. Next, Kuntaegowdanahalli et al. [125] demonstrated multi-particle separation simultaneously as a unique feature of spiral design with multi branches at the outlet (Figure 2-16c). The concept of this design was similar to Bhaghat device [33] but the channel height, i.e. particle clogging ratio K , was manipulated to change the ratio of the inertial force to the drag force (Equation 2.9), resulting in different size-dependent equilibrium positions across the channel. The experimental results showed that reducing particle clogging ratio K brings about particle migration towards outer wall under the dominating Dean drag force for a given Re number. They achieved in separating 10 μm , 15 μm and 20 μm particles by using a spiral at $De=14.4$.

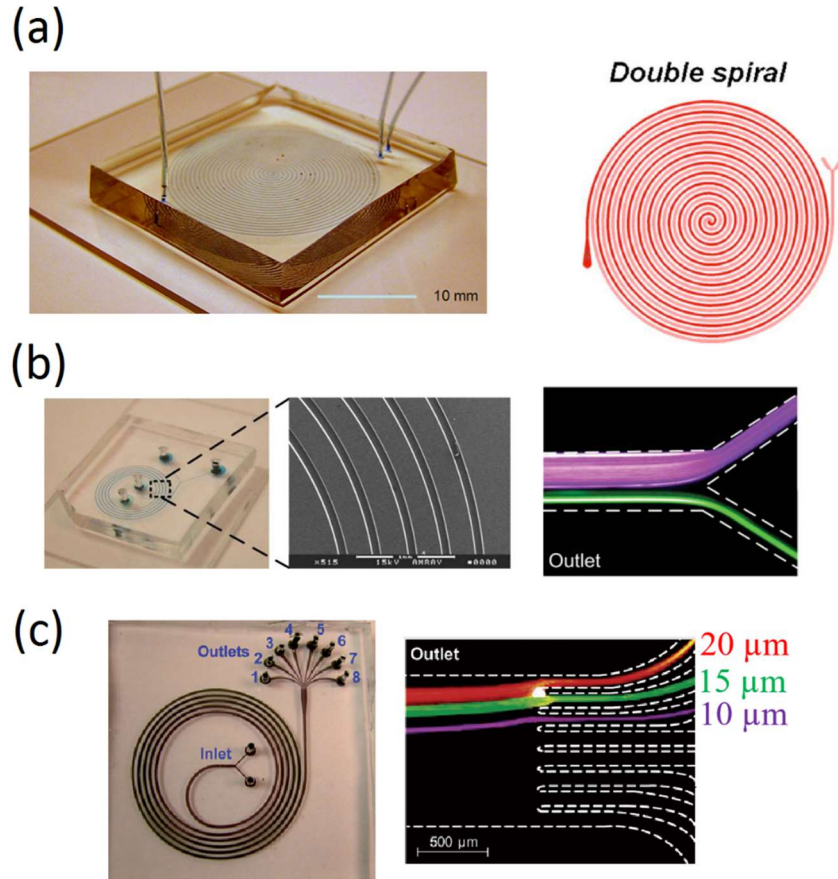


Figure 2-16 (a) Double spiral chip was functionalized for filtering of microparticles [123, 124] independently (b) segregating 1.9 mm (colored purple) from 7.32 mm (colored green) particles completely where flowing at $De = 0.47$ [33] shown by superimposed fluorescent images. (c) spiral microchannel for separating different-sized particles (10, 15 and 20 μm particle)[125]

Further investigation was carried out in a spiral channel with variable high-AR channel where the width was increased gradually [88] in order to have the flow rate increased while keeping Re number low (Figure 2-17a). No focusing was observed for particles with clogging ratio below $K=0.1$. On the other hand, regardless of particle clogging ratio, when De number was increased to ~ 25 , the particles started defocusing, indicating that drag forces have overcome inertial forces (Figure 2-17b).

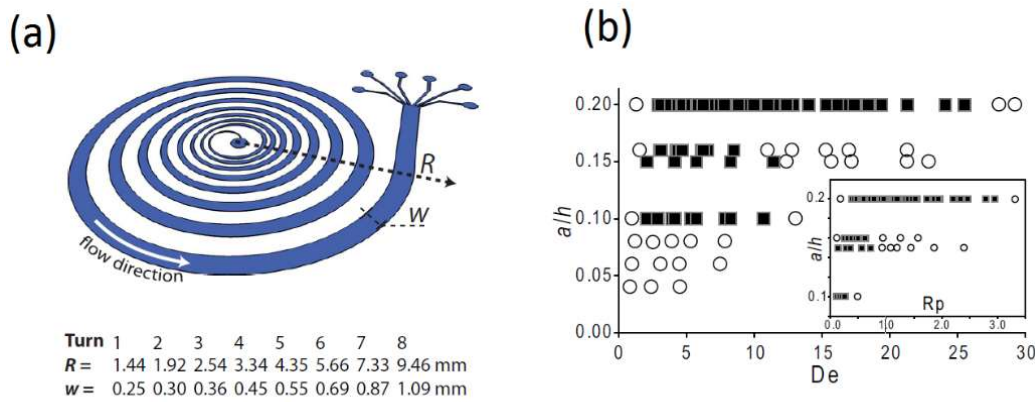


Figure 2-17 (a) spiral microchannel designed for separating multi-particle size and its width is increasing along the spiral route (b) Focusing map based on particle diameter to channel height Vs. De number while solid square shows focused point and circle is representative of unfocused points [88].

Martel and Toner [126] carried out a comprehensive experiment on the dynamics of particle focusing in spiral microchannels, with AR ranging from 1 to 8, while the particle clogging ratio was kept constant at $K=0.2$ (Figure 2-18a). Generally, increased hydraulic diameter (D_H) through enlarged channel width while the height was constant, resulted in decreasing lift force due to flatter velocity profile as seen in Figure 2-18b; however, the Dean drag force went up with scaling factor $De^{1.5}$. The effect of Dean number was investigated first by reversing the direction of flow in spiral channels (see Figure 2-18c), decoupling Re and De number from each other, while the Reynolds number remained constant. The distribution of minimum streak width was less influenced for increasing De number in comparison to decreasing De number condition. Also, increasing-Dean modes resulted in $\sim 25\%$ higher volumetric throughput for higher AR of 8; however, decreasing-Dean modes led to larger stable particle focusing.

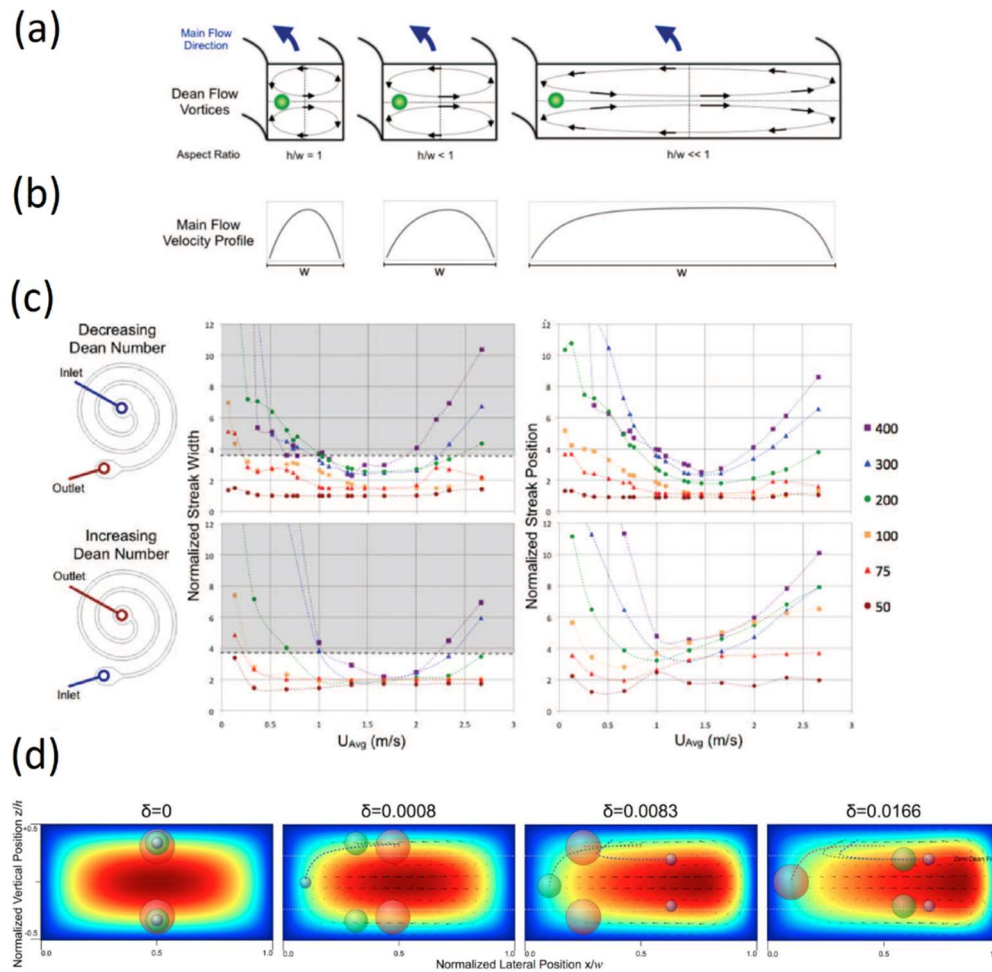


Figure 2-18 (a) Schematic counter-rotating Dean flow in a curved and low aspect ratio cross-section of microchannel while shows (b) main flow velocity distribution (c) effect of De number for decreasing (top) and increasing (bottom) condition on streak width which display the distance normalized by particle diameter from inner wall; the gray part shows the streak width is more than 3.8 particle size [126] (d) particle equilibrium location across the channel cross-section for different flow condition and particle sizes [84]

To further elucidate the effects of Dean number and Re number independently, different curved channels with curvature ratio $\delta = D_H/2R$ ranging from $\delta=0$ (straight channel) to $\delta=0.0166$ were examined. A channel with AR of 2, height of $50\ \mu\text{m}$ and fixed length of $40\ \text{mm}$, and particle clogging ratios $K=a/H$ of 0.08, 0.2 and 0.3 were investigated [84]. They illustrated the locations of the 3D particle streams across the channel for different flow conditions and particle sizes (Figure 2-18d). Regardless

of flow condition, a dimensionless number of $K/\delta^{0.5}$ was found; when this number reaches above 2.66, it was observed that the particles migrate towards the inner wall. Larger particles with $K=0.3$ migrated toward the inner wall regardless of channel curvature ratio or De value, implying that the equilibrium was mainly dominated by the net lift force. Nonetheless, particles with $K \leq 0.2$ were influenced by Dean vortices and driven toward the outer wall at high De magnitude.

The spiral microchannel was applied in many biological applications such as CTC enrichment [81], blood plasma extraction and blood cell fractionation [127] based on size difference. However, the low separation resolution not only results in low purity and yield but also necessitates large dilution in processing samples such as blood. To enhance the separation resolution, Wu et al. [48] designed new spiral microchannel with a trapezoidal cross-section (Figure 2-19a) to separate red blood cells (RBCs, 6-8 μm discoid) from leukocytes comprising polymorphonuclear (10-12 μm) and mononuclear (7-10 μm). By providing more space between equilibrium position of red blood cells (which exist in high numbers) and leukocytes (which are larger in size but smaller in numbers), the working blood cell concentration can increase by 15-fold (hematocrit $\approx 1.5\%$) relative to that of conventional rectangular spiral channels (hematocrit $\approx 0.1\%$) [127]. The main key to increase throughput, or volumetric flow rate, is to enlarge the spiral channel width; however, the main factor for particle equilibrium position is the particle size relative to the channel height (K) [128]. Hence, high throughput is achieved by increasing the AR of trapezoidal spiral channel to ~ 7 [49].

Figure 2-19b shows the movement of $K=0.32$ particles (the ratio of particle size to shorter side wall that is used as a definition of K for trapezoidal channels in this study) inside a trapezoidal spiral channel. Similar to rectangular spirals [128], first equilibria is seen to have moved towards inner wall but suddenly the focusing point switched to outer wall under the influence of vortex cores which are located close to the outer wall. This sharp transition of particle equilibrium from the inner half to the outer half is a function of particle size and flow rate; while smaller particles

underwent transition earlier than that of bigger particles, creating a considerably high separation resolution (Figure 2-19d).

Warkiani et al. [44] applied a trapezoidal spiral with $AR=7.5$ [48] for enriching CTCs from patients' RBC-lysed whole blood samples diluted 2x where larger cells (CTCs) focused against the inner wall whereas the rest of hematological cells (leukocytes) trapped in Dean vortex cores near the outer wall (Figure 2-19c). Unlike the conventional rectangular cross-section design for CTCs isolation from whole blood [43, 45, 96, 129], applying trapezoidal cross-section eliminated the need for sheath flow, helping automation and ease of use of this technique; nevertheless, the fabrication process was more expensive due to micro-milling methods compared with the routine photolithography method. Also, the size-dependent critical flow rate corresponding to sharply shifting of particle equilibrium towards outer wall yet to be explored.

Moreover, although the fundamental theory of particle equilibration has been developed based on force balance between the inertial force and Dean drag force, this theory is however unable to explain particle migration in curved channels when the secondary flow direction alternates, such as in double spirals [81, 130] and serpentine channels [40, 82]. Alternating secondary flow path brings about equilibration of relatively larger particles at the middle whereas these particles migrate close to the inner wall in a corresponding spiral channel. Surprisingly, numerical simulations of those channels with alternating secondary flows without modeling of the inertial force agree with experimental results while there is still no numerical multiphase model based on continuum approach as well as finite volume method (FVM) or finite element method (FEM) for a spiral channel.

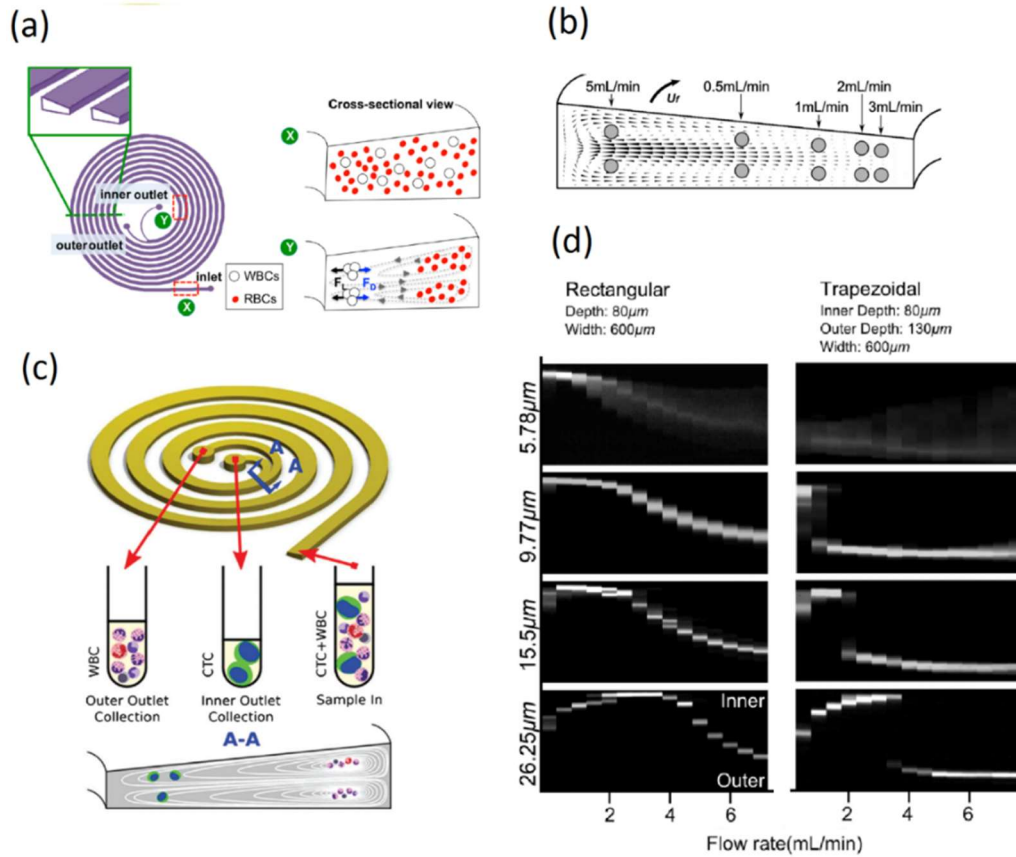


Figure 2-19 (a) Spiral chip with trapezoidal cross section for separating leukocytes from RBCs [48] (b) schematic particle equilibrium position within a trapezoidal cross-section for different flow condition [49] (c) high throughput CTC enrichment by using slanted trapezoidal spiral [44] (d) fluorescently labeled particle equilibrium position inside a rectangular and trapezoidal spiral for varying flow rates [49].

One of the main hindrances so far in separation of microparticles in the range of 1-4 μm is the channel height; reducing the channel height to less than 50 μm ($H < 50$ μm) results in extraordinary hydraulic resistance. Xiang *et al.* [131] designed an Archimedean spiral chip with $AR=3.2$ and $H=50$ μm, as shown in Figure 2-20a, in order to separate particle suspension containing 2.1 μm ($a/H=0.042$) and 4.8 μm ($a/H=0.096$).

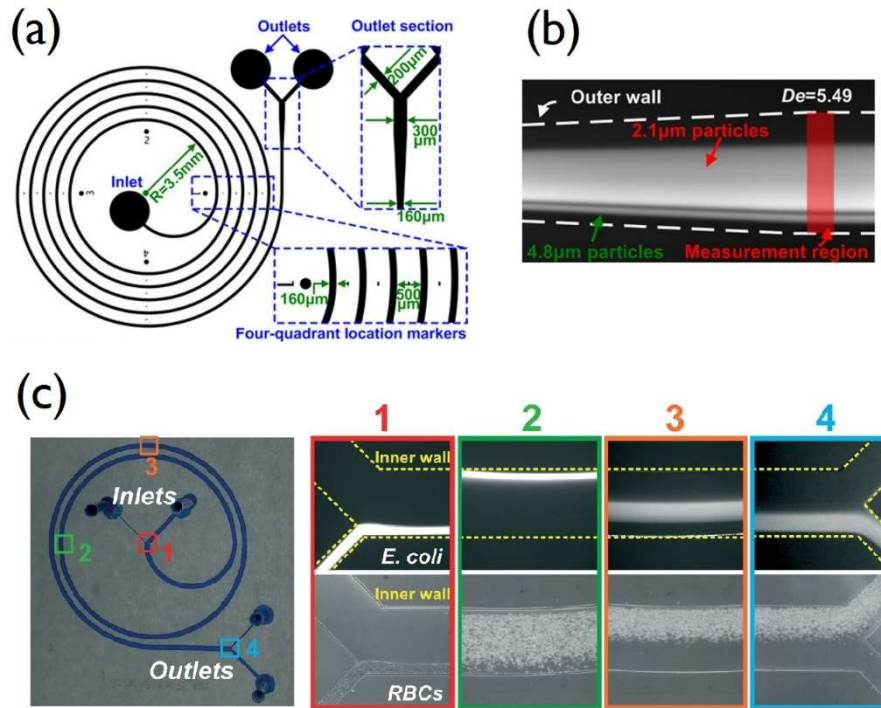


Figure 2-20 (a) Images of spiral chip separating 2.1 μm and 4.8 μm particle diameter while the small particle size is below the critical threshold for inertial focusing ($a/H=0.042 < 0.07$) (b) Separation of 4.8 μm from 2.1 μm particle diameter by using spiral while 4.8- μm particles equilibrate close to inner wall in a particle-free zone of 2.1 μm particle diameter [131]. (c) Separation of *E.coli* ($K\sim 0.01$) from 3x diluted blood in a spiral channel using sheath flow, 500 μm (W) \times 80 μm (H) [47].

In this experiment, it was found that for particles of 2.1 μm , there were two particle-free regions, in the proximity of the inner and the outer wall. A suspension consisting of a mixture of 2.1 μm and 4.8 μm particles with extremely low concentration of $<0.005\%$ was successfully fractionated at $De=5.49$, as shown in Figure 2-20b, although the resolution was poor. Further investigations demonstrated that particles with clogging ratio of 0.042 ($K<0.07$) were mainly governed by Dean drag forces and entrained in two vortices at the upper and the lower halves of the channel cross-section [132]. With the aid of sheath flow, the spiral channels outperformed with regards to focusing and separation of small sized particles with $K\sim 0.01$ [46, 47], such as separation of bacteria ($<1 \mu\text{m}$) from 3x diluted blood

(Figure 2-20c); however, its throughput and scalability are impeded by some difficulties such as massive parallelization and operation.

Ramachandraiah et al. [133] investigated the effects of radius of curvature and channel AR on inertial particle focusing ($K=0.2$) in a single U-turn ($H=50\text{ }\mu\text{m}$) providing uniform Dean flow in contrast to spiral channels. They reported inertial focusing for a wide range of channel AR ranging from 1 to 10, and De number varied from 2 to 80; however, as AR increased to 20, the particle focusing was lost. Their results implied that reduction of curvature ratio led to reduction of Re (or throughput) while keeping the lateral particle focusing fixed or i.e. maintaining the ratio of F_L/F_D constant. Consequently, altering a spiral channel to an arc is another potential design which can significantly streamlines parallelization for achieving high-throughput device by utilizing trapezoidal cross-section.

Table 2-2 summarizes the broad range of applications demonstrated so far using Dean-coupled inertial focusing (particularly spiral channels) along with their major characteristics.

Table 2-2 Application of Dean-coupled inertial microfluidics using a spiral, double spiral and U-shaped channel structure

Application	Sample	H (μm)	AR	De	Volumetric flow rate ($\mu\text{L}/\text{min}$)	Throughput (cells/min)	Yield	Purity	Remark	Ref.
Separation	10, 15 and 20 μm mixture	130	3.84	14.4	3000	-	90%	-	increasing De	[125]
	Neuroblastoma ~15 μm and glioma cells ~8 μm	120	4.2	11.8	-	1E6	80%	-		
Flow cytometry	6 μm particle	50	2	2.3	100	126000	-	-	decreasing De	[134]
Particle separation	10 and 3 μm particle	50	5 to 20	-	3500	-	98.5 % for 10 μm	-	variable AR /decreasing De	[88]
							92.5 % for 3 μm			
CTC (MCF-7 and HeLa) enrichment	diluted blood 0.8% hct	50	6	4	333.3	3.33E7	96.8 %	-	double spiral	[81]
CTC (HeLa) enrichment	20x diluted blood	85	3.5	10.8	1000	2.5E8	90.5 %	-	double spiral	[130]
Leukocyte isolation	diluted blood 1.5% hct	70 to 100	7.1	-	800	-	96.2 %	86.8 %	trapezoid/ increasing De	[48]
Blood plasma extraction	diluted blood 0.45% hct	75	3.3	-	1000	-	-	~100 %	small inner most radius of 2 mm /Decreasing De	[127]
Blood cell fractionation	diluted blood 0.1% hct	110	4.5	-	1800	~1E5 WBCs	~95% WBCs	-	decreasing De	[127]
						~1E7 RBCs	~94 % RBCs			
CTC isolation	Diluted blood 20% hct	160	3.125	-	50	-	>85%	-	using sheath fluid/ Decreasing De	[43, 135]

Continued **Table 2-2**

Application	Sample	H (μm)	AR	De	Volumetric flow rate ($\mu\text{L}/\text{min}$)	Throughput (cells/min)	Yield	Purity	Remark	Ref.
CTC isolation	7.5 mL lysed blood in 10 min processing	160	3.125	-	-	-	99.99 % WBC depletion	-	multiplexed spirals / Clinical validation	[45, 129]
							>76 % CTCs			
CTC isolation	7.5 mL lysed blood in 10 min processing	80-130	7.5	-	1700	-	>80% CTCs	-	trapezoidal spiral/ increasing De	[44, 136]
Isolation of Circulating Fetal Trophoblasts	10 mL blood	80-130	7.5	-	1700	-	79%	-	trapezoid spiral/ increasing De	[137]
Sorting of microalgae cells	mixture of <i>P. tricornutum</i> and <i>T. suecica</i> cells	80-130	7.5	-	1000	-	-	95%	trapezoid spiral/ increasing De	[138]
Particle filtration	10 μm and 2 μm	50	10	-	4250	-	92%	-	single U-shaped/high AR	[133]
Cell filtration	Leukocytes from diluted blood 0.5% hct	50	5	37	2200	-	78%	-	single U-shaped/high AR	[133]
Blood plasma extraction	diluted blood 2.25% hct	50	3	-	700	-	38.5 %	~100 %	decreasing De /3.5 mm radius	[42]
Bacteria isolation	diluted blood ~15% hct	80	6.25	-	150	-	75%	-	decreasing De / using sheath flow	[47]
Enrichment of single neural stem cells (NSCs)	chemically dissociated neurosphere clusters	150	3.33	-	1000	-	84%	-	decreasing De /NSCs 8-14 μm and cluster 40-60 μm	[139]
Sorting MSCs	hMSCs population	140	3.57	-	2500	2.5E5	-	-	decreasing De	[140, 141]

Continued **Table 2-2**

Application	Sample	H (μm)	AR	De	Volumetric flow rate ($\mu\text{L}/\text{min}$)	Throughput (cells/min)	Yield	Purity	Remark	Ref.
Blood plasma extraction	diluted blood 0.5% to 1% hct	70-40	12.5		1500-2000	-	-	100%	decreasing De / Multiplexed 16 spirals throughput reached to 24 mL/min	[34]
Cell retention system	CHO cells	-	-	-	6000	-	95%	-	trapezoidal spiral/Decreasing De / Multiplexed spirals' throughput up to 500 mL/min for CHO	[2]
	yeast cell				2000		90%			
Cell retention	CHO cells	260-80	12.5	-	4000	~160E6	84%	-	trapezoidal spiral	[142]
Enrichment of <i>Cryptosporidium parvum</i>	water	30	5.6	-	400	-	100%	-	-	[143, 144]
Isolation of functional mitochondria	crude cell lysate	50	2	-	~20	-	90 %	-	using sheath flow	[145]
CTC (MCF-7) isolation	100x diluted blood	40	3.75	-	400	-	87.9 %	-	2 stage separation	[146]
Neutrophil purification	2x diluted lysed blood	115	4.34	-	130	-	>80%	-	using sheath fluid	[147]
Sorting Algal cells	water	100	3.5	-	3200	16.2E5	77%	-	non-spherical plant cells	[148]
Enrichment of neural stem cells	neural stem cells (NSCs), derived from induced pluripotent stem cells	160	3.125	-	3000	-	93%	-	using sheath fluid	[149]
Syringe cell concentrator	Particle/cell suspension	100	5	-	2500	-	>92%	-	3D printed	[150]

Continued **Table 2-2**

Application	Sample	H (μm)	AR	De	Volumetric flow rate ($\mu\text{L}/\text{min}$)	Throughput (cells/min)	Yield	Purity	Remark	Ref.
Separation of <i>C. elegans</i> embryos	Mixed-age worm population	220-160	6.25	-	5000-10000	-	97%	-	Trapezoidal/non-spherical worm	[151]
Mesenchymal stem cell enrichment	bone marrow sample	160	3.125	-	1600	$\sim 3\text{E}6$	73%	$13.1 \pm 2.9\%$	-	[152]
Separation of non-motile sperm	Mixed RBCs and sperm	50	3	-	520	$\sim 1\text{E}6$	81%	99%	-	[153]

2.5 Downstream processing of stem cell therapy manufacturing and challenges

2.5.1 Stem cell therapy manufacturing

Cell therapeutics using human-derived cells are deemed as the next generation of medicine to combat a wide range of incurable diseases such as neurological disorders, cancers, diabetes and heart disorders [154]. Some notable cell therapies in clinical trials involve mesenchymal stem cells (MSCs). There were 374 number in 2015 using MSCs for therapeutic purposes [155] targeting disease and injury of various organs such as skin, lung, heart, liver and kidney due to their anti-inflammatory properties and trophic influence on tissue repair [156]. For universal-donor (otherwise known as allogeneic) stem cell therapy, a master cell bank is first developed before cells are expanded in vitro to produce approximately 10^8 to 10^9 cells per dose, depending on body weight and indication [157].

To meet the large number of cells required for stem cell transplantation, a paradigm shift is therefore inevitable from 2D culture flask to a highly dense 3D cell culture environment to achieve throughput of up to 100 billion to trillion cells per lot [158]. For anchorage-dependent cell types such as mesenchymal stem cells, one alternative approach is using micro-beads (~ 100 to ~ 300 μm size) as carriers, shown in Figure 2-21, to scale up expansion by increasing the surface to volume ratio [159, 160].

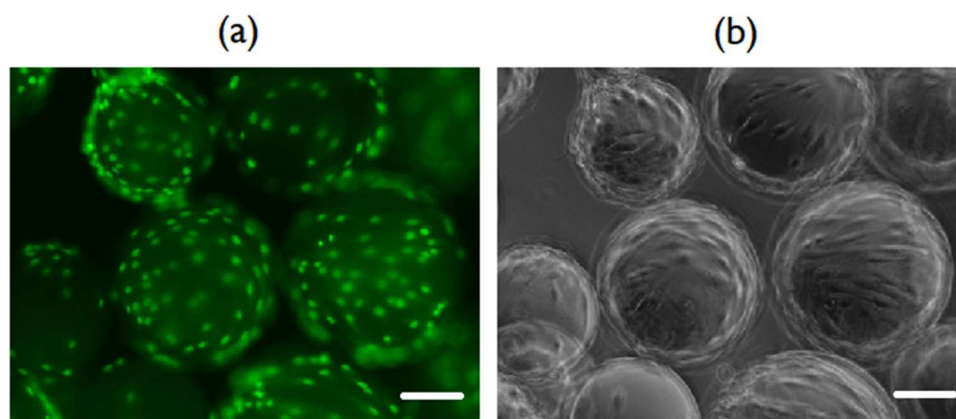


Figure 2-21 (a) Nucleolus-stained hMSCs on Synthemax II hydrogel microcarriers after 4-5 days in culture and (b) its phase-contrast image (Corning). Scale bars are 100 μm .

2.5.2 Microcarrier-based bioreactor

Developing bioreactor technology goes back to mass production of molecular-based biopharmaceutical industry such as protein or vaccine productions. Bioreactor technologies have been developing in cell therapy by growing clinical trials and stimulating commercial outlook. In addition to large-scale cell manufacturing in vitro, bioreactors offer reduced manufacturing cost and more controls over biophysical and biochemical properties of cell culture environment such as pH, dissolved oxygen, temperature, nutrients supply and removal of metabolic-derived waste, thereby enhancing product quality and consistency [161]. Among different types of bioreactors, stirred tank bioreactors are well-established as a large-scale biopharmaceutical manufacturing platform due to its reliability and scalability attributes [162].

Microcarriers (MC) are commonly used in stirred tank bioreactors to culture adherent cells. This helps increase mixing performance since agitation is an essential part of stirred-tank bioreactors to provide homogenous culture environment supplying oxygen and nutrients. Different commercial types of microcarriers have been demonstrated for MSC culture. Microcarriers are available in different materials including polystyrene and dextran.

Microcarriers are generally selected based on material, size and porosity. Cell growth and multipotency of MSCs are functions of cell line and media, and these parameters are interdependent. Accordingly, different surface treatment and coatings have been developed to enhance cell attachment and growth for different cell types. Porous MCs have also been developed; while these MCs seem to provide a heterogenous culture environment, the challenge in harvesting of MSCs from such MCs result in low yields [163].

Despite prominent advantages of microcarrier-based bioreactors, this technology also faces some hurdles such as separation of cells from microcarriers and removal

of particulates; microcarrier fragments [164] generated due to high shear rate in bioreactors (Figure 2-22).

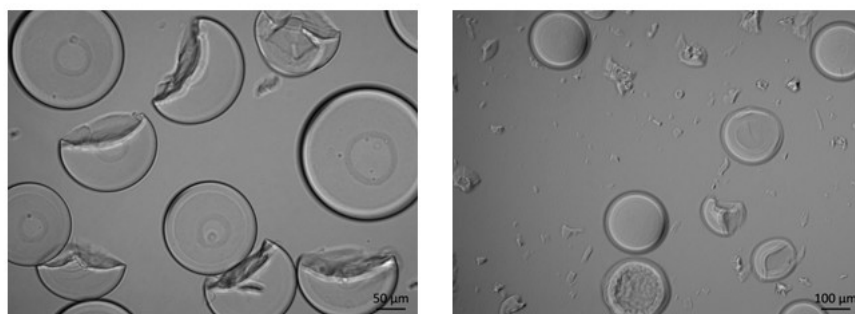


Figure 2-22 Cytodex 3 breakage in a 500-mL spinner flask (Corning) with 120 rpm rotational velocity at day 7. The medium is sterilized DI water.

2.5.3 Particulates type in cell therapy industry

Particulates are classified based on their source, size, shape and composition. Particulates are generated from diverse sources as described in Figure 2-23. In contrast to extrinsic particulates, some particulates are introduced to the product through formulation and packaging processes. Inherent particulates such as protein aggregates and cell debris, are usually accepted as part of the final cell therapy product [165, 166].

Furthermore, employing single-use technology is drawing more attention in biologics manufacturing. Some of significant advantages of single-use systems, for instance elimination of cleaning, sterilization and validation steps, have inspired cell therapy industry to approach single-use systems as a cost-effective mass manufacturing [167-169]. Single-use lots, containers and bioreactors, however, introduce some impurities and hazardous materials such as polymer-derived substances originate from leachable component of wetted surface area during cell expansion process [170, 171].

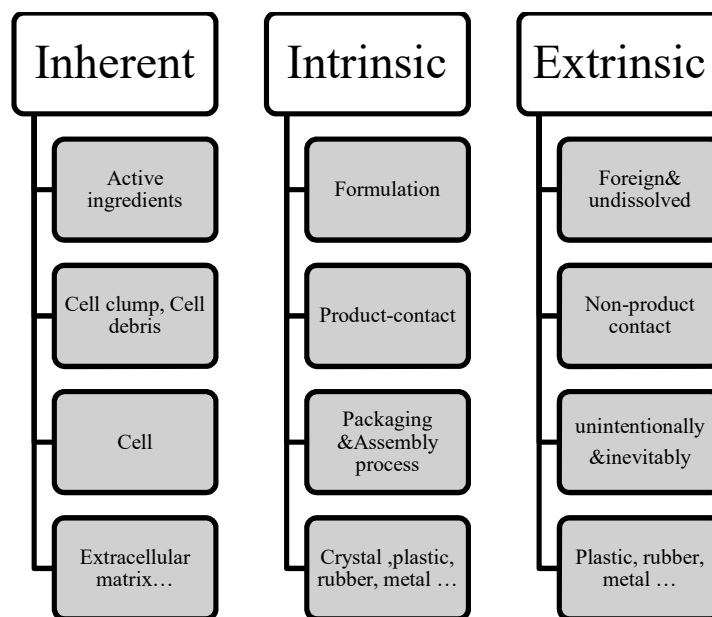


Figure 2-23 Different sources of particulates in cell therapy

Size of the particulates can range from 10 to 4000 μm and under Good Manufacturing Practice (GMP) guidelines, particles larger than 600 μm are categorized as a fibrous in nature [172].

Given that cell therapies are usually administered intravenously (IV), the final cell therapy product must comply with stringent regulatory standards of injectable drug products. While there have been little data on the effect of particulates in patients undergoing cell therapy clinical trials, some in-vivo experiments demonstrated serious harmful consequences of particulates. For example, a micron-sized particle ranging between 12 to 15 μm , when injected to a vein, have been shown to be trapped in the pulmonary capillaries. Furthermore, as for patients suffering from impaired immune system, non-sterile particulates can also cause adverse effects [165, 173]. Unfortunately, in contrast to protein-based products, it is not possible to carry out downstream filtration and purification step using membrane technology, as cell sizes fall within the range of that of the particulates [166, 172, 174]. Patient safety, therefore, is a major challenge which needs to be addressed to pave the way for successful development, and ultimately commercialization of cell therapy products [175].

2.6 Summary

In this chapter, the inertial microfluidic technology is reviewed while concentrating on particle focusing dynamics. Next, some potential applications and new challenges in bioprocessing and downstream cell clarification respectively are introduced.

Inertial focusing has been used in numerous applications including particle and cell sorting, filtration and separation. Although the fundamentals of inertial-induced lift force have been fully established, there are still no comprehensive explicit models to predict the inertial force inside channels with complex non-rectangular cross section such as trapezoids. Moreover, while spiral channels with exclusively trapezoidal cross-sections have been developed and applied widely due to high-throughput and high-resolution separation, the mechanism is not yet fully understood. Thus, inertial focusing in straight trapezoidal microchannels is first studied to provide a better understanding of inertial lift force without the presence of secondary flow (Chapter 3).

Despite efforts to establish Dean-coupled inertial focusing dynamics particularly for spiral channels, the main literature is limited to the scale of cell size ($\sim 10\ \mu\text{m}$), i.e. low channel hydraulic diameter ($D_H \ll 0.5\ \text{mm}$). However, a diverse range of particle sizes exists in many industrial applications such as bioprocessing and cell therapy industries where particle sizes have been described to be greater than $50\ \mu\text{m}$. Scaling up channel hydraulic diameter is crucial when dealing with larger particle sizes to prevent clogging of the channel. This thesis studies the impact of scaled-up channel hydraulic diameter on Dean-coupled inertial focusing. Ultimately, some developed scaled-up curved channels are utilized for filtration (Chapter 4 & 5) and separation (Chapter 6) in the context of bioprocessing.

Chapter 3 Inertial Particle Focusing Dynamics in a Trapezoidal Straight Microchannel

In this chapter, inertial focusing is experimentally investigated in a straight microchannel with a trapezoidal cross-section – without the presence of curvature-induced secondary flow. The impacts of slanted wall and particle clogging ratio as the two determining factors are mainly studied then. Remarkably, an almost complete transition of particle focusing with $K \sim 0.9$ ($45 \mu\text{m}$) from the longer side wall to the shorter side wall is demonstrated at extremely high particle Re number of $R_p \sim 85$. This phenomenon might shed further light into the mechanism of cross-laterally inertial migration of particles close to the wall (wall-effect lift force) through establishing a comprehensive numerical model in near future. Eventually, as a proof of principle, a trapezoidal straight microchannel is utilized for continuous filtration of a broader range of particle clogging ratio ($0.3 < K < 1$) in comparison to the rectangular straight microchannels ($W > H$, $0.3 \leq K < 0.5$).

3.1 Introduction

Cross-laterally migration of particles inside square and rectangular microchannels experimentally proved the wall-effect lift force when the inertial effect (i.e. particle Reynolds number $R_p = Re a^2 / D_H^2$, where Re is channel Reynolds number, a is particle diameter, and D_H is the hydraulic diameter of channel) goes beyond a certain threshold, $R_p \sim 1$ [25, 37]. Accordingly, Papautsky's group recently proposed a two-step particle focusing model for the rectangular cross-section channels which is in good agreement with the experimental results [39]. However, this model fails to explain the inertial focusing for a non-rectangular microchannels such as triangular [102]. The number of equilibrium positions inside a rectangular channel relies on

Re number ($Re = \rho_f U_{max} D_H / \mu$, where ρ_f is the density of fluid, $U_{max} \approx 2 U_{avg}$ is the maximum flow velocity, and μ is the dynamic viscosity of fluid), aspect ratio ($AR = W/H$, where H and W are height and width of the channel, respectively), and particle clogging ratio, $K = a/H_{min}$ [79]. The number of focusing points varies between 2 to 4 at the centers of long and short walls [35, 37, 38, 75, 104, 176, 177]. Mainly two equilibrium positions inside a rectangular microchannel, adjacent to the longer walls has been utilized for particle filtration [38, 99], fractionation [36], and flow cytometry [134, 178] when the AR varies considerably from unity. Recently experimental results demonstrated that the higher the clogging ratio K ($0.3 \leq K < 0.4$), the higher the AR ($2 \leq AR < 5$) will be to obtain two strong focusing streaks, i.e. narrower particle band width in the middle of long faces of channel [32, 79]. Generally, as the ratio of AR/K goes up, the particle band width increases [79] within the perspective of inertial microfluidics $10 \leq Re \leq 100$ [18, 27, 37]. In this study, AR of 2 and 4 is, therefore, chosen at which the best particle focusing is achieved.

Despite comprehensive experiments and numerical analysis of the lift forces in a rectangular [75, 79] and non-rectangular microchannels [102], which all possess planes of symmetry, less effort is made on the “flow field structure” of trapezoidal straight microchannels and its effects on inertial focusing. On the other hand, a rectilinear channel with trapezoidal cross-sections breaks down all planes of symmetry. Though trapezoidal cross-section has been exclusively applied in curved microchannels to alter the secondary flow structure – thereby improving the separation resolution [44, 45, 48, 49, 179] and filtration [34] – the channel AR ($AR = W/H_{min}$) ranged from ~ 7.1 to ~ 12.5 in previous works, which was relatively high, and the slope of slanted wall was limited to low degree ($\tan(\alpha) < 0.1$). Given the simplicity (operation and manufacturing) of straight microchannels compare to the spiral channels and ease of parallelization, it is believed that for certain type of applications, straight microchannels would be better candidates for particle sorting.

3.2 Theoretical Background

The lateral migration of neutrally buoyant particles dispersed in a fluid flowing through a channel originates from inertial lift force which is decomposed to shear-gradient (F_S) and wall-induced (F_W) lift forces. The difference in velocity around the finite-sized particle [26, 61] induces a dominating shear-gradient lift force across the channel height ($W > H$). Particles, therefore, migrate toward the top and the bottom wall in the rectangular channels (Figure 3-1a). In contrast, due to the dissymmetry in the corresponding trapezoidal channels, the equilibrium plane near the slanted wall is spoiled and thus particles are mainly driven toward the center and the bottom wall (Figure 3-1b). In this zone, adjacent to the wall, a cross-laterally wall-effect lift (F_{CL}) is dominant, driving particles toward the center of long wall in the rectangular channels [36, 39]. Nonetheless, altering the rectangular cross-section to the trapezoidal causes an asymmetry in the velocity profile while the core of maximum velocity declines toward the longer side wall, resulting in off-center turning point in the shear field, whereby lateral focusing shifts toward the longer side wall (Figure 3-1b).

According to analytical models developed earlier to justify the particle migration across the streamline [70, 180], shear-gradient forces are independent of particle rotation [26] and it should be noted the rotation-induced lift force is 3 orders of magnitude smaller than the shear-gradient lift force [66, 70]. The wall-induced lift force is triggered when the particle approaches the wall. The net inertial lift force scales with a^4 which was derived using the perturbation method [72] based on point-particle approximation, i.e. neglecting finite-sized particle [75] is as follows:

$$F_L = f_L \frac{\rho U_{max}^2 a^4}{D_H^2} \quad (3.1)$$

where f_L is a dimensionless lift coefficient which is a function of particle position for a definite channel cross-section and Re number [18] which can be decreased by increasing Re number [73, 74]. Recently it was experimentally shown that f_L in a channel with rectangular cross-section can be expressed as follows [39], where $W > H$:

$$f_L \propto \frac{H^2}{a^2 \sqrt{Re}} \quad (3.2)$$

Therefore, the net inertial lift force F_L scales with a^2 ($F_L \propto a^2$).

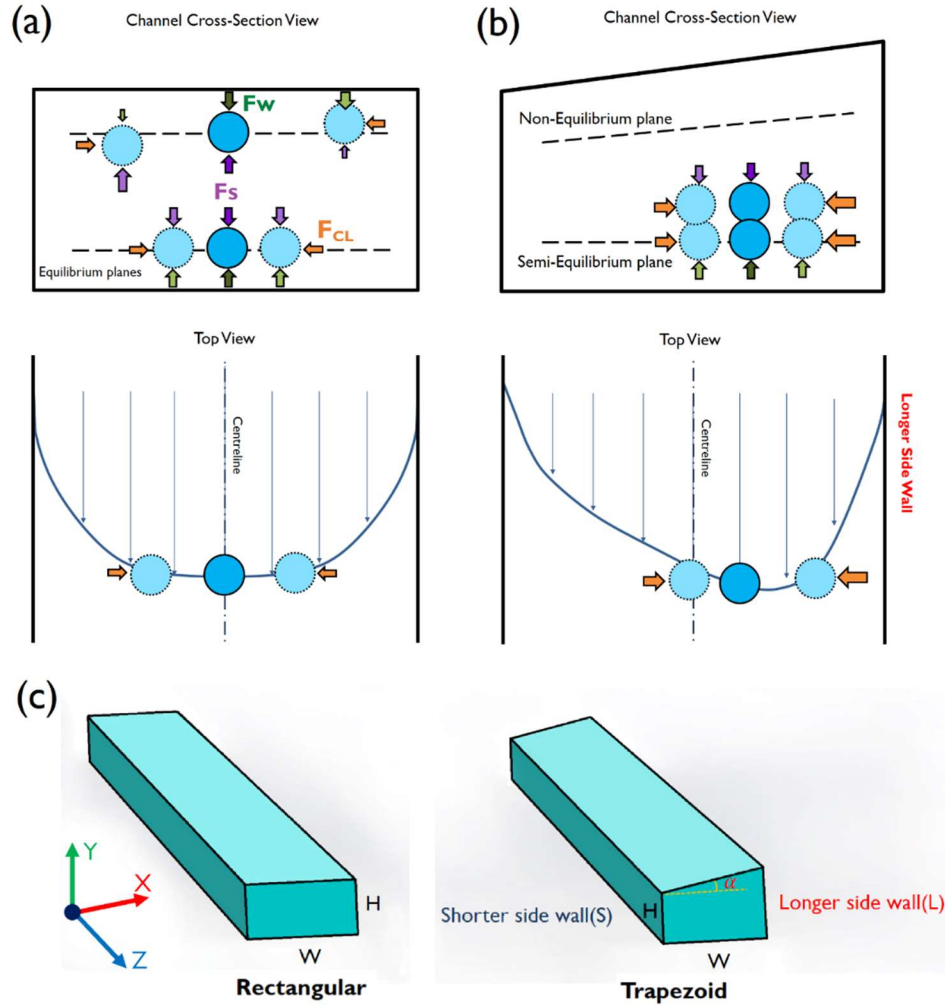


Figure 3-1 Schematic representations of shear-gradient lift force (F_s), wall-induced lift force (F_w) and cross-laterally wall-effect lift force (F_{CL}) in (a) a rectangular and (b) a trapezoid microchannel. (c) Rectangular and trapezoid straight microchannels designed; slope of the slanted wall is $\tan(\alpha)$.

3.3 Materials and Methods

3.3.1 Design and Fabrication

To study the new configuration of the inertial lift forces and their impacts on particle focusing within a microchannel with a trapezoidal cross-section, a series of trapezoidal channels was designed with $AR=2$ to 4 while the slopes of upper wall varied from ~ 0.2 to ~ 0.65 (Figure 3-1c, $\tan(\alpha)=0.2-0.65$). Also, a microchannel with rectangular cross-section ($\tan(\alpha)=0$) was fabricated not only to compare the results but also as a benchmark to verify the well-recognized particle focusing phenomenon for the designed rectangular channel. All the microchannels' length are 40 mm , with one inlet and one outlet. The length of microchannels having bifurcation is increased to 60 mm . The height of shorter side wall in the trapezoidal channels which is equal to the rectangular height was chosen to be $50\text{ }\mu\text{m}$ (Figure 3-1c). Rectangular microchannels were fabricated using standard soft lithography techniques described elsewhere [181], while trapezoidal channels were built using micro-milling technique described in our previous works [44]. The cross-sections of all fabricated channels can be seen in Figure S3-1 (Appendix A). Having been cured in an oven, the polydimethylsiloxane polymer (PDMS, Sylgard 184 Silicone Elastomer Kit, Dow Corning) replica was bonded to another thick layer of PDMS. First, the degassed mixed PDMS and curing agent (ratio 10:1) were cured for 1.5 hour in an oven at $80\text{ }^{\circ}\text{C}$. Next, after replica and blank layer of PDMS were peeled off, the inlet and outlet were pierced using a Uni-CoreTM puncher. Finally, the replica and blank layer were bonded irreversibly by oxygen plasma cleaner (PDC-002, Harrick Plasma) and cured for 3 hours in an oven at $70\text{ }^{\circ}\text{C}$. A $1/50''$ tubing (Tygon ND-100-80, USA) was used for the inlet and outlet ports.

3.3.2 Sample Preparation

Different neutrally-buoyant particle sizes (polystyrene $\rho\sim 1.05\text{ g/mL}$), with mean diameters of $10\text{ }\mu\text{m}$, $20\text{ }\mu\text{m}$, $45\text{ }\mu\text{m}$ (Fluoresbrite[®] YG Microspheres, Polysciences Inc, USA), and $15\text{ }\mu\text{m}$ (Dragon green, Bangs Lab Inc, USA), were used to

investigate the effect of particle clogging ratio (K) under different flow conditions. Fluorescent particles were diluted with DI water to reach ~ 0.01 - 0.02% volume fraction to decrease the particle-particle interaction. Tween 20 (Sigma-Aldrich, Singapore) was added, at a ratio of $\sim 0.1\%$ volume fraction to avoid particle clogging or particle aggregation.

3.3.3 Numerical Simulation

To investigate the flow field structure within different channel cross-section profiles, a 3D microchannel model was numerically developed using commercial software ANSYS Fluent (Version 15). The Navier-Stokes governing equations were solved for laminar flow using SIMPLE scheme. No-slip boundary condition was applied to wall. The velocity inlet and atmospheric pressure were set to the inlet and outlet, respectively. The physical properties of liquid water, i.e. density of 998.2 kgm^{-3} and dynamic viscosity of $0.001002 \text{ kgm}^{-1}\text{s}^{-1}$, were used for flow simulation.

3.3.4 Experimental Setup and measurement

Each suspension was pumped through the channel using a syringe pump (Chemyx, F200, USA) at different flow rates from 0.05 mL/min to 5 mL/min . The channel was mounted on an inverted epifluorescence microscope (Olympus IX71, Olympus Inc., USA) equipped with 16-bit CMOS camera (optiMOS, QImaging) shown in Figure 3-2. The images were taken at downstream close to the outlet ($\sim 40 \text{ mm}$). To capture the trace of fluorescent particles, exposure time was set to 1 s . To statistically find particle streak distribution, on average 100 fluorescent image sequences were stacked using IMAGEJ software to create a composite image along with an intensity line scan across the channel width. Counting particles using hemocytometer could not be carried out accurately for the dilute suspension in an order of 10^4 particles/mL ($10 \text{ }\mu\text{m}$, $15 \text{ }\mu\text{m}$ and $20 \text{ }\mu\text{m}$) and 10^3 particles/mL ($45 \text{ }\mu\text{m}$). Thus, a smaller sample volume of $1 \text{ }\mu\text{L}$ ($10 \text{ }\mu\text{m}$ to $20 \text{ }\mu\text{m}$ particle size) and $50 \text{ }\mu\text{L}$ ($45 \text{ }\mu\text{m}$ particle) was taken for enumerating particles. Having been collected from each outlet, samples were agitated by using vortex mixer and pipetting, then the

smaller sample volume was taken and dispersed into a petri dish. Subsequently, the fluorescent particles were counted manually on the microscope stage using fluorescent illumination.

To eliminate formation of air bubbles inside the channels, all channels required to be first primed by 70 percent ethanol for ~5 min before pumping particle suspension.

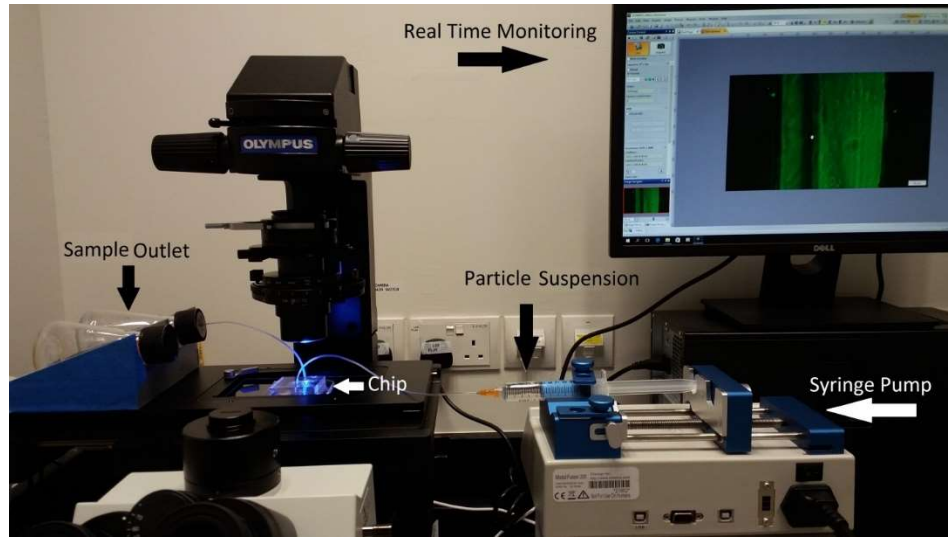


Figure 3-2 Photograph of the Experimental setup

3.4 Results and Discussion

3.4.1 Inertial focusing in the trapezoidal straight channel with AR of 2

To investigate the particle equilibrium position inside a trapezoidal cross-section, the effect of trapezoidal cross-section on axial velocity and vorticity profile was first studied as the main factors in the first step of particle migration undergoing shear-gradient lift force [39]. Figure 3-3 shows axial velocity contour and two main vorticities whose directions in the plane are perpendicular to the main flow. Shear-gradient inertial lift force originates from curl velocity [39] ($F_S = \omega \times U_S$ where U_S is the particle slip velocity and ω is the curl velocity). ω_x and ω_y are the representative of two major shear rates ($\omega_x \approx \frac{\delta U_{Axial}}{\delta y}$ and $\omega_y \approx -\frac{\delta U_{Axial}}{\delta x}$) which drive particles toward the top/bottom wall and the side walls at the primary stage of

lateral migration. The axial velocity contour displays deviation of the maximum velocity inside the trapezoidal cross-section toward the longer side wall. This deviation is one of the main factors which results in a new configuration of net inertial force and new equilibrium positions. ω_x contour in Figure 3-3a shows no significant change in the symmetrical condition when the rectangular cross-section is altered to the trapezoid, the ω_y contour, nonetheless, incurs a noticeable asymmetry along the channel width, particularly when AR increases from 2 to 4 (Figure 3-3a, ω_y), leading to the shear-gradient lift forces, pushing particles toward the longer side wall for the trapezoidal cross-section (Section 3.4.2), dash lines show zero-shear-rate boundary where direction of shear-gradient lift force alters. Similarly, the corresponding normalized axial velocity profiles show that elevated AR, from 2 to 4, intensifies the asymmetry of the velocity contour for the trapezoidal channels (Figure 3-3b). But, increasing the slope of the slanted wall, $\tan(\alpha)$, from 0.2 to 0.65, cannot change the asymmetry of axial velocity profile considerably; for the AR=4 (Figure 3-3c).

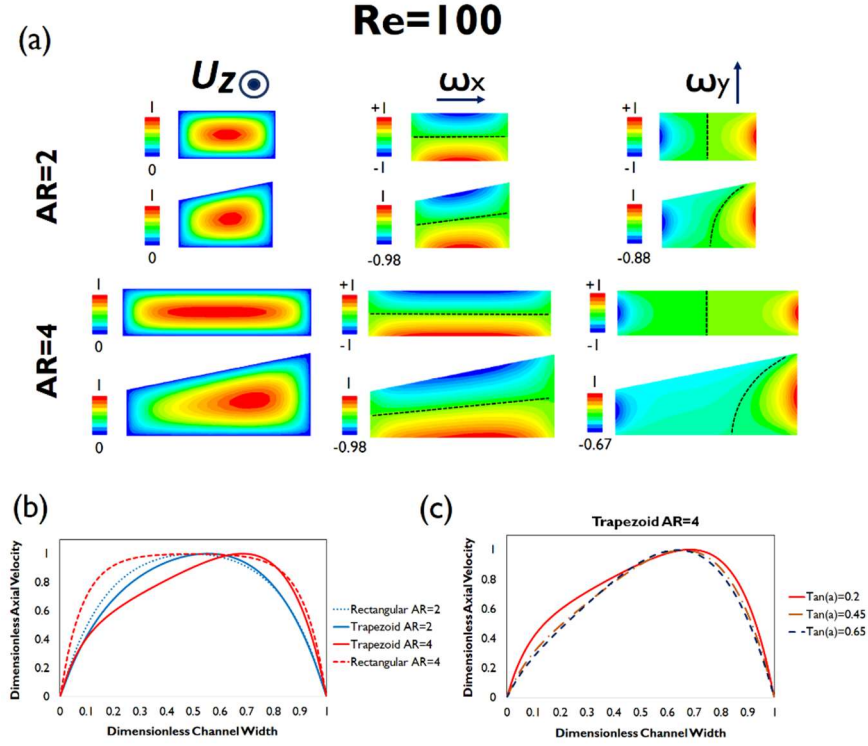


Figure 3-3 (a) Normalized axial velocity and vorticity profile at $Re=100$ for channels with rectangular and trapezoidal cross-sections with $\tan(\alpha)=0.2$. All contours are plotted under the same condition to be comparable qualitatively. Dash lines show zero-shear rate boundary where direction of shear-gradient lift force alternates. (b) The corresponding normalized axial velocity profile for the rectangular and the trapezoidal channel at the middle of channel height coincided with dash lines at ω_x contour. It shows that the deviation of maximum velocity toward the longer side wall is enhanced by increasing channel AR from 2 to 4. (c) Normalized axial velocity profiles of trapezoid straight microchannels for increased slopes of the slanted wall at the middle of channel height.

The equilibrium position of 10- μm and 15- μm fluorescent particles ($K\sim 0.2-0.3$) is shown for the trapezoidal channel ($H_{SW}50\text{ }\mu\text{m}$ - $H_{LW}70\text{ }\mu\text{m}$ - $W100\text{ }\mu\text{m}$) with $AR=2$ in Figure 3-4. As can be seen in Figure 3-4a, particles start gradually focusing and migrating toward the longer side wall when Re number increases ($20\leq Re<240$). Further increasing Re causes another lateral focusing next to the short side wall ($Re\geq 240$, $K\sim 0.3$), whereas the smaller particles with $K\sim 0.2$ are mostly dispersed due to the lower shear force. These minor lateral particle streams next to the side walls can be seen in Figure 3-4b at high $Re=320$ using intensity line scans. The main

lateral focusing peak of $K \sim 0.3$ particles is slightly deviated toward the longer side wall ($80 \leq Re \leq 160$); when exceeding a critical threshold, it causes particles to move back to the middle of the channel. This movement of major lateral focusing point in the trapezoidal channel is illustrated in Figure 3-4b by using fluorescence intensity line scan across the channel width. This low off-center movement of the major lateral focusing (~ 10 percent of the channel width at $Re \sim 80$) in the trapezoidal channel with $AR=2$ compared to the trapezoidal channel with $AR=4$, to be investigated next, has qualitatively similar trends to the numerical simulation, showing less dissymmetry in the velocity profile (or shear field).

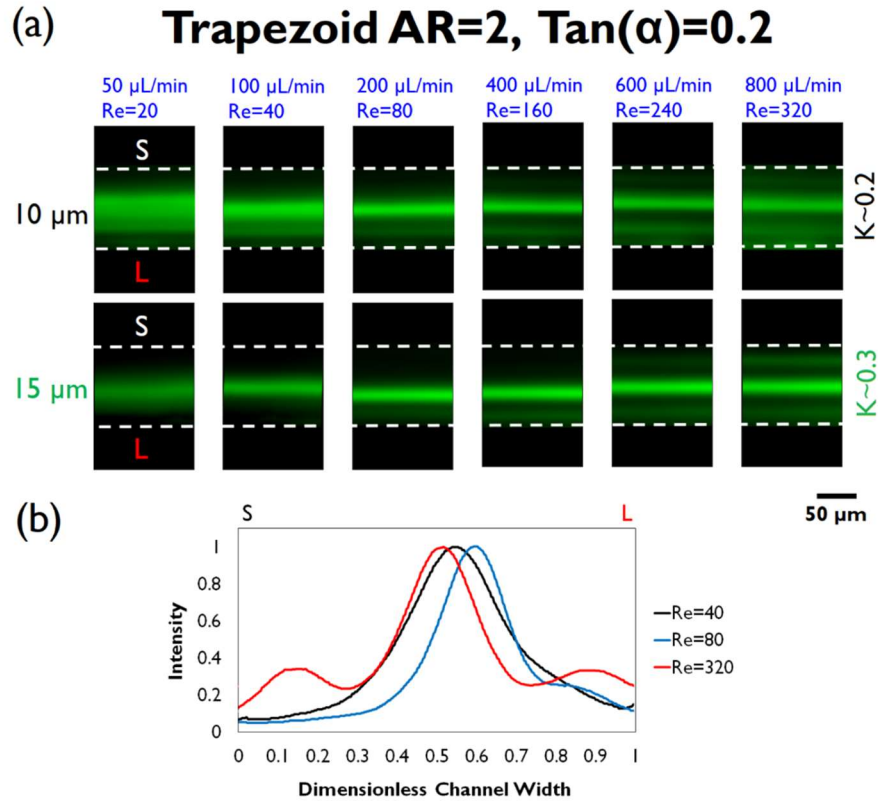


Figure 3-4 (a) Fluorescent images of 10- μm ($K \sim 0.2$) and 15- μm ($K \sim 0.3$) microparticles display lateral distribution of particles in the trapezoidal channel with $AR=2$ and $\tan(\alpha)=0.2$, (b) corresponding intensity line scan of 15- μm particles across the channel width (Letter L and S show the longer and the shorter side wall of the trapezoidal channel, respectively).

3.4.2 Inertial focusing in the trapezoidal straight channel with AR of 4

Particle focusing inside the rectangular channel ($H50\ \mu\text{m} \times W200\ \mu\text{m}$) with AR of 4 was first investigated as a benchmark ($\tan(\alpha)=0$). Figure 3-5a shows the lateral particle stream with $K \sim 0.4$ ($20\ \mu\text{m}$) equilibrated at the centers of the long face walls for $Re < 212$. As shown, further increasing Re number causes unstable equilibrium and consequently turns the lateral focusing at the middle into two lateral focusing streams symmetrically ($Re \geq 212$), which can also be seen in the corresponding intensity line scan profile (Figure 3-5b). Smaller particle clogging ratio of $K \sim 0.3$ ($15\ \mu\text{m}$) forms a comparatively broader particle band width (See Appendix A, Figure S3-2a) due to less wall-effect lift forces, $F_{CL} \sim a^3$ [39]. These behaviors are in agreement with previous works [32, 79].

Figure 3-5c shows that changing the rectangular channel ($\tan(\alpha)=0$) to the trapezoidal channel with $\tan(\alpha)=0.2$ ($H_{SW}50\ \mu\text{m}$ - $H_{LW}90\ \mu\text{m}$ - $W200\ \mu\text{m}$) slightly enhances the deviation of lateral focusing ($K \sim 0.4$, $20\ \mu\text{m}$) toward the longer side wall for low $Re \sim 49$, compared with the trapezoidal channel having AR=2 (Figure 3-4), but the main lateral focusing gradually gets back to the center of long face wall when Re increases to ~ 196 . Further increasing the channel Re number leads to the migration of main lateral focusing close to the shorter side wall while some other weaker lateral particle streams simultaneously start to emerge around the middle and the longer side wall ($Re \sim 733$). The movement of major lateral focusing toward the longer side wall and its backward shifting can be seen in Figure 3-5d. Also, the minor equilibrium is developed next to the longer side wall as Re exceeds ~ 196 illustrated by small peak adjacent to the wall at Figure 3-5d. Particles with lower clogging ratios, less than or equal to $K \sim 0.2$ ($10\ \mu\text{m}$) have no clear lateral focusing and are almost dispersed along the channel width (Figure S3-2b).

Interestingly, elevating the slope of slanted wall up to $\tan(\alpha) \sim 0.45$ ($H_{SW}50\ \mu\text{m}$ - $H_{LW}140\ \mu\text{m}$ - $W200\ \mu\text{m}$) further enhances the migration of particles with K greater than or equal to ~ 0.3 toward the longer side wall (Figure 3-5e) and boosts their

focusing quality (Figure 3-5f) for low- Re flows ($Re < 100$). However, minor peaks in Figure 3-5f at $Re > 100$ demonstrate that going beyond this threshold of channel Re number intensifies particle dispersion around the channel center and the longer side wall compared to the trapezoidal channel with lower slope ($\tan(\alpha) \sim 0.2$). Due to the comparatively large slant, it could handle a broader range of particle size without clogging. Figure 3-5e shows that the lateral focusing of particles with $K \sim 0.9$ ($45 \mu\text{m}$) sustains higher $Re \sim 264$ while neighboring the longer side wall. Remarkably, further increasing Re to ~ 654 demonstrates an almost complete shift of the lateral focusing toward the shorter side wall which can also be observed using the intensity line scan (Figure 3-5g). It should be noted that the intensity line scan does not approach zero near the longer wall, representing a few random particles passing by near the longer side wall.

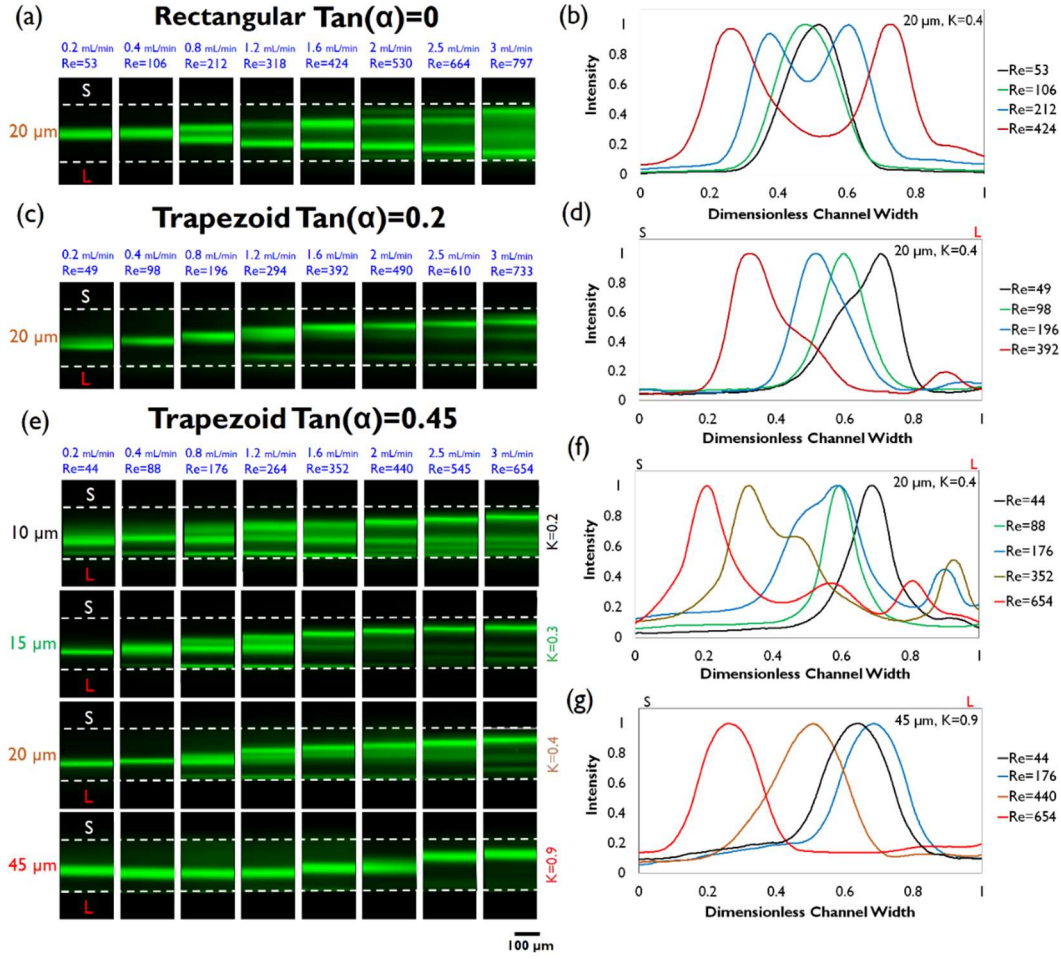


Figure 3-5 Fluorescent images and the corresponding intensity line scans of the rectangular channel (a-b) and the trapezoid with $\text{Tan}(\alpha)=0.2$ (c-d) for 20- μm particles ($K\sim 0.4$). (e) Fluorescent images of various particle sizes in the trapezoid channel with $\text{Tan}(\alpha)=0.45$ and the corresponding line scans for (f) 20- μm particles ($K\sim 0.4$) and (g) 45- μm particles ($K\sim 0.9$), displaying lateral distribution of particles in the trapezoidal channel. The channel aspect ratio of all channels is $\text{AR}=4$ (Letter L and S show the longer and the shorter side wall of the trapezoidal cross-sections, respectively)

To further clarify the location of particle focusing inside the trapezoidal channels, a side view channel was fabricated. Its fabrication process can be found elsewhere [102]. Figure 3-6a shows a side view of two particle streams for large-sized particles of $K\sim 0.9$ ($\text{Re}<264$), fluctuating near the center and the bottom wall (smaller particle clogging ratio $K\sim 0.4$ shown at Figure S3-3 displays clearly the side view of the lateral streams. For low-slant trapezoid $\text{Tan}(\alpha)\sim 0.2$ particles are mainly equilibrated

near the bottom wall and increasing slope of the slanted wall to $\tan(\alpha) \sim 0.45$ drives particle streams to both the center and the bottom wall). These two streams gradually merge close to the bottom wall when Re increases to ~ 654 . Figure 3-6b schematically displays the corresponding shifting of $K \sim 0.9$ particles from the longer side wall to the shorter side wall when Re goes up.

Moreover, the transient lateral particle focusing along the channel length and the corresponding line scan of $K \sim 0.9$ particles are shown in Figure 3-6c. Generally, particles are first pushed toward the middle and the longer side wall (See Figure S3-4, $Re \sim 440$ for smaller particle sizes). Afterwards, they start to be driven toward the shorter side wall. The developed minor peak next to the longer side wall that is shown in the intensity line scan at $L = 20$ mm gradually disappears, corresponding to particles migrating across streamlines toward the shorter side wall as travel to the channel downstream ($L = 40$ mm). The larger the particle size, the more particles will drift toward the shorter side wall. It should be noted that the particle Re number is considerably high ($R_p \sim 85$), on the grounds of high $Re \sim 654$ and large particle size ~ 45 μm . We would have interestingly reached the same R_p for the smaller particle size ~ 20 μm if the corresponding channel Re number could go up to ~ 3300 – close to the turbulent flow regime – which is impossible to experimentally explore due to a high pressure drop. Although the unperturbed velocity profile and shear force configuration, when flow is laminar, will remain similar, regardless of its magnitude, the alternation of lateral focusing implies the key role of particle-flow interaction. The particle-induced lateral flow may also play an important role at high- R_p flows [65]. A comprehensive numerical model which can simulate both particle and flow inertia may lead to an improved understanding of the mechanism of cross-laterally particle movement.

Finally, further increasing the slope of the slanted wall to $\tan(\alpha) \sim 0.65$ ($H_{SW} 50$ μm - $H_L 180$ μm - $W 200$ μm) caused a broader range of lateral focusing overall (Figure S3-5) due to the increased hydraulic diameter of channel cross-section.

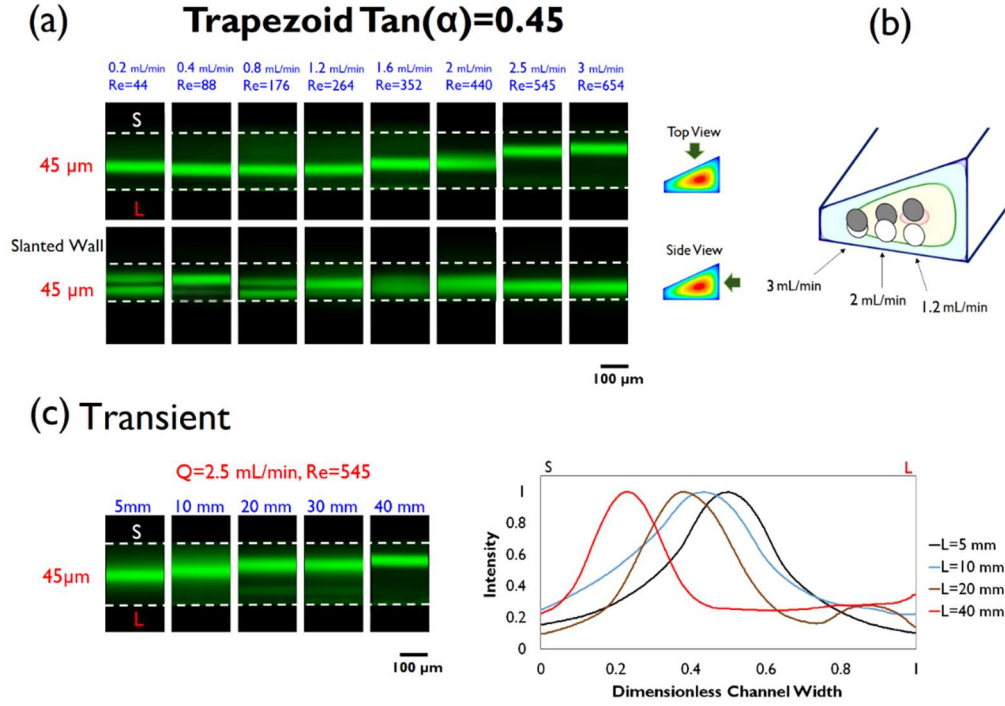


Figure 3-6 (a) Top and side view of the particle focusing ($K \sim 0.9$) in the trapezoid channel with $\tan(\alpha)=0.45$ and (b) the corresponding schematic particle movements by increasing Re . (c) Transient lateral particle focusing along the channel length and the corresponding line scans for $Re \sim 545$ and $K \sim 0.9$. It demonstrates a two-step lateral movement while it first moves toward the longer side wall and then starts shifting back toward the smaller side wall (Letter L and S show the longer and the shorter side wall of the trapezoidal cross-sections, respectively).

3.4.3 Particle filtration

Our experimental results proved the size-dependent cross-lateral migration of particles with $K > 0.3$ toward the longer side wall for $Re < 100$. Therefore, a trapezoidal channel with bifurcation was fabricated ($AR \sim 4$ and $\tan(\alpha) \sim 0.45$) for filtration purposes. Figure 3-7a depicts the filtration of a broad range of particle sizes through the longer wall (LW) outlet. As can be seen, particles with $K \sim 0.3$ (15 μm) were approximately equilibrated at the middle but the majority still went to the LW outlet. The larger particle sizes such as $K \sim 0.4-0.9$ (20 μm-45 μm) were laterally focused farther away from the middle of channel cross-section neighboring the LW,

and were subsequently collected from the LW outlet. Figure 3-7b displays the collected samples from the LW and the shorter wall (SW) outlet for $Re \sim 88$ (0.4 mL/min). To quantitatively measure the filtration performance of the trapezoidal straight channel, the efficiency is defined as follows:

$$Efficiency = \frac{Collected\ particles\ of\ interest}{Total\ number\ of\ particles} \quad (3.3)$$

Total number of particles is the sum of particles collected from both outlets. It should be noted that the ratio of collected volumes from LW to SW outlet is 2:1 due to the skewed maximum velocity toward the LW. The concentration of samples collected from both outlets can be seen in Figure 3-7c-e for 15 μ m, 20 μ m and 45 μ m, respectively. It demonstrates a large gap between concentration of particles collected from LW and SW outlet for particles with $K > 0.3$ ($a > 15$ μ m). The corresponding efficiency, Figure 3-7f, shows the high efficiency of $\sim 99\%$ and $\sim 87\%$ for particles with $K \sim 0.4-0.9$ and $K \sim 0.3$, respectively, when flow rate is 0.4 mL/min ($Re \sim 88$). The smaller particle size of 10 μ m ($K \sim 0.2$) cannot be focused and $\sim 33\%$ of it is diminished through the SW outlet. Thus, filtration resolution of the trapezoidal channel can reach down to ~ 5 μ m difference in size, i.e. the trapezoidal channel developed here can focus and filter ~ 15 - μ m particle or greater in contrast to smaller particle size of 10 μ m or less dispersed. Also, the 1.5-fold concentration of the trapezoidal straight channel can potentially increase to 2-fold by simply cascading two channels, while the whole unit has only one inlet and two outlets, relatively easier than that of the rectangular channels with trifurcation used for filtration [38, 99, 104]. In a recent work, a rectangular channel with $AR=2$ ($W > H$) with higher concentration of 3-fold to filter $K \sim 0.4$ particles/cells from the center outlet was used [99]; nonetheless, the particle clogging ratio could not exceed $K \sim 0.5$ due to the clogging of the channel. Moreover, the rectangular channels with $AR < 1$ ($H > W$) holding similar concentration of 1.5-fold can drive a broad range of particle sizes toward the side walls, $K > 0.07$ [37], disregarding being cross-laterally focused. Nonetheless, because of dominating shear gradient lift force along the channel width, it is likely suitable for extraction of all particle sizes from side outlets while

either a particle-free sample or a relatively small non-focused particles (such as bacteria in blood [104]) is collected from the central outlet.

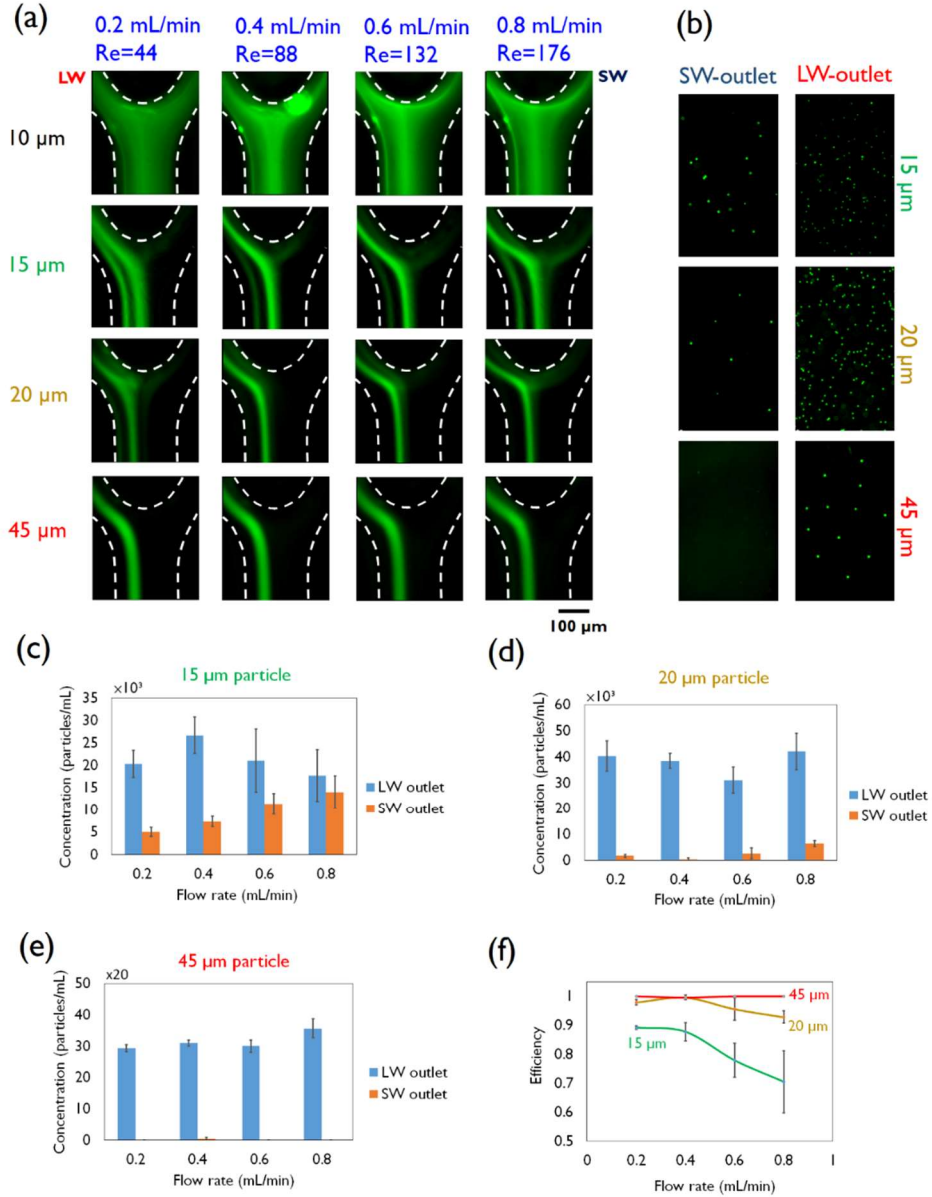


Figure 3-7 (a) Lateral focusing and filtration of particles through the longer wall outlet in the trapezoid straight channel ($\tan(\alpha) \sim 0.45$ and $AR \sim 4$), and (b) the corresponding samples collected from the shorter wall (SW) outlet and the longer wall (LW) outlet at $Re \sim 88$ (0.4 mL/min). (c-e) Concentration of various particle sizes (15 μm , 20 μm and 45 μm) collected from the SW outlet and the LW outlet. (f) Efficiency of particle filtration vs. flow rate.

Cross-lateral movement of major equilibrium position toward the shorter side wall in the trapezoidal channel can be utilized in filtration applications. A non-symmetrical bifurcation was used to further enhance the concentration of samples collected from the SW outlet, up to ~ 3 -fold, through increasing the volume of carrier fluid extracted from the LW outlet, though being slightly affected. Figure 3-8a depicts the transition of lateral particle focusing, $K \sim 0.9$ ($45 \mu\text{m}$), from the middle of the channel ($Re \sim 440$) toward the shorter side wall ($Re \sim 1100$), and correspondingly changing the filtration of particles through the LW outlet to the SW outlet at $Re \sim 440$ (2 mL/min) and $Re \sim 1100$ (5 mL/min), respectively. The transition condition occurred at $Re \sim 880$ (4 mL/min), while the lateral focusing fluctuated around the middle of the channel. Further increasing Re led to migration of particles toward the shorter side wall till Re reached ~ 1100 (5 mL/min); exceeding $Re \sim 1100$ brought about a formation of another lateral focusing near the longer side wall ($Re \sim 1320$). The soaring concentration of collected samples from the SW outlet (~ 2.5 -fold) at $Re \sim 1100$ (5 mL/min) can be seen in Figure 3-8b and the corresponding efficiency in Figure 3-8c, as high as $\sim 82\%$. It should be noted that the threshold of critical Re number from which particles began to migrate to the shorter side wall was increased for the trapezoidal channel having bifurcation, mainly due to the slight alteration of cross-section dimensions, which arose from the $\pm 10 \mu\text{m}$ resolution of micro milling technique, and the channel deformation due to the high working pressure. The performance of the device, i.e., efficiency and concentration factor, can be further enhanced by fabricating more precise channels and manipulating the bifurcation design. Also, the filtration resolution can be further enhanced by using a symmetrical trapezoidal cross-section thereby boosting inertial focusing off the channel center even at higher Re number expected.

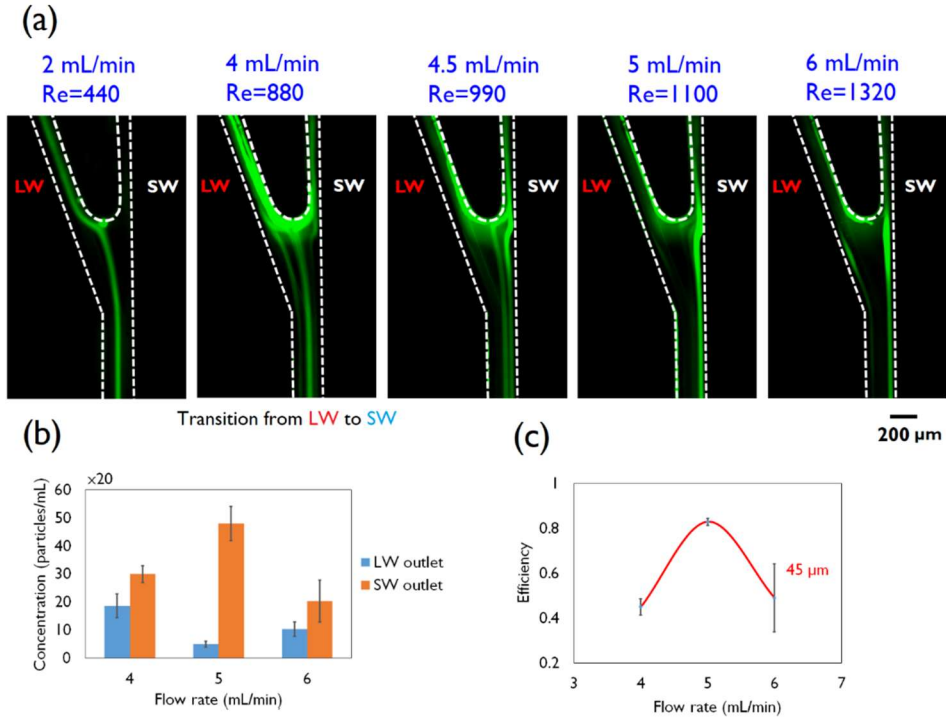


Figure 3-8 (a) Transition of lateral focusing from the middle of channel cross-section toward the shorter side wall as the Re number increases. (b) Concentration of samples collected from the SW and the LW outlet and (c) the corresponding efficiency (Letter **LW** and **SW** show the longer and the shorter wall outlet of the trapezoidal cross-section ($\tan(\alpha) \sim 0.45$ and $AR \sim 4$), respectively).

3.5 Summary

The inertial particle focusing dynamics in trapezoidal straight microchannels is investigated for a broad range of particle Reynolds number ($0.4 < Re < 90$). An off-center lateral focusing position from the middle of channel cross-section, up to ~20 percent of the channel width, is found. In general, a shift from longer sidewall towards the shorter side wall in lateral focusing is observed when the channel Reynolds number increases ($Re > 50$). Finally, a trapezoidal straight channel with a bifurcation is applied to remove a broad range of particle sizes ($0.3 < K < 1$) exiting through the longer wall outlet with an efficiency of ~99% ($Re < 100$).

Chapter 4 Inertial-Based Filtration Method for Removal of Microcarriers from Mesenchymal Stem Cell Suspensions

In Chapter 3 inertial focusing was investigated in straight trapezoidal channels without the influence of secondary flow. Though throughput of straight channel structure is relatively easy to scale out through parallelization, this structure is inherently limited to low particle volume fractions ($V_f \ll 0.5\%$). Therefore, the Dean-coupled inertial focusing is employed to achieve higher throughput that can tackle high microcarrier volume fractions used for efficient expansion of adherent cell types such as human mesenchymal stem cells (hMSCs). This chapter demonstrates a novel alternative approach which utilizes inertial focusing to filter microcarriers (MCs) from the final cell suspension.

4.1 Introduction

Off-the-shelf (allogeneic) therapies transplanting human mesenchymal stem cells (hMSCs), derived mainly from bone-marrow, adipose tissue, and umbilical cord blood tissue [157], are widely adopted due to hMSCs' regenerative, immunosuppressive, and multipotent features [156, 182]. The clinical demand for hMSCs is rising significantly, with more than 400 registered clinical trials [155, 183], and the required doses per patient can reach up to 10^9 cells [157, 158, 184]. For instance, the number of cells is estimated to be $\sim 10^{12}$ cells per lot for diseases that need high doses of $\sim 10^8$ - 10^9 cells to be delivered. Using multilayer tissue culture flasks cannot meet the demand efficiently for cell therapy products beyond the scale of 100 billion cells [157, 185, 186]. Thus, embracing alternative methods for in vitro cell expansion is necessary. Bioreactors, for scaling up the cultures in 3D rather than scaling out the cell culture flask in 2D, are used as an efficient and cost-effective approach to commercialization [160, 163, 187]. Among different

adherent cell bioreactors, employing suspension scaffolds so-called microcarriers (MCs), $\sim 100\text{-}300\text{ }\mu\text{m}$ in diameter, within a stirred tank has been widely recognized [161, 184]; recently it was demonstrated within a 50-L bioreactor that a 43-fold expansion of hMSCs could be reached in 11 days [188]. Using microcarriers, however, necessitates clarification of cell suspension bulk and downstream removal of MCs.

Following cell expansion and detachment from microcarriers, existing systems for separation of MCs and cells are tangential flow filtrations (TFF), counter-flow centrifugation elutriations (CCE), and dead-end sieving [185]. However, clogging (cake formation) and high shear stress for sieve-based systems [189, 190], as well as high operative costs due to bulkiness and rotating parts for CEE systems such as KSep platform (Sartorius), pose disadvantages. Herein, the advancement of an alternative method using inertial focusing is demonstrated – shown recently to be scalable for filtration of large-scale lot size in the order of liter per min [2, 142, 191, 192].

The inertial focusing phenomenon is only reliant on hydrodynamic forces, therefore, it gives rise to the relatively ease of parallelization to scale out the throughput. A high-throughput cell retention device was recently introduced; it utilized spiral channels for perfusion bioreactors while the projected device footprint for overall $\sim 1000\text{ L}$ perfusion rate during one day was approximated to be $100\text{ mm} \times 80\text{ mm} \times 300\text{ mm}$ [2, 142], noticeably smaller when compared to other CEE systems. Furthermore, the inertial-based filtration is a continuous clog-free (or membraneless) system thereby sustaining reliable steady performance without declining during long-term operation, and obviating the need for filter replacement. In this chapter, first inertial focusing of microcarriers in scaled-up spiral channels (channel size $\geq 0.5\text{ mm}$) is systematically investigated. Afterward, removal of microcarriers from hMSCs suspension was accomplished by inertial focusing with $\sim 99\%$ purity while cell harvest yield reached $\sim 94\%$.

4.2 Design Principle

Inertial focusing for neutrally buoyant particles flowing inside a channel occurs when the particle radius is comparable to the channel hydraulic diameter, $a/D_H > 0.07$ [25], and the channel Re number is of order about ~ 100 [37, 193], thereby triggering the shear-gradient lift force (F_S). Adding any curvature to the straight channel such as a spiral leads to the development of two counter-rotating vortices whose structures rely upon the Re number and channel cross-sectional shape [33, 49, 138, 194]. The interplay between the induced shear-gradient lift forces and the secondary drag forces (F_D) results in distinctive lateral focusing points inside the spiral channels, which is strongly dependent on particle size [84, 126]. When the particle approaches the channel walls, wall-induced lift force (F_W) and cross-lateral wall-effect lift force (F_{CL}) emerge [195]. Figure 4-1b illustrates schematically the balancing forces that develop equilibrium near the inner wall. Since the difference in size between MCs ($\sim 100\text{-}300\ \mu\text{m}$) and hMSCs ($\sim 10\text{-}30\ \mu\text{m}$) is significant (Figure 4-1a), it is impossible to focus both particle sizes simultaneously in a channel. A negative selection approach, therefore, is chosen to focus and filter out the MCs. However, the cells are not large enough to undergo shear-gradient lift forces ($a/D_H \sim 0.02$); as a result, they are mainly influenced by the secondary flow and disperse inside the spiral channel (Figure 4-1b). Consequently, some cells are elutriated through the inner wall (IW) outlet. Thus, to enhance cell harvest yield, recirculating IW outlet collection containing both MCs and cells is mandatory. However, because cells are the final product, their viability and integrity are prone to decline when pumped through the channel, as they are iteratively exposed to shear stress. The number of passes to retrieve cells from MCs (IW) outlet, therefore, should be limited. To achieve cell harvest greater than 90% with two passes, it requires a higher amount of cell harvest via outer wall (OW) outlet than 50% for one pass.

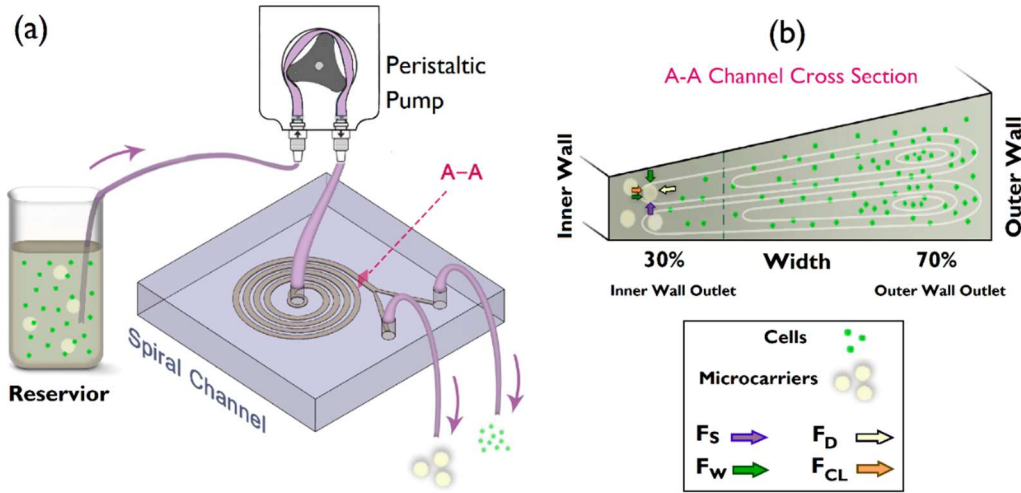


Figure 4-1 Schematic model showing filtration of microcarriers from cell suspensions. (a) The microcarrier-cell suspension is driven to the channel using a peristaltic pump. (b) Channel cross-section A-A before bifurcation. Microcarriers equilibrate near the inner wall (IW) by the balancing forces shown schematically whereas cells are mainly circulated by secondary flow and harvested through the outer wall (OW) outlet.

Altering the cross-sectional shape of spiral channels from rectangular to trapezoidal shifts the maximum axial velocity and vortex cores toward the longer side wall (Figure 4-2a), thereby elevating the ratio of outer outlet to inner outlet collection from 1:1 up to 2.5:1, depending on the location of bifurcation and channel aspect ratio; it implies the increased harvesting of carrier fluid from outer outlet from 50% up to ~70%. Cell harvesting yield is proportional to elutriated carrier fluid from outer wall outlet assuming uniformly dispersed cells inside the channel although the vortex cores near the outer wall potentially trap and maintain higher cell concentrations locally. Accordingly, trapezoidal spiral channels with different slanted wall slopes are investigated as well as the rectangular spiral for which the slope of the slanted wall is zero ($\tan(\alpha) = (H_{\text{outer wall}} - H_{\text{inner wall}})/W = 0$).

To scrutinize secondary flow structure, rectangular and trapezoidal spirals ($\tan(\alpha) = 0.0375$) with large channel aspect ratios of 8 ($AR = W/H$) were numerically assessed using ANSYS Fluent to solve the Navier-Stokes equations for incompressible flow (The density, 998.2 kg m^{-3} , and dynamic viscosity, 0.001002

$\text{kgm}^{-1}\text{s}^{-1}$, were set for liquid water at room temperature $20\text{ }^{\circ}\text{C}$). The results show that the trapezoidal spiral not only enhances a positive secondary flow, which contributes to driving particles (or MCs) to the inner wall, but also alters the distribution of secondary flow. As such, the maximum secondary flow's regions are laid at the outer half of channel cross-section (Figure 4-2b). Compared to the corresponding rectangular spiral, the positive secondary flow tapers at a slower rate across the trapezoidal spiral channel, due to the rapid reduction of Dean number ($De = Re\sqrt{D_H/2R}$ where Re is channel Reynolds number, D_H and R are channel hydraulic diameter and radius of curvature respectively) by 60% across the spiral channels. In other words, the difference in positive secondary flow between two spirals increases particularly at the downstream loops (3rd to 4th loop), as shown in Figure 4-2c. This illustrates the enhanced secondary flow drag ($F_D \sim U_D$ where U_D is secondary velocity) sweeping particles (microcarriers) toward the inner wall to establish focusing only in an ultra-low-slope trapezoidal spiral (Section 4.4.1). Because inertial focusing of MCs near the inner wall cannot be interpreted solely as a result of positive secondary flow without considering the shear force; we investigated MC focusing dynamics experimentally due to the lack of a shear-gradient force model exclusively for spiral channels.

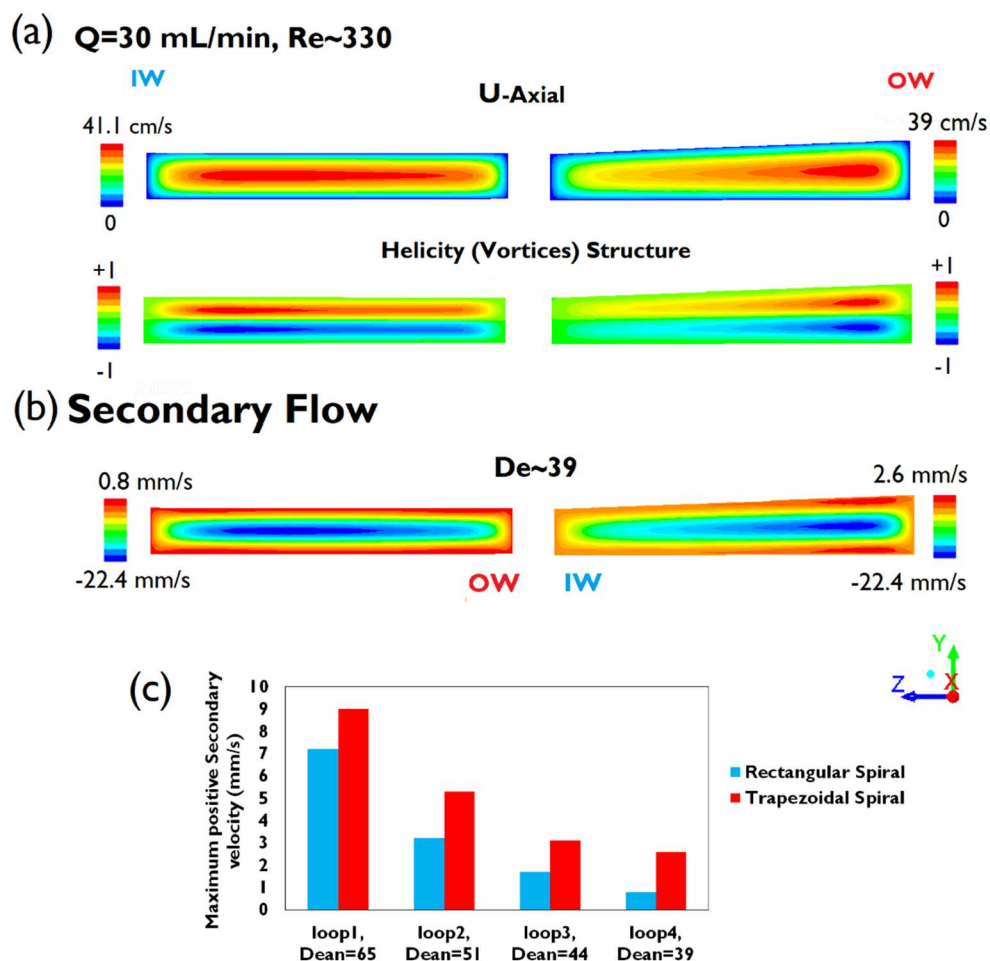


Figure 4-2 (a) Axial velocity profile (+X direction) and vortices structure (Helicity contour) in the rectangular and trapezoidal channels with $\tan(\alpha)=0.0375$. (b) Secondary flow distribution and (c) its maximum positive secondary flow velocities, whose direction from outer wall to inner wall, reduce notably at different loops of the scaled-up rectangular and trapezoidal spiral channel at flow rate of 30 mL/min, but the trapezoidal spiral shows relatively higher positive secondary velocity (+Z direction) and as a result larger drag force to drive particles to the inner wall.

4.3 Material and methods

4.3.1 Channel fabrication

Aluminum master molds were fabricated via micro-milling technique (Whits Technologies, Singapore). After casting the mixed polydimethylsiloxane polymer

(PDMS, Sylgard 184 Silicone Elastomer Kit, Dow Corning) and curing agent (10:1 ratio) into the mold, it was cured for 30 min in an oven with 80 °C. To boost bonding, we used semi-cured PDMS bonding rather than the conventional oxygen plasma treatment [196, 197]. Following peeling off the semi-cured PDMS spiral channel and punching the inlet and outlets, the PDMS spiral chip was bonded irreversibly with another semi-cured slab of PDMS (~3 mm thickness cast in a petri dish). Subsequently, the assembled channel was further cured for 3 hours in the oven until complete bonding was achieved.

4.3.2 Cell culture

Bone-marrow-derived hMSCs (Lonza, Singapore) were cultured in T175 tissue culture flasks pre-coated with 0.1% (1g/L) type A gelatin (Sigma-Aldrich, Singapore) in a humidified incubator with 37 °C and 5% CO₂ in air. The BM-hMSCs were passaged in high-glucose Dulbecco's modified Eagle's medium (DMEM, Life Technologies Holdings Pte Ltd, Singapore) supplemented with 10% fetal bovine serum (FBS, Life Technologies Holdings Pte Ltd, Singapore), 1% Penicillin-Streptomycin (10,000 U/mL, Life Technologies Holdings Pte Ltd) and 10 ng/mL bFGF (PeproTech, Singapore). At ~80% confluency, cells were washed with Ca²⁺- and Mg²⁺-free DPBS, then dissociated using 0.25% trypsin and 0.53 mM EDTA, and finally incubated for 3 minutes. The detached cells were subsequently resuspended in the culture medium (~5-fold dilution) to neutralize the trypsin, then centrifuged with 300 g for 10 min. The harvested cell pellet was then resuspended in the culture medium based on desired cell concentration. The hMSCs were seeded at density of 5000 cells/cm².

4.3.3 Microcarrier and sample preparation

Dry Cytodex 3 microcarriers (GE Healthcare) were hydrated using 1X Ca²⁺- and Mg²⁺-free phosphate buffered saline (PBS) for 3 hours. Afterward, they were washed twice using PBS prior to autoclaving. The stock solution was prepared at a concentration of 10 g/L. According to the manufacturer's instruction, the average

number of MCs is approximately 3×10^6 MCs/g, which corresponds to 8.42% v/v solid volume fraction (the average diameter is $\sim 175 \mu\text{m}$). The stock MC suspension was prepared with various dilution factors to acquire lower volume fractions which are 0.2%, 0.4%, 0.8% and 1.68%.

4.3.4 Device characterization

First, to evaluate focusing dynamics of MCs in spiral channels without cells, the desired MC suspension was dyed with trypan blue (0.1% v/v) to enhance contrast for bright field microscopy. The spiral channel was mounted on an inverted epifluorescence microscope (Olympus IX71, Olympus Inc., USA) which is equipped with a 16-bit CMOS camera (optiMOS, QImaging), and the MC solution was introduced to the channel inlet by means of a peristaltic pump (LeadFluid, BT300S). The MC solution was agitated to prevent deposition. The exposure time was set as low as 100 ms. Image sequences (an average of 200) were stacked to develop a composite image using ImageJ software to obtain the entire footprint of the MC band width.

The best spiral design achieved with regards to MC focusing was used for removal of MCs from cell suspensions. To reduce contaminations, the filtration process was carried out inside a biosafety cabinet (BSC). The channel and tubing were sterilized running 70% ethanol for ~ 15 min. Next, the channel was washed with Ca/Mg-free DPBS for ~ 10 min to wipe residual ethanol and to keep the channel and tubing filled. Finally, the inlet tubing was inserted into the MC-cell solution previously prepared, and the filtration began by pumping the solution until the total volume reached 45 mL (Figure S4-1 shows the experiment setup). Lastly, to enhance cell harvest yield, collected samples from the inner wall (MCs) outlet were once more passed through the channel.

4.3.5 Cell characterization

4.3.5.1 Cell viability and proliferation

Following cultivation of sorted cells at day 1 in a 6-well tissue culture plate at a concentration of 5×10^4 cells/well, the viability and proliferation of attached cells were examined by PrestoBlue assay. A mixture of 10X PrestoBlue reagent (Invitrogen, Life Technologies Corporation) and culture medium with ratio of 1:10 was prepared. Having been washed in PBS with $\text{Ca}^{+2}/\text{Mg}^{+2}$, each well was filled up with 2 mL of the 1X PrestoBlue reagent stock prepared. Next, the 6-well plate was covered in aluminum foil (to protect from light) and incubated for 40-60 min. The supernatant was then aliquoted (at least 4 samples from each well) to a 96-well plate (100 μL) so to read fluorescence in a plate reader (Tecan Infinite M1000). Finally, the PrestoBlue reagent was washed off in PBS without $\text{Ca}^{+2}/\text{Mg}^{+2}$, and the 6-well plate was topped up with fresh culture medium and placed in the incubator.

4.3.5.2 Trilineage differentiation

Once the sorted cells had grown to 80% confluency, they were harvested using the methods described in 4.3.2. Cell culture.

Adipogenic differentiation

Prior to cell seeding for adipogenic differentiation, a 24-well plate (Nunclon Delta Surface, Thermo Scientific) was pre-coated with fibronectin (Sigma-Aldrich). 200 μL of Ca^{2+} - and Mg^{2+} -free DPBS, and 2 μL of fibronectin were added to each well. The plate was incubated at 37°C for 1 hour, after which the coating solution was aspirated. 6×10^4 cells in 500 μL of culture medium (described in 4.3.2. Cell culture) were seeded into each well. After 24-hour incubation, all the culture medium was aspirated, and the wells rinsed with Ca^{2+} - and Mg^{2+} -free DPBS twice. 500 μL of adipogenic differentiation media (MSCgo™ Adipogenic, Biological Industries) was added to the wells. The plate was incubated at 37°C for 28 days, with 100% medium change done every 2 or 3 days.

Oil Red O staining for adipogenic differentiation

At the end of 28 days of culture, the adipogenic differentiation medium was removed from the 24-well plate and the wells were rinsed with Ca^{2+} - and Mg^{2+} -free DPBS once and removed. 500 μL of 4% formaldehyde (Paraformaldehyde Solution, 4% in PBS, Affymetrix/USB) was added to each well; the plate was then incubated at room temperature for 1 hour. 0.175 g of Oil Red O (Sigma-Aldrich) was dissolved in 50 mL of 2-propanol (Sigma-Aldrich) and filtered through a 0.2 μm filter (Minisart®, Sartorius Stedim Biotech). 18 mL of the dissolved Oil Red O was mixed with 12 mL of deionized water and was left at room temperature for 20 minutes. The staining solution was filtered through a 0.2 μm filter. 4% formaldehyde was removed from the fixed samples and samples were rinsed with Ca^{2+} - and Mg^{2+} -free DPBS. 1mL of Oil Red O staining solution was added to each well. The plate was incubated at room temperature for 30 minutes, after which the stain was removed, and the wells were rinsed with deionized water until excess Oil Red O stain was washed off. The plate was imaged at 4X, 10X, and 20X magnification (EVOS FLc, Life Technologies).

Chondrogenic differentiation

1×10^5 cells in 100 μL of culture medium (described in 3.2. Cell Culture) were seeded into each well of a 96-well ultra-low attachment, round-bottom plate (Ultra Low Cluster, 96 Well, With Lid, Round Bottom, Ultra Low Attachment Polystyrene, Costar) and incubated for 24 hours. Culture medium was subsequently aspirated and rinsed with Ca^{2+} - and Mg^{2+} -free DPBS twice. 200 μL of chondrogenic differentiation media (MSCgo™ Chondrogenic XF, Biological Industries) was added to the wells. The plate was incubated at 37°C for 28 days, with 100% media change every 2 or 3 days.

Alcian Blue staining for chondrogenic differentiation

After culturing for 28 days, chondrogenic differentiation medium was removed from the 96-well plate, and all wells were rinsed with Ca^{2+} - and Mg^{2+} -free DPBS once. 200 μL of 4% formaldehyde was added to each well, and the plate was incubated at room temperature for 1 hour. 0.2 g of Alcian Blue 8GX (Sigma-

Aldrich) was dissolved in 20 mL of 0.1 N hydrochloric acid (Sigma-Aldrich) and filtered through a 0.2 μm filter. 4% formaldehyde was removed from the fixed samples and samples were twice rinsed with deionized water. 200 μL Alcian Blue staining solution was added to each well. The plate was incubated at room temperature overnight and protected from light. The Alcian Blue stain was removed, and the wells were rinsed with 0.1 N hydrochloric acid until excess Alcian Blue stain was washed off. 200 μL deionized water was added to each well. The plate was imaged at 4X magnification.

Osteogenic differentiation

Before cell seeding for osteogenic differentiation, a 24-well plate was coated with fibronectin, as described in adipogenic differentiation. 6×10^4 cells in 500 μL of culture medium were seeded into each well and incubated for 24 hours. After a 24-hour incubation period, all culture medium was aspirated and rinsed with Ca^{2+} - and Mg^{2+} -free DPBS twice. 500 μL osteogenic differentiation medium (MSCgo™ Osteogenic XF, Biological Industries) was added to the wells. The plate was incubated at 37°C for 28 days, with 100% medium change every 2 or 3 days.

Alizarin Red S staining for osteogenic differentiation

After 28 days of culture, osteogenic differentiation medium was removed from the 24-well plate, and all wells were rinsed with Ca^{2+} - and Mg^{2+} -free DPBS. 500 μL cold 70% ethanol was added to each well, and the plate was incubated at room temperature for 1 hour. 1 g Alizarin Red S (Sigma-Aldrich) was dissolved in 50 mL of deionized water. The pH was adjusted to 4.1 – 4.3 using 0.1 N hydrochloric acid or 0.5 M sodium hydroxide (prepared from sodium hydroxide pellets from 1st BASE) and filtered through a 0.2 μm filter. Ethanol was aspirated from samples and each was rinsed with deionized water thrice. 500 μL Alizarin Red S stain was added to each well, and the plate was incubated at room temperature for 30 minutes. The stain was removed, and the wells were rinsed with deionized water until excess stain was washed off. 500 μL deionized water was added to each well. The plate was imaged at 4X and 10X magnifications.

4.4 Results and discussion

4.4.1 Microcarrier focusing dynamics in the scaled-up spirals

A series of scaled-up trapezoidal spiral channels were fabricated to investigate the effects of channel height and slanted wall slope – $\tan(\alpha)$. The cross-sectional shape of fabricated channels can be seen in Figure S4-2. The initial radius of curvature measured from the inner wall was 5 mm, and the pitch of the Archimedean spiral was 7 mm (3-mm interval between successive spiral loops). The channel width was fixed at 4 mm while the channel heights varied from 0.5 mm to 1 mm. The channel Reynolds number was defined based on maximum shear rate: $Re = \rho_f U_{max} D_H / \mu$ (where ρ_f is the density of fluid, $U_{max} \approx 3/2 U_{avg}$ [25, 84], D_H is the hydraulic diameter of channel and μ is the dynamic viscosity of fluid).

Figures 4-3a-d are the composite bright field images illustrating the complete footprint of MC focusing before bifurcation. First, a scaled-up trapezoidal spiral with a low slant ($\tan(\alpha)=0.075$) that is similar to trapezoidal spirals reported at the micron scale [48, 49] was investigated. Though the MC volume fraction is as low as $\sim 0.2\%$, the relatively large band of MC streaks equilibrated at the inner half of the cross-section (Figure 4-3a) demonstrates malfunctioning of the channel (0.5 mm inner wall height and 0.8 mm enlarged outer wall).

It should be noted that the channel is fit for low-volume-fraction suspensions while particles are collected from the inner wall outlet (See Figure S4-3 displaying the filtration of MCs with low $V_f \approx 0.1\%$). Similar to trapezoidal spiral channels at micron scale when a small population of larger particles/cells is separated from an abundant population of smaller particles/cells—e.g. separation of CTCs from WBCs or WBCs against RBCs population [44, 48]—the channel performs robustly. Conversely, the MC volume fraction is not limited to $\sim 0.1\%$ or less here. In addition, unlike the present configuration where the Dean number ($De = Re\sqrt{D_H/2R}$) declines rapidly by $\sim 60\%$ across the spiral channel, the increasing-Dean mode of

the trapezoidal spiral (switching the direction of MC solution pumped) was examined. Though it enhances focusing but it still cannot handle the high MC volume fraction of greater than 0.4% (Figure S4-4).

Next, effects of particle clogging ratio were investigated by increasing channel height. Importantly, though there is no theoretical limitation on channel height when the ratio of particle size to channel height ($K=a/H$) ranges typically from 0.1 to 0.4, a 0.2 mm increase in average channel height led to MCs equilibrating partially at significantly low Re number ~ 56 (Figure 4-3b, 5.5 mL/min). The corresponding average K factor decreased from 0.26 to 0.20. The physical ramification of reduced volumetric flow rate was a lower velocity of particles traveling through the channel (flow velocity $U_{avg} \approx 2.6$ cm/s), which heightened the potential of clogging the channel, particularly when the microcarrier volume fraction was high ($V_f > 0.4\%$).

Finally, variations in the slope of the slanted spiral wall were surveyed. Remarkably, Figure 4-3c demonstrates that a trapezoidal spiral with an ultra-low-slope slanted wall ($\tan(\alpha)=0.0375$, channel height varied from 0.5 mm to 0.650 mm at outer wall) could only establish the MC focusing (particle band width $< 4a$) close to the inner wall at a noticeably high flow rate of ~ 30 mL/min ($Re \sim 326.5$). The MC dispersion began at Re greater than ~ 468 , however, the swift switch in equilibrium position from the inner wall to the outer wall was not observed even at high $Re \sim 555$ compared to conventional trapezoidal spirals in micron scale [48, 49]. The ultra-low slanted wall and relatively large particle clogging ratio could potentially delay the transition of focusing from the inner wall to the outer wall. The corresponding rectangular spiral channel (Figure 4-3d, $\tan(\alpha)=0$) verified the constructive impact of the ultra-low-slope slanted wall on MC focusing, while even partial focusing was not formed regardless of channel Re number. It should be noted that the elevated channel height in Figure 4-3c is relatively small in the order of MC size or even lower (150 μm) particularly at the outer half of channel cross-section in the ultra-low-slope trapezoidal spiral. As previously demonstrated numerically (Section 4-2), in addition to the enhanced secondary flow's drag force overall, the ultra-low-slope

trapezoidal spiral may cause the MCs exposed further to the positive secondary flow close to the top and the bottom wall than the typical trapezoidal spirals with a larger slope ($\tan(\alpha) \sim 0.1$), i.e. it could alter the equilibrium planes next to the top and the bottom wall relative to the zero-secondary-flow boundary, in which the direction of secondary flow switches, or vice versa.

In conclusion, Figure 4-3e demonstrates the performance of the ultra-low-slope trapezoidal spiral in MC filtration efficiency with approximately ~99% (Table S4-1 Appendix B, efficiency $E = \frac{C_s - C_o}{C_s} \times 100$ where C_s is the MC concentration in the reservoir and C_o is the MC concentration in the outer wall outlet). The fraction of flow which exited through the outer wall outlet (MC-free outlet) was maintained at ~70% of the carrier fluid that directly impacts on cell harvesting yield. The strong MC focusing developed adjacent to the inner wall, enabled higher MC volume fractions of up to ~1.68% to be removed without compromising filtration efficiency. It is of great importance to incorporate high-volume-fraction MC solutions as industrial scales of MC-based bioreactors (~100 L) have been reported that using MCs with volume fractions in the order of ~1% or more practically [164, 190, 198-203]. Thus, the proposed channel streamlines the filtration procedure and eliminates any large dilution factors.

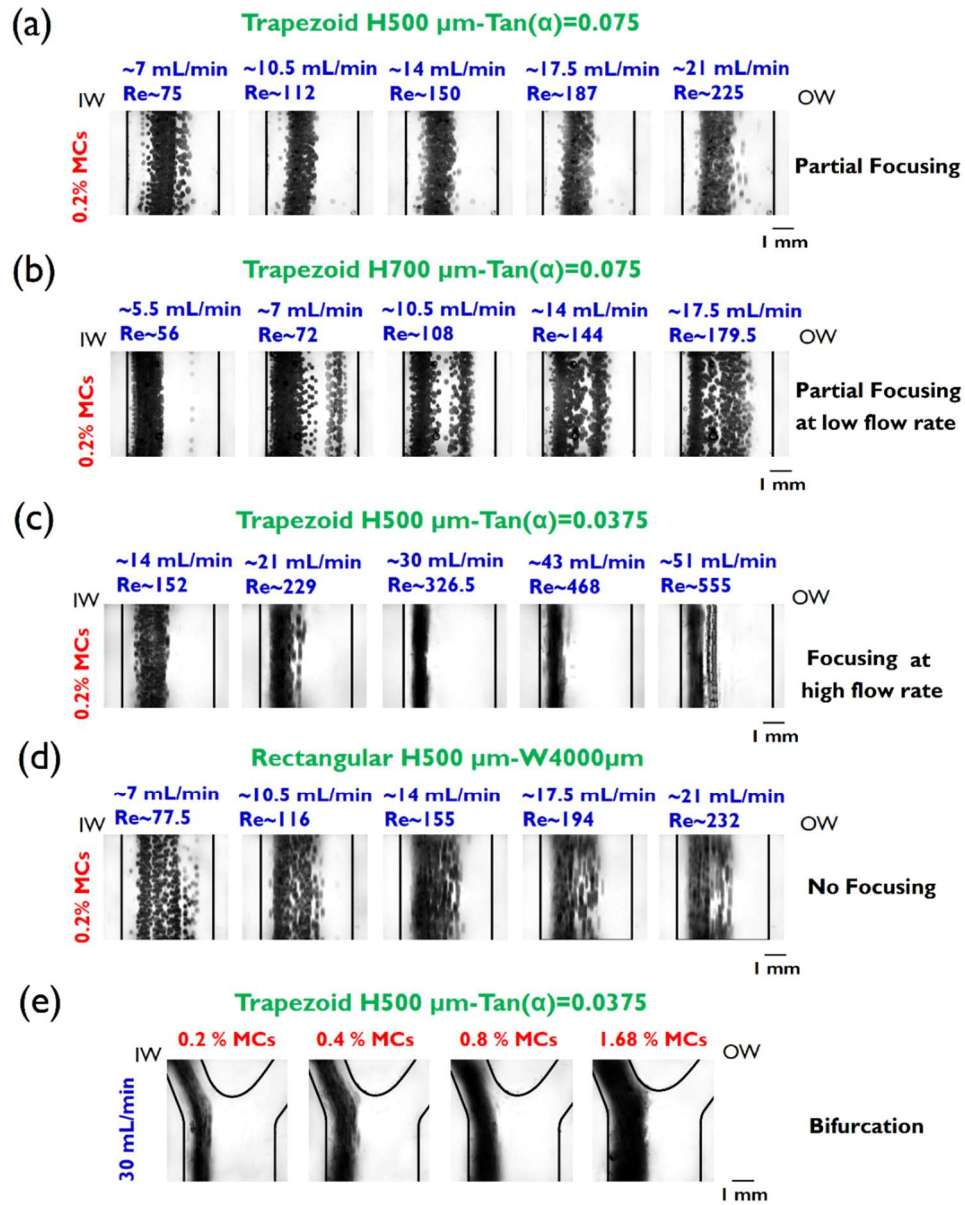


Figure 4-3 Microcarrier focusing dynamics at the last loop of spiral channel in (a) the trapezoid with $H=500 \mu\text{m}$ Tan(α)=0.075, (b) $H=700 \mu\text{m}$ and Tan(α)=0.075, (c) $H=500 \mu\text{m}$ Tan(α)=0.0375 and (d) $H=500 \mu\text{m}$, rectangular cross-section (Tan(α)=0.0). (e) Filtration of microcarriers from the inner wall outlet at 30 mL/min using trapezoidal spiral $H=500 \mu\text{m}$ Tan(α)=0.0375. It demonstrates complete removal of microcarriers for high microcarrier volume fraction of 1.68%, while collecting 70% of carrier fluid from the outer wall outlet. Focusing and partial focusing refer to particle band width (BW) $< \sim 4a$ and $\sim 4a < \text{BW} < \sim 10a$, respectively.

4.4.2 Removal of microcarriers from mesenchymal stem cell suspension

Since hMSCs are prone to morphology damage and cell death due to high shear stress, it is critical to ascertain viability and cell harvest yield after each pass. A case model, reported recently by Hewitt et al. [200], with 1 g/L of Cytodex 3 (0.84% volume fraction) and $\sim 2 \times 10^5$ cells/mL was considered. To enhance cell harvesting, following the first pass, the inner wall (MCs) outlet collection was passed through the ultra-low-slope trapezoidal spiral. To avoid diluting collected sample from MCs outlet after the first pass—the concentration factor is ~ 3.3 for the IW outlet collection—and reduce delay in harvesting cells from IW outlet for the second pass, $\sim 4X$ dilution factor was considered. Thus, a 45 mL MCs solution with $\sim 0.22\%$ volume fraction was prepared using cell culture medium. A total viable BM-hMSCs of $\sim 3 \times 10^6$ was added to the reservoir containing MCs, a magnetic stirrer was used to gently agitate the MC–cell solution (average cell concentration was $\sim 0.67 \times 10^5$ cells/mL).

Figures 4-4a-b display collected samples from IW and OW outlet after the second pass, respectively. Clearly, the contrast between the two samples displays cells depleted in the IW outlet (Figure 4-4a) and conversely removal of MCs from the OW outlet (Figure 4-4b). The purity of harvested cells was able to reach $\sim 99\%$ which is a crucial attribute. Harvested cells were cultured subsequently in a plastic tissue culture, as shown in Figure 4-4c, while maintaining their spindle-like morphology [204]. Furthermore, a semi-quantitative assay using PrestoBlue demonstrated that the proliferation of harvested cells in vitro compared to a control sample of unsorted cells was similar for 4 days post culture, Figure 4-4d. With respect to cell viability, Figure 4-4e illustrates the negligible reduction in viability of harvested cells from $96.5 \pm 1.32\%$ (control sample, $n=3$) to $95.3 \pm 1.15\%$ (OW outlet-I) and $93.16 \pm 2\%$ (OW outlet-II) after the first and second pass respectively. After counting, cell harvest results showed $76.62 \pm 2.1\%$ and $17.21 \pm 0.6\%$ cell recovery from the OW outlet at first and second pass respectively, and $6.16 \pm 1.80\%$ cell loss through the IW outlet at the end of process displayed in Figure 4-4f. The

sum of yield (sum of cells harvested from the OW outlet over the total cell harvest from all outlets) can reach ~94%.

Quality of the harvested BM-hMSCs can be checked by a multipotency test to assess whether the cells are capable of differentiating into adipocytes, chondrocytes, and osteoblasts. Results from this multipotency test indicated that the multipotency of the harvested BM-hMSCs was retained and not compromised. After 28 days of trilineage differentiation into the adipogenic, chondrogenic, and osteogenic lineages, the cells showed positive staining for the 3 differentiated lineages, as shown in Figure 4-4g. Formation of lipid vacuole visualized by Oil Red O confirmed adipocytic phenotype [205, 206], the presence of stained Alcian Blue-glycosaminoglycan complex showed typical chondrocytic phenotype [205, 207] and mineralized matrix stained by Alizarin Red S indicated osteoblastic phenotype [205, 208].

Close scrutiny of shear rate distribution accomplished numerically across the spiral channel at the working flow rate of ~30 mL/min (Figure S4-5) reveals that its magnitude is smaller than the shear rate of 3000 s^{-1} recently verified for volume reduction of hMSC using TFF [189]. Moreover, the present configuration of the scaled-up spiral with a decreasing-Dean mode, where outlets are placed at the outermost of the spiral curve, leads to ease of parallelization in a plane and sizable scaling out of the throughput via multiplexing spiral channels, as recently reported by our group [2, 34]. As a result, the designed spiral could potentially be stacked up to deliver on a more relevant, industrial scale (~1-5 L/min) in practice. This proposed inertial-based filtration method offers beneficial attributes such as a closed system, scalability, and continuous mode (vs. batch processing) that are appreciated for large-scale cell manufacturing in downstream processing [174, 185].

Though there is recently a paradigm shift towards dissolvable MCs to circumvent separation following cell expansion, the majority of commercially available MCs widely adopted are non-dissolvable [157, 199]. On the other hand, emerging

thermally-responsive MCs for culturing adherent cell types [209, 210] may eliminate the need for enzymatic treatment of cells, such as exposure to trypsin but the MCs still have to be separated. There will likely be advantages and downsides for each option chosen whether using dissolvable MCs or non-dissolvable MCs. Furthermore, the device demonstrated is versatile, and it can perform MC retention, removal of large-sized particulates from manufactured cell products such as MSCs.

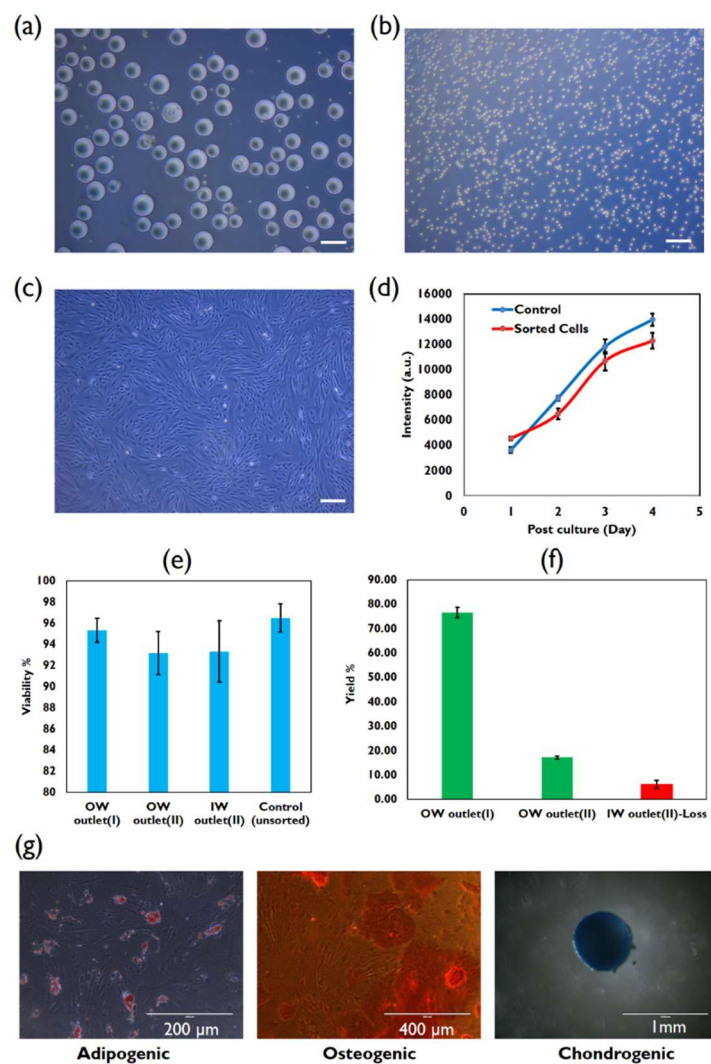


Figure 4-4 Collected samples from (a) the inner wall (IW) outlet and (b) the outer wall (OW) outlet (scale bar is 200 μm) using the ultra-low-slope trapezoidal spiral. (c) monolayer culture in a 6-well plate in day 5 and (d) PrestoBlue assay displays semi-quantitative growth of harvested BM-hMSCs compared to control sample. (e) Viability of harvested BM-hMSCs from the OW outlet at pass (I,II) and the IW outlet at pass (II) compared to initial viability. (f) Yield gains from the OW outlet at first and second pass and loss from the IW outlet at second pass. (g) Multipotency assay of harvested BM-hMSCs using Red-oil solution, alizarin red and alcian blue to stain lipid droplets (adipocytes, left panel), calcium deposits (osteoblasts, central panel), and extracellular matrix proteins (chondrocytes, right panel) respectively.

4.5 Summary

A high-throughput trapezoidal spiral channel is designed with channel hydraulic diameter of ≈ 1 mm to focus microcarriers with particle clogging ratio of 0.35 near the inner wall whereas the cells are mainly dispersed within the Dean vortices. An ultra-low-slope trapezoidal spiral with ($\tan(\alpha)=0.0375$) is found that it can focus microcarriers efficiently with high microcarrier volume fractions ($V_f < 2\%$) and the microcarriers can be removed from the inner wall outlet at $Re \sim 300-400$. The established channel is employed to remove microcarriers from human mesenchymal stem cells suspension at ~ 30 mL/min ($Re \approx 326.5$) with total yield of $\sim 94\%$ after two passes. Overall cell viability decreases by less than 5 %. The sorted cells are differentiated to adipocytes, osteoblasts and chondrocytes, showing that the sorted cells preserve their multipotency when undergoing filtration process.

Chapter 5 Scaled-up Inertial Microfluidics: Retention System for Microcarrier-based Suspension Cultures

According to the previous chapter, some discrepancies such as the minimum particle confinement ratio required for large-sized particles ($a > 100 \mu\text{m}$) compared to the micron-scale channels are found using Dean-flow coupled inertial focusing. In this chapter, a comprehensive study is carried out to uncover effect of scaling up on Dean-flow coupled inertial focusing. A focusing map illustrating the critical threshold of channel hydraulic diameter is established. Moreover, a unique inflection point focusing is reported. It outperforms the conventional focusing in rectangular and trapezoidal channels concerning high particle volume fractions ($V_f \sim 3.4\%$) and a broad range of particle clogging ratio ($0.086 < K < 1$). The utility of this device as a high-throughput and continuous retention system for cell-microcarrier suspension culture has been showcased.

5.1 Introduction

Unlike biological sample processing where the target particle size is in order of $\sim 10 \mu\text{m}$, inertial focusing has drawn attention recently for other industrial applications such as water treatment and bioprocessing, in which the target particle size is in order of $\sim 100 \mu\text{m}$ [192]. Enlarged particle sizes of $\sim 10\times$ necessitate scaling up of channel dimensions based on the empirical linear function of $a/D_H > 0.07$ [25] to maintain inertial focusing and to also avoid clogging channels. Having benefited from scalability along with parallelization, Miller et al. [192] recently demonstrated the concentration and classification of large polystyrene particles with total throughput of $\sim 1 \text{ L/min}$ by stacking 20 toroidal spiral channels. In this study, to reduce the channel footprint and boost the Dean magnitude, although the channel

cross-section was scaled up, the radius of curvature was not scaled up correspondingly based on similarity criteria (see section 5.3.1).

From the $D_e \propto D_H^{1.5}$ equation, it can be concluded that scaling up dimensions of channel cross-sections ($\geq 5X$) amplify the Dean vortices noticeably; however, the impact on secondary flow and inertial particle focusing dynamics has not yet been investigated fully. Moreover, recent modification of a rectangular spiral to a trapezoid (with a larger outer wall) has shown to alter the structure of Dean vortices [48, 49], resulting in not only enhanced separation resolution, but also boosted throughput by increasing particle volume fraction and channel aspect ratio. Interestingly, in trapezoidal spiral microchannels, a size-dependent equilibrium was formed near the outer wall located at the vortex cores [48, 49] which was capable of trapping a broad range of particles after exceeding a critical flow rate. It was shown experimentally that increasing the slope ($\tan(\alpha) = (H_{\text{outer wall}} - H_{\text{inner wall}})/W$) from ~ 0.06 to 0.13 expedited particle migration toward the outer wall [48, 49], though the underlying mechanism is not fully elucidated. Concentration, purification and volume reduction processes [2, 211] in various industrial and bioprocessing steps are all referring to one similar process: the removal or collection of all particles regardless of size. Unlike micron-scale trapezoidal spiral channels, focusing was not established close to outer wall for scaled-up and low-slant trapezoidal spiral channels ($\tan(\alpha) < 0.1$) [212] (Chapter 4). Here, a trapezoidal spiral with large slant ($\tan(\alpha) = 0.2$), therefore, was investigated. In addition, particle focusing near the larger side wall can potentially entrap a broader range of particles ($K = a/H_{\min} \geq 0.1$, H_{\min} is the shorter side wall), while it is feasible to reach $K \sim 1$ without clogging the channel; however, rectangular spirals have a limitation on the range of particle clogging ratio ($0.07 < K < 0.5$) previously uncovered in micron-scale channels (Figure 5-1a) [49, 84, 126]. Nonetheless, a much larger K factor ($K > 0.175$) required for the Dean-coupled inertial focusing at larger particle sizes ($a \geq 100 \mu\text{m}$) has been found experimentally.

In this chapter, effect of scaling-up channel dimensions on the secondary flow and particle focusing dynamics is studied in rectangular and trapezoidal spiral channels. More insight into particle focusing dynamics within different loops (i.e. Dean magnitude) of scaled-up spirals were provided. The results showed that an optimized rectangular spiral length (i.e. minimum number of loops required) was dependent on the purpose of operation (i.e. particle separation and/or filtration) and working flow rate (Re number). To further boost the working Dean number (i.e. throughput) and elevate the range of particle clogging ratio (K), a scaled-up trapezoidal spiral with a large slant ($\tan(\alpha)=0.2$) was investigated (Figure 5-1).

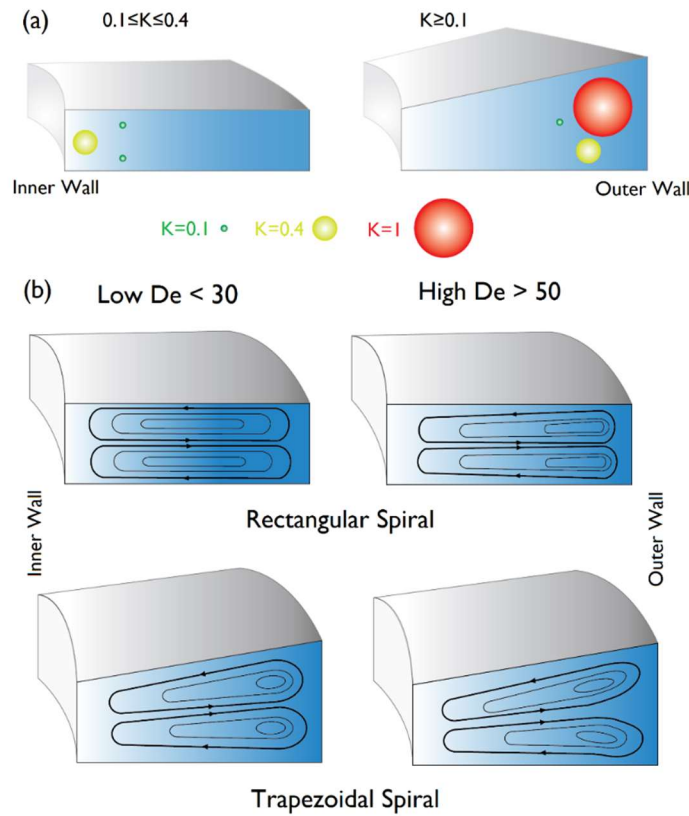


Figure 5-1 (a) Schematic variation of particle clogging ratios in a rectangular spiral and a trapezoidal spiral with large slant ($H_{outer\ wall}/H_{inner\ wall}=1.8$); it shows that a broader particle size range can be entrapped close to the outer wall of trapezoidal spiral. The particle clogging ratio can potentially increase to $K \sim 1$ without clogging the channel. (b) Schematic structures of Dean vortices of rectangular and trapezoidal spirals for low and high Dean magnitude. The Dean vortex structure in rectangular spiral channels can be altered by an increase in Dean magnitude itself and/or a transformation of the cross-section to a trapezoid.

5.2 Material and methods

5.2.1 Design and fabrication

The designed spiral channels have 6 loops for both the rectangular and trapezoidal cross-sections. The radius of curvature varies from 5 to 29 mm (measured from the inner wall). The minimum channel height was considered $H=0.5$ mm ($K<0.5$) to avoid channel clogging ($100\text{ }\mu\text{m} < a < 250\text{ }\mu\text{m}$). The moderate channel $AR=4$ and higher were considered (because the lower AR is not appropriate to have a high-throughput separator device). The height of the rectangular spiral was 0.5 mm, and the height of trapezoid increased from 0.5 mm (inner wall) to 0.9 mm (outer wall). The width of spiral channels was fixed at 2 mm. The channels were fabricated using aluminum molds and soft lithography described in previous chapter.

5.2.2 Sample preparation

Different types of neutrally buoyant particles were used to characterize the spiral devices. Fluorescent labeled particles with 100 μm in diameter (Phosphorex, Inc., USA) and 175 μm particles (Cytodex 3, GE Healthcare, USA) were diluted with DI water to reach 0.01% and 0.1-0.2% volume fraction respectively to decrease particle-particle interaction. To enhance the resolution for bright field microscopy, Cytodex 3 particles were dyed with trypan blue (0.1% volume fraction).

5.2.3 Cell culture

5.2.3.1 Monolayer cell culture

Human bone marrow-derived mesenchymal stem cells (RoosterBio, USA) were seeded at 5000 cells/cm² and cultured in T175 flasks (Nunc Easy Flask 175cm² Nuclon Delta Surface, Thermo Scientific, USA) in 40 mL MEM-Alpha (Gibco, USA) supplemented with 10% v/v Fetal Bovine Serum (FBS, Gibco, USA) and 1% v/v Pen-Strep (Pen-Strep Solution, Biological Industries, Israel). To perform cell count, 5 μL of Solution-13 stain containing acridine orange and 4',6-diamidino-2-

phenylindole (DAPI) (Solution 13 AO-DAPI 1mL, Chemometec, Denmark) was spiked into 100 μ L of suspended cell sample. The viable cell count was measured by the Nucleocounter (Nucleocounter NC-250, Chemometec, Denmark).

5.2.3.2 Stirred culture

5 g of Cytodex 3 microcarriers (GE Healthcare, USA) was soaked in 500 mL of PBS (10X Phosphate Buffered Saline, 1st Base, Singapore, diluted with deionized water in 1:10 ratio) for 3 hours, rinsed twice with PBS and autoclaved. The concentration of the microcarrier stock is 10 mg/mL of Cytodex 3 in PBS. 2 mg/mL of Cytodex 3 was seeded with 2.4×10^4 cells/mL cultured in MEM Alpha supplemented with 10% v/v FBS and 1% v/v Pen/Strep. A 125-mL disposable spinner flask (Corning, USA) was used. To make up 60 mL of cell-microcarrier culture volume, 12 mL of Cytodex 3 stock solution rinsed already with culture medium and 8 mL of cell suspension containing 1.44×10^6 cells were added into 40 mL of culture medium. The spinner flask was agitated at 38 rpm. Cells were cultured on microcarriers for seven days in an incubator at 37 °C and 5% CO₂ level. 50% fresh culture medium was exchanged for all spinner cultures on day 2, 4 and 6.

5.2.4 Cell-microcarrier characterization assay

5.2.4.1 Cell counting

To measure total cell concentration, 100 μ L of cell-microcarrier culture was lysed using 50- μ L lysis buffer (Reagent A100 Lysis Buffer, Chemometec, Denmark) and then 50 μ L of stabilizing buffer (Reagent B Stabilizing Buffer, Chemometec, Denmark) was added and mixed. 5 μ L of 4',6-diamidino-2-phenylindole (DAPI) (Solution 12, Chemometec, Denmark) was spiked into the sample. The stained sample (total cells) was counted by the Nucleocounter. To count dead cells, the cell-microcarrier sample was stained with Solution 12 without lysis.

5.2.4.2 Flow cytometry

Having been harvested, total 10^5 cells were resuspended in cold PBS supplemented with 1% v/v BSA (Bovine Serum Albumin, USA). Cell surface markers CD34, CD90, CD45, CD105, CD73 and CD146 (Biolegend, USA) were analyzed using flow cytometry (Novocyte, ACEA Biosciences Inc, USA). Cells were incubated with the antibodies for 30 minutes in an ice box and in the dark.

5.2.5 Numerical simulations

The spiral channel was simulated using a commercial software, ANSYS Fluent. The Hex map mesh was imported from Gambit, and the continuity and Navier-Stokes equations were solved subsequently by using a SIMPLE algorithm. The inlet and outlet boundary conditions were set to inlet velocity and ambient pressure. No-slip velocity was applied for walls boundary conditions. Liquid water properties, density of 998.2 kgm^{-3} and dynamic viscosity of $0.001002 \text{ kgm}^{-1}\text{s}^{-1}$, were used for fluid. Though many efforts have been made, a comprehensive net inertial lift force model to simulate inertial particle focusing exclusively for spiral channels has not been validated [80]. In this study, flow simulation was only carried out to qualitatively analyze the secondary flow and its impacts on main velocity profile, i.e. inertial lift force.

5.2.6 Experimental setup

The fluorescent particle suspension was injected into the spiral channels, mounted on an inverted epifluorescence microscope (Olympus IX71, Olympus Inc., USA) using a syringe pump (Chemyx, F200, USA). Cytodex-3 suspension was fed by a peristaltic pump (LeadFluid, BT300S). The flow rates varied from 8 mL/min ($Re \sim 100$) to 24 mL/min ($Re \sim 300$). To prevent deposition of fluorescent particles, a spherical ball (magnetic stirring bar, PTFE, spherical, 12 mm, Sigma-Aldrich, Singapore) was placed and moved inside the syringe (60 mL B-D plastic syringe)

intermittently by using another magnetic stirring bar from outside. A magnetic stirrer was used to agitate gently the suspension in the Cytodex-3 inlet reservoir. All channels were first primed by running 70% ethanol for 5 min to clear the residue and air bubbles. The images were taken (16-bit CMOS camera, optiMOS, QImaging) at different loops of the spiral channel ranging from loop 1 to loop 5. The exposure time was set to 1 s and 100 μ s for fluorescent and bright field microscopy. 100 images were staked using ImageJ software to find the location of particle streaks laterally.

5.3 Results and discussion

5.3.1 Particle focusing dynamics in the scaled-up rectangular spiral channel

Figure 5-2a shows the designed scaled-up spirals including the rectangular and trapezoidal compared to a conventional spiral. The radius of curvature, R , measured from the inner wall, varies considerably from 5 mm (base circle) to 29 mm (loop 6) and the corresponding square root of curvature ratio ($\sqrt{\delta}$) of ≈ 0.3 and ≈ 0.1 , respectively (Figure 5-2b). The radius of curvature of the scaled-up spirals is not enlarged based on similarity criteria to not only reduce the spiral footprint but to also increase the Dean magnitude (the scaled-up spirals and the conventional spiral all have a similar radius of curvature at the starting point). The De magnitude decreases rapidly at the downstream for a constant Re number as shown at Figure 5-2c. It reduces by 40% from the loop 1 to loop 5 consecutively when the channel Re is constant. To show the impact of scaling up channel cross-section independent of Re , the dimensionless parameter of curvature ratio (δ), the ratio of De/Re , is plotted against the conventional spiral (Figure 5-2d). 5X scaling-up of channel dimensions causes a noticeable increase in the curvature ratio and thus the Dean magnitude. It should be noted that the designed scaled-up spirals cannot be scaled down $\geq 5X$ based on similarity criteria due to restrictions on the innermost radius of curvature: it cannot be reduced to ≤ 1 mm ($R \leq 1$ mm). To our knowledge, the maximum reported square root of curvature ratio ($\sqrt{\delta}$) for a rectangular spiral channel was ≈ 0.2 by reduction of innermost curvature R of ~ 2 mm [127].

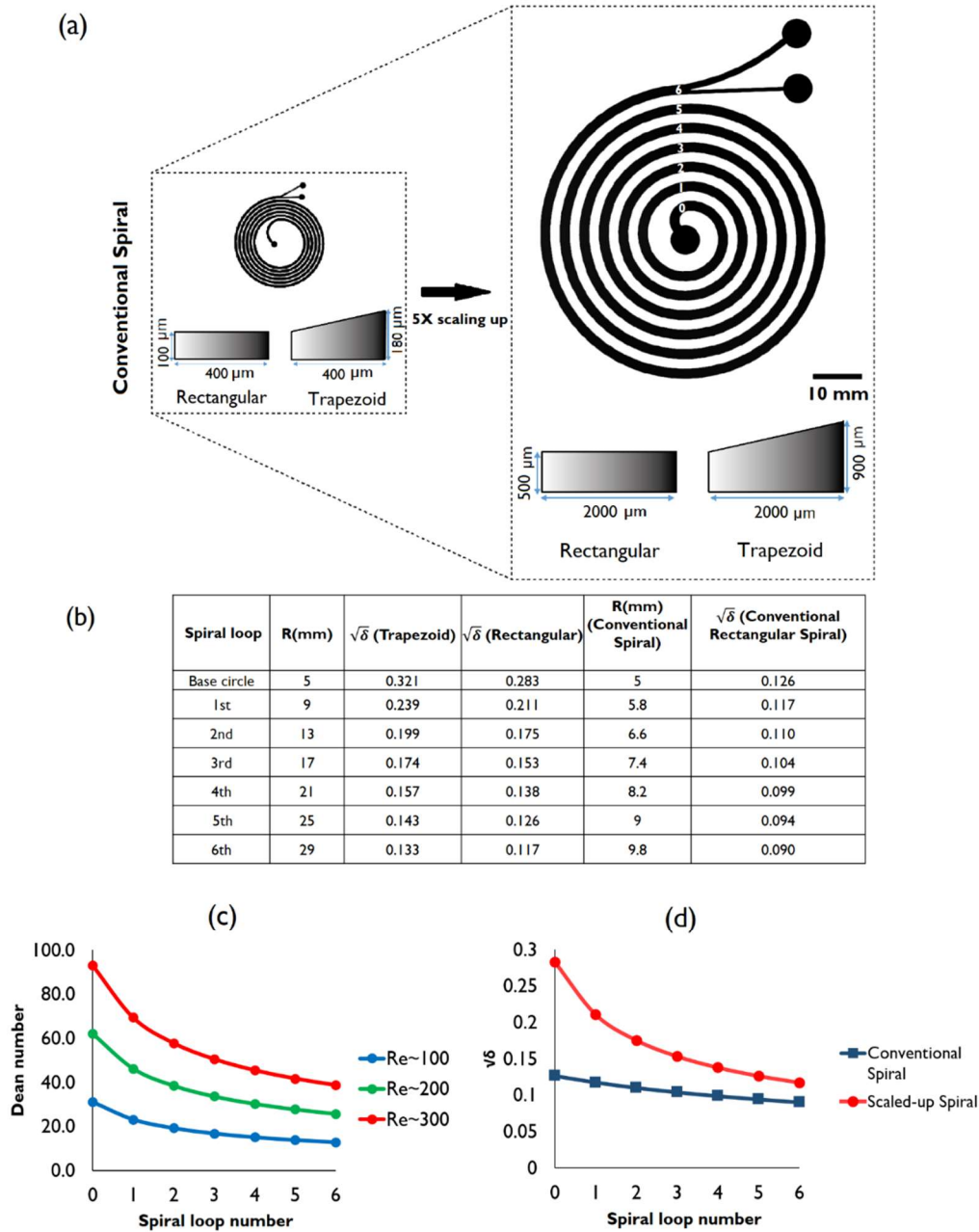


Figure 5-2 (a) Schematic outline of the scaled-up spiral with rectangular and trapezoidal cross-sections compared to a conventional spiral. (b) Specifications of curvature ratios for conventional and scaled-up spirals. (c) Dean profile of the scaled-up spirals for different Re numbers. Rapid reduction of Dean magnitude occurs due to significant enlargement of the radius of curvature as a result of scale-up. (d) The impact of scaling up channel cross-sections on the curvature ratio ($\sqrt{\delta}$).

Particle movements are progressively shown in Figure 5-3a at different loops of the rectangular spiral device. Large particles (i.e., microcarriers) with $K=0.35$ gradually focus at one lateral position close to the inner wall at low Re number (~ 100), where increasing Re to ≥ 200 results in the expansion of streak width (further migration of particles in which they exactly equilibrate next to the inner wall in loop 4 and 5). Similarly, fluorescent particles with $K=0.2$ display the same trend by migrating toward the inner wall continuously at $Re \leq 200$. It can be concluded that the moderate magnitude of $Re \leq 200$ can be utilized for particle concentration and filtration where all suspended particles in the mixture with $K \geq 0.2$ mainly focus near the inner wall (loop 4 and 5) [192]. Furthermore, one can utilize higher flow rates ($Re \sim 300$) for separation of $K=0.2$ from $K=0.35$ particles at a shorter distance (loop 2 and 3), reducing the total spiral footprint.

Intriguingly, at a higher $Re=300$, $K=0.2$ particles are mainly pushed toward the outer wall at the first loop, partially focus at the second loop close to the outer wall, then begin to defocus, sweeping back toward the inner wall (Figure 5-3a). It should be noted that the maximum separation resolution occurs between loop 2 and 3 in which the channel Dean magnitude is above 50. In comparison to equilibrium positions of $K=0.2$ particles adjacent to the inner wall when $De < 35$ ($Re \sim 100-200$, loop 3 to 5), this fast migration to the outer wall (loop 1&2) originates from the high De magnitude, while further reduction of De magnitude (greater than 40%) at the downstream causes particle dispersion (Figure 5-3a, $Re \sim 300$, $K=0.2$), which has not been reported yet in conventional curved rectangular microchannels. This fast migration of $K=0.2$ particles to the outer half of the channel cross-section, as well as the migration of $K=0.35$ particles to the inner half, for a given $Re \sim 300$, arises from the size-dependent vertical position of particles as the Dean magnitude grows. Smaller particles with $K=0.2$, due to the reduced shear-gradient lift force across channel height particularly at the inner half of the channel cross-section, get closer to the center of the channel, crossing zero Dean velocity, thereby experiencing the reversed direction secondary flow outwards away from the inner wall [84].

Another factor in regard to the fast migration of $K=0.2$ particles is the evolved structure of Dean vortices. Recently, the formation of secondary Dean vortices was experimentally demonstrated to be close to the outer wall for high-Dean flows. This is said to be responsible for trapping particles/cells with $K \approx 0.06$ at the outer half of the channel cross-section in a spiral with $AR \approx 1.6$ [194]. However, this theory has not been proved numerically and is accompanied by some uncertainties, particularly in rectangular spirals with high AR of >4 ($W > H$) [49]. Here, to capture the precise structure of Dean vortices, a helicity density (H_d) function is defined numerically (Figure S5-1, Appendix C) [213, 214]. Helicity density is a pseudo-scalar quantity and its variation from positive to negative shows alternating direction of vortex rotation. The dimensionless helicity density at the first loop of the rectangular spiral can be seen in Figure 5-3b. Increasing De magnitude to >40 results in a significant evolution of axial velocity profile and deviation of the core of maximum velocity toward the outer wall. Similarly, the Dean vortices contour, i.e. H_d , displays not only a shift in the Dean vortex cores toward the outer wall, but also a shrinking of vortex cores like trapezoidal spirals. This may account for trapping of $K=0.2$ particles located at the outer half of the channel cross-section at higher De numbers.

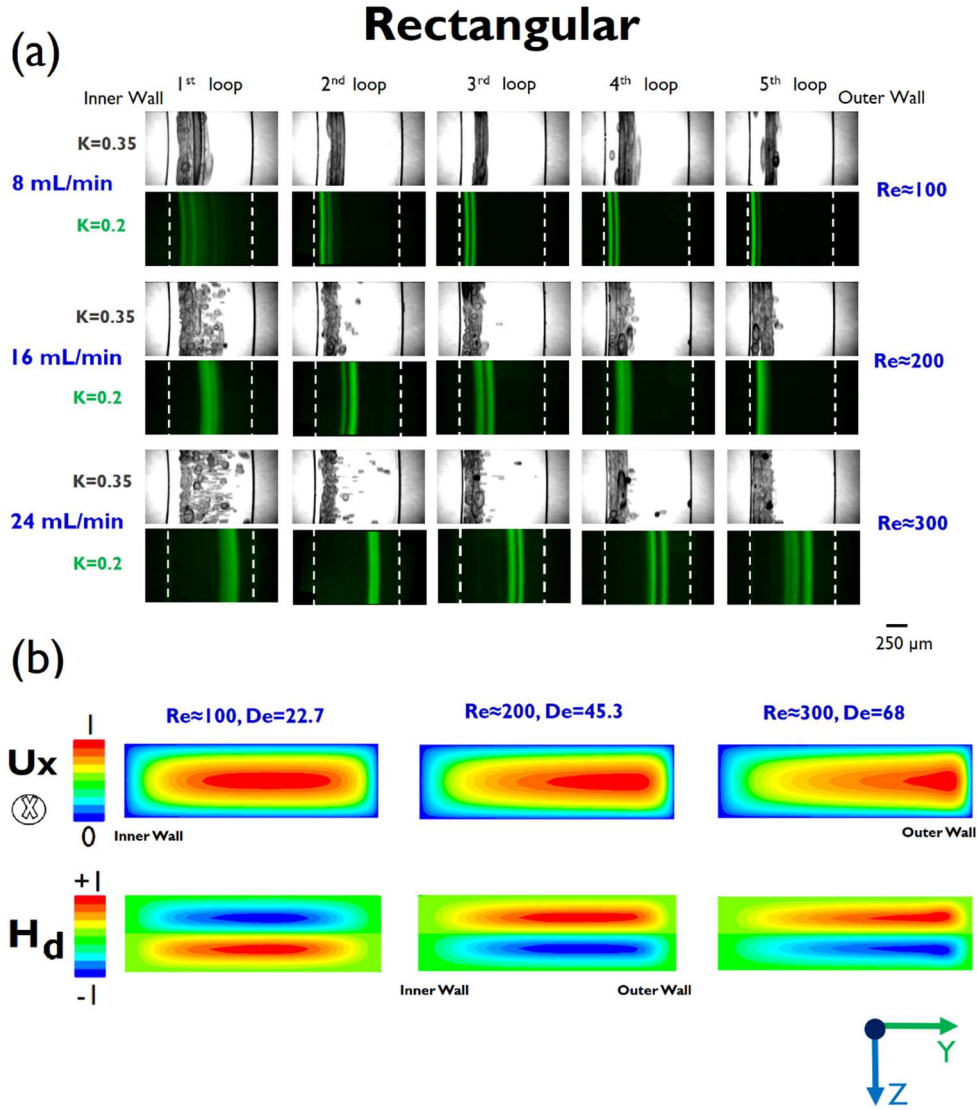


Figure 5-3 (a) Particle focusing of $K=0.35$ (175 μ m, bright field) and $K=0.2$ (100 μ m, fluorescence) are shown at successive loops of the rectangular spiral. (b) Dimensionless axial velocity U_x and helicity density contours at the first loop. Increase in flow rate and corresponding Dean magnitude transforms the axial velocity profile while the core of maximum velocity is noticeably skewed toward the outer wall. The helicity density function (H_d) shows the Dean vortex structure of the spiral channel precisely. The evolution of H_d when the channel De number increases from ~ 22.7 to ~ 68 displays movement of Dean vortex cores toward the outer wall.

5.3.2 Particle focusing dynamics in the scaled-up trapezoidal spiral channel

Figure 5-4a demonstrates the migration of particles at different loops of the trapezoidal spiral (i.e. various Dean magnitudes) at varying Re numbers ($100 \leq Re \leq 300$). Observed at $Re \approx 100$, larger particles ($K=0.35$) mainly migrate toward the outer wall (loop 1) then slowly sweep back toward the inner wall (loop 5); a clear focusing is not seen. Comparatively, smaller $K=0.2$ particles first partially focus next to the outer wall until they reach loop 3. After further travel to the downstream loops, some particles incur secondary drag force and move toward the inner wall while other particles remain trapped at vortex cores (loop 5). Given that the secondary drag force scales with particle size ($F_D \sim a$), $K=0.35$ particles are significantly influenced by secondary forces when compared to that effect on $K=0.2$ particles. Surprisingly, increasing channel Re to 200 causes fast migration of $K=0.35$ particles in the loop 1 and 2. Nevertheless, further traveling of particles to the downstream results in particle defocusing and mixing under the influence of secondary flow. Unlike the larger particles, $K=0.2$ particles gradually focus perfectly next to the outer wall. Finally, further increasing the flow Re to 300 leads to the entrapment of all particles with $K \geq 0.2$ in the vortex cores close to the outer wall (loop 5) as reported previously for the conventional trapezoidal spiral microchannels at high- Re flows [48, 49].

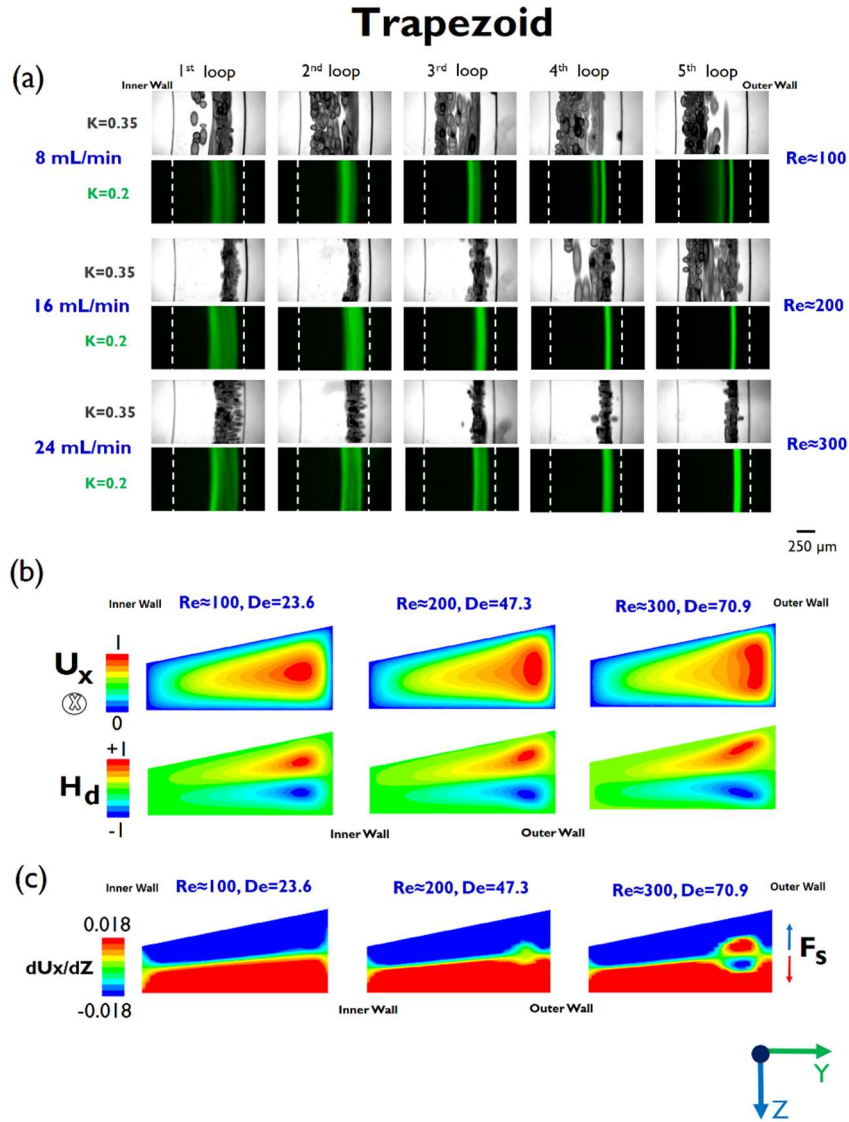


Figure 5-4 (a) Particle focusing of $K=0.35$ (175 μm , bright field) and $K=0.2$ (100 μm , fluorescence) at successive loops of the trapezoidal spiral. Interestingly, $K=0.35$ particles migrate fast toward the outer wall at first loop for $Re \approx 200$ under the dominating shear-gradient lift force while further traveling to the downstream spiral loops causes particle mixing despite the reduction of Dean magnitude by 40%. (b) Evolution of dimensionless axial velocity and Dean vortex contour of the trapezoidal spiral by increasing De number. (c) Dimensionless shear rate field of partial of axial velocity with respect to height of the trapezoid at the first loop (to find out the boundary where the sign of shear rate alternates, its range is lowered). Increasing Dean to ~ 70 results in formation of a dipole near the outer wall.

Figure 5-4b depicts the evolution of axial velocity profile and structures of Dean vortices by growing Dean magnitude. Figure S5-4 demonstrates the existence of an inflection point in the axial velocity profile located at the outer half of the channel cross-section for high $De \approx 47$, resulting in fast migration of $K=0.35$ particles toward the outer wall due to inflection point focusing in which the direction of shear gradient lift force switches [215]. Further increasing De to ≈ 70 causes dispersion of $K=0.35$ particles at the loop 1 (Figure 5-4a, $Re \approx 300$, $K=0.35$). At high De magnitude of ≈ 70 , the core of maximum axial velocity contour is changed from convex to concave near the outer wall. Investigation of the vortex structure shows that the vortex cores move away from each other, and the boundary of shear rate in partial axial velocity with respect to height ($\frac{\partial U_{axial}}{\partial z}$), upon a sign change, alternates along the height and forms a dipole near the outer wall (Figure 5-4c). Consequently, particles are not able to focus efficiently at loops 1 and 2 (the boundary of the shear rate does not alternate for the rectangular spiral when Dean magnitude increases to $De \approx 70$ as shown in Figure S5-2a. Another major component of the shear-gradient lift force, which could affect the equilibrium state near the inner wall, is the derivative of axial velocity along the channel width ($\frac{\partial U_{axial}}{\partial y}$). Figure S5-2b displays more uniform shear rate field specifically at the inner half of the channel cross-section, i.e. loss of shear-gradient lift force, for the trapezoidal spiral).

To elucidate further the observed phenomenon – fast migration of particles to the outer half of the channel cross section within loop 1 ($Re > 100$, $De > 40$) of the trapezoidal spiral with large slant, compared to the rectangular spiral – secondary flow is investigated numerically (please see Appendix C, Figure S5-3). Overall, secondary flow dragging particles toward the outer wall at the horizontal midplane reduces for trapezoidal spirals at the inner half of the channel cross-section. Therefore, the main remaining factor responsible for the fast migration of $K=0.35$ particles (Figure 5-4a, $Re \approx 200$, loop 1) is the inflection point focusing which originates from high De magnitude ($De \geq 50$) altering the shear field (Figure S5-4).

5.4 Re- D_H operation map

Given the well-known influence of particle confinement ratio ($C=a/D_H$) on inertial focusing, a series of scaled-up rectangular and trapezoidal channels were designed systematically to survey the effects of channel hydraulic diameter (D_H) on inertial focusing for large-sized particles (Cytodex 3, $a\sim 175\ \mu\text{m}$), all channels' specifications are described in Table S5-1 (Appendix C).

The focusing map (Figure 5-5) shows existence of a critical threshold for channel hydraulic diameter ($D_H\sim 1\ \text{mm}$). There is only a narrow zone in which focusing can happen (displayed in green) although, based on theory, a wider range of channel hydraulic diameter ($D_H>1.6\ \text{mm}$) is expected for inertial focusing. Scaling up channel hydraulic diameter one order of magnitude from $\sim 0.1\ \text{mm}$ (micron scale) to $\sim 1\ \text{mm}$ (millimeter scale) causes reduction of absolute flow velocity for a given channel Re number ($Re\leq 500$). Therefore, the practical ramifications of scaling up is a damping effect on inertia or momentum of flow ($U\propto Re/D_H$). Consequently, the secondary flow velocity that is approximately ~ 1 -10 percentage of average flow velocity is influenced much more severely, resulting in a non-focusing zone (orange).

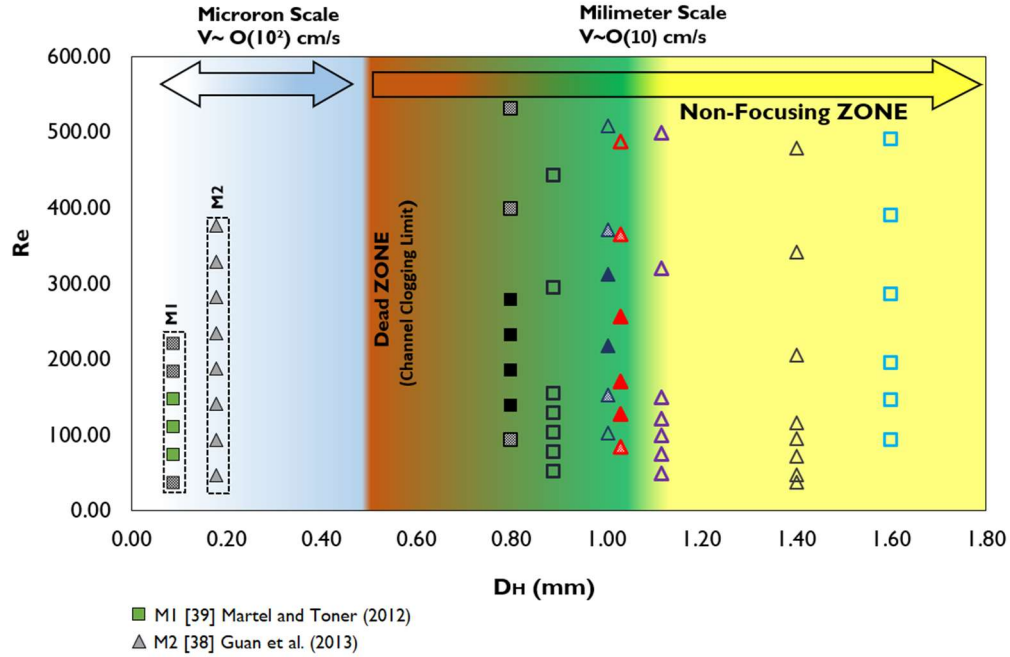


Figure 5-5 Particle focusing map. The square and triangular markers represent the rectangular and trapezoidal channels respectively. Solid markers show focusing (particle band width $< 4a$), markers with pattern depict partial focusing ($\sim 4a < \text{particle band width} < 6a$) and plain markers display non-focusing (Only inside the Green zone focusing can be developed for millimeter scale channels). The focusing map here considered focusing either near the inner wall or the outer wall.

Unlike the micron scale channel, the minimum particle (microcarrier) confinement ratio (C) required is found greater than 0.2 and 0.17 for the rectangular and trapezoidal channels respectively (The minimum C reported for micron-scale particle is greater than 0.07).[25] Accordingly, scaling up channel for larger particle size ($250 \mu\text{m} < a < 500 \mu\text{m}$) will be more difficult (Figure S5-6, $D_H \geq 2 \text{ mm}$) where the average flow velocity falls below 20 cm/s even at a large channel $Re \sim 400$ (Figure S5-7), therefore existence of Dean flow-coupled inertial focusing will be deteriorated.

There are some other factors which can affect inertial focusing at larger particle size ($a \geq 100 \mu\text{m}$). Inherently, possessing higher coefficient of variation for large-sized particles ($CV > 10\%$) than that of micron-scale particles ($CV < 5\%$) brings about more

restriction in focusing regime. Lastly, the deviation of large-sized particle density from being ideally neutrally buoyant can disrupt inertial focusing further compared to micron-size particle focusing. Scaling gravity force over the inertial lift force demonstrates the boosted impact of gravity force for larger channel size as follows:

$$f_g = \frac{mg}{F_L} \propto \frac{\rho_P}{\rho_F} a^{-1} \left(\frac{D_H}{U}\right)^2$$

Where the shear rate $G=U/D_H$ is decreasing for scaled up channels (reduction of flow velocity and an increase in D_H simultaneously), i.e. the power law function of $1/G^2$ grows faster than canceling effect of particle size, a^{-1} .

5.5 Microcarrier concentration and/or filtration

Microcarrier suspensions ($\sim 100 \mu\text{m}$ to $\sim 300 \mu\text{m}$ diameter of beads) are used, along with a stirred tank bioreactor, to increase the culture surface area to volume ratio for proliferation of cells in cell therapy [157]. The optimum concentration of microcarriers (MC) has not been reported as it is dependent on cell type, MC properties, bioreactor type, and culture volume. However, a diverse range of ~ 3000 MCs/mL to ~ 15000 MCs/mL is reported in the literature [164, 190, 198-203].

Dealing with high particle concentrations is of great importance due to the limits of inertial focusing in low particle volume fractions of $<1\%$ [26, 27, 48, 49], regarded as one of the major drawbacks for many applications. For example, dilution of culture broth in a bioreactor containing MC-cell complexes not only reduces throughput but also imposes some major disadvantages such as increasing cost of processing and extra concentration step after filtration, which negate the advantages of applying inertial-based (membrane-less) filtration system. To study the effect of particle concentration, four different suspensions with 1500 MCs/mL, 3000 MCs/mL, 6000 MCs/mL, 12000 MCs/mL, corresponding to 0.42%, 0.84%, 1.7% and 3.4% volume fractions (the ratio of total volume of MCs in unit volume; approximated based on MC concentration and the average diameter of MCs), were prepared.

Figure 5-6 shows that in all cases, while MC volume fractions are greater than or equal to 0.42% ($V_f \geq 0.42\%$), the perfect MC focusing for $Re \approx 300$ at the last loop (5th loop) is spoiled, unlike the low MC concentrations (0.1% MCs, $K=0.35$, Figure 5-4a). This particle defocusing next to the outer wall proves the limitations of inertial focusing, in which the core of Dean vortices exists while excessive numbers of particles drift to the inner wall and subsequently mix due to the secondary flow drag while its magnitude gradually declines. Nevertheless, a MC-free zone can be observed next to the inner wall of first loop regardless of high MC concentration, showing superiority of the inflection point focusing. Therefore, a single-loop spiral channel, which is identical to the first loop of the trapezoidal spiral, along with bifurcation is fabricated to filter and/or concentrate microcarriers (Figure 5-7a).

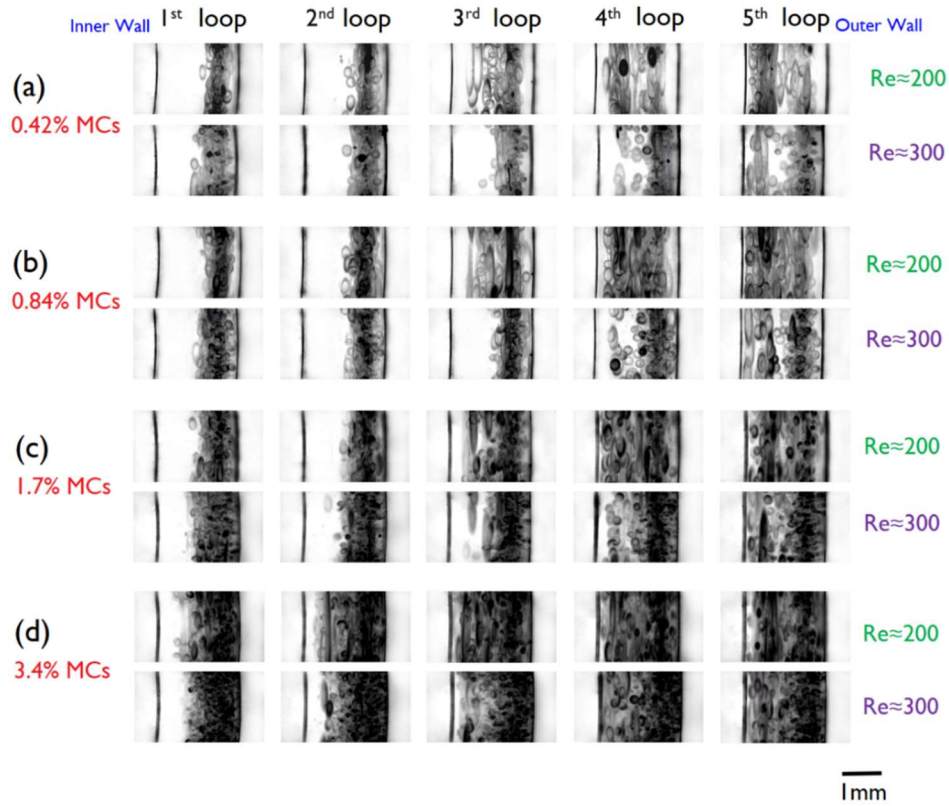


Figure 5-6 Impact of microcarrier volume fraction of (a) 0.42% (b) 0.84% (c) 1.7% (d) 3.4% on particle focusing at different loops of the trapezoidal spiral for $Re \geq 200$. The particle focusing at 5th loop is ruined even for $Re \approx 300$ when $V_f \geq 0.42\%$ whereas the particle-free region remains at the inner half of the channel cross-section for the first loop.

Characterization of the single-loop spiral channel is displayed in Figure 5-7b for different MC volume fractions. As can be seen for MC suspensions with volume fractions of $<1\%$, a lower flow rate of 16 mL/min can generate enough shear force to push MCs toward the outer wall (Figure 5-7b, 0.42% MCs and 0.84% MCs), but increasing the MC volume fraction to $>1\%$ results in a wider MC dispersion, which necessitates an increase in flow rate to ≥ 24 mL/min (Figure 5-7b, 1.7% MCs and 3.4% MCs) to separate MCs efficiently to the outer outlet.

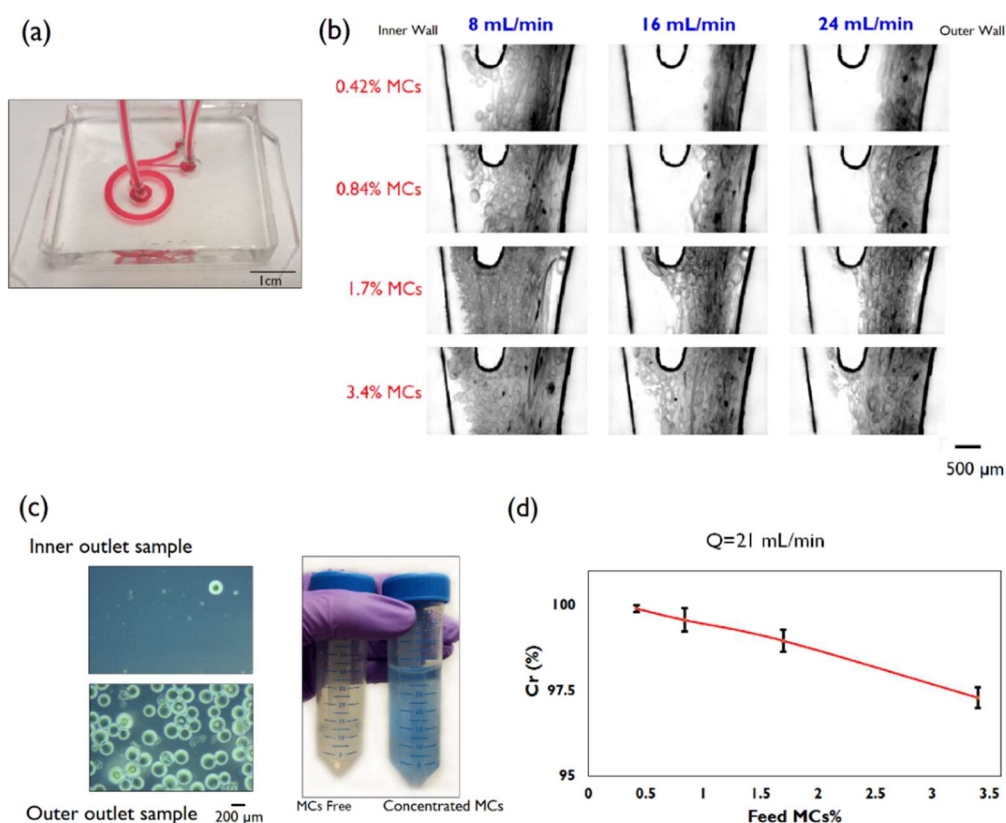


Figure 5-7 (a) Image of the fabricated single-loop trapezoidal spiral channel (the microchannel was filled with a red dye for visualization). (b) Microcarrier focusing behavior at the bifurcation for different flow regimes and microcarrier (MC) volume fractions of 0.42%, 0.84%, 1.7% and 3.4%. (c) Pictures of samples collected from the inner outlet and the outer outlet for 1.7% MCs feed (the concentrated MC sample has a blue color due to the trypan blue-dyed MCs). (d) The rejection factor for different microcarrier volume fractions when flow rate is 24 mL/min ($n=3$).

To evaluate the quantity of MCs which are elutriated from the inner outlet, the relative rejection factor (Cr) parameter is defined as follows [34]:

$$C_r = 1 - \frac{C_c}{C_s} \quad (5.1)$$

where C_c and C_s are the number of MCs collected from MC-free sample (inner outlet) and feed MC in unit volume. The higher rejection factor represents a lower magnitude of MC loss as well as higher purity in the MC-free sample. Figure 5-7c shows images of samples collected from the inner outlet (MC-free) and the outer outlet (concentrated MC) for 1.7% MCs feed at a flow rate of 24 mL/min. It should be noted that the ratio of sample volumes collected from the inner to outer outlets is 1:3 because the bifurcation is located about a third of the channel's width from the inner wall. However, the present single-loop spiral can accept the higher concentration without compromising purity of the particle-free sample. As demonstrated (Figure 5-7d), the rejection factor remains almost constant while increasing MC volume fraction to 1.7% and 3.4% resulting in only ~1% and ~2.7% drop in Cr , respectively.

Moreover, among other configurations of trapezoidal spirals applied for particle filtration, the performance of a scaled-up trapezoidal spiral with larger inner walls was examined (Figure S5-5). The results show that its performance is reliant on low- Re flow of ~100 regardless of large spiral footprint and low particle volume fraction ($V_f < 1\%$). [34] The best focusing is developed adjacent to the inner wall when Re number is ~100. An increase in Re results in a wider particle band even for a dilute MC suspension with low particle volume fraction of ~0.1%.

The proposed single-loop trapezoidal spiral with a large slant, in addition to substantially lesser footprint than that of the scaled-up spiral with 6 loops (Figure 5-8a), can accommodate a broader range of particle clogging ratios due to the large slant (large outer wall). Figure 5-8b demonstrates that small-sized particles with $K=0.086$ are mainly pushed away from the inner wall and exit through the outer outlet when flow rate is as high as 24 mL/min ($Re \sim 300$) though there is no focusing.

Theoretically, because the shear-gradient lift force is proportional to the power law function of particle size (Eq. 2.1), particles with clogging ratio of $K > 0.086$ can be filtered from the outer outlet. Additionally, because the height of the outer wall is 1.8 times higher than that of the inner wall, it is feasible to reach $K = (a/H_{min}) \sim 1$. Thus, the proposed single-loop trapezoidal spiral is potentially capable of filtering a suspension with diverse range of particle sizes ($50 \mu\text{m} < a \leq 500 \mu\text{m}$). However, in a rectangular spiral, the K factor cannot exceed 0.5 due to channel clogging (conventional range of the K factor for inertial focusing in a rectangular spiral is $0.1 \leq K \leq 0.4$ [84, 126, 133], Figure 5-1a, although here it was found that $K > 0.175$ required for scaled up rectangular spirals. Figure S5-8 shows no focusing developed for $K = 0.175$ particles).

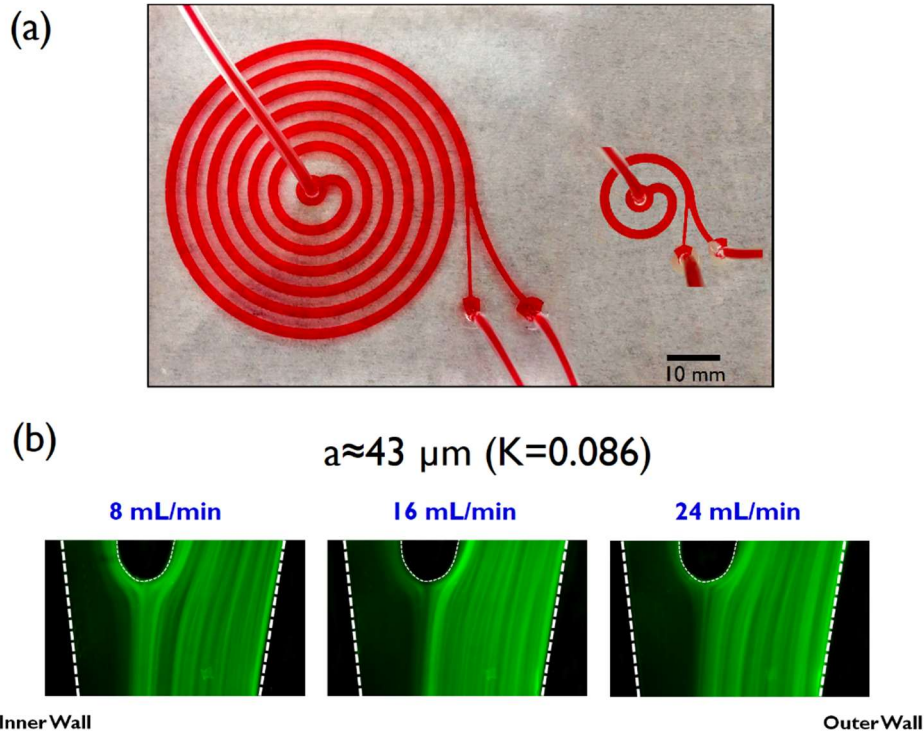


Figure 5-8 (a) Optical images of the fabricated spiral channels display the footprint of the trapezoidal spiral with 6 loops versus that of single loop. (b) Inertial migration of $\approx 43 \mu\text{m}$ fluorescent particles (Polysciences, USA) toward the outer wall at bifurcation in the single-loop trapezoidal spiral. Particles are mainly filtered from the outer outlet at a flow rate of 24 mL/min.

An increase in the slant of a trapezoidal spiral will lead to an increase in the hydraulic diameter of channel cross-sections ($D_H > 1$ mm), and thus the minimum cutoff particle size will shift to a larger size. For example, a single-loop trapezoidal spiral with $\tan(\alpha) = 0.4$ ($H_{\text{outer wall}}/H_{\text{inner wall}} = 2.6$, $H_{\text{inner wall}} = 0.5$ mm, $W = 2$ mm) cannot filter efficiently the MC suspension with $K = 0.35$, i.e. the rejection factor Cr will decrease noticeably (data is not shown).

5.6 Microcarrier-based suspension culture retention system

Since cell-microcarrier stirred culture are prone to cell damage due to exposure to high shear rate, two sets of three spinner cultures ($n=3$) were set up as case model (described in section 5.2.3). The single-loop trapezoidal spiral channel functioned as MSCs-MCs retention system to either harvest conditioned medium or carry out medium change for the spinner cultures. Separated MSCs-MCs complex from the outer wall outlet was recycled to the spinner flasks (Figure S5-9 displays the experiment configuration). Following extraction of conditioned medium from the inner wall outlet using the single-loop spiral (at inlet flow rate of ~ 20 mL/min, about ~ 8 min), the fresh medium was added at day 2, 4 and 6.

Although there was ~ 1 -2% MSCs-MCs loss from the inner wall outlet, cell culture growth profile (Figure 5-9a) revealed ~ 8 -fold cell expansion having similar trend to control spinner flask cultures ($n=3$). From Day 3, clumping of MCs were observed in all sets (Figure S5-10). MSCs harvested at day 7 maintained their immunophenotypic expression according to ISCT criteria [204], being positive for CD73, CD90, CD105 and negative for markers CD34 and CD45 (Figure 5-9b). This suggested that cells on microcarriers passing through the single-loop trapezoidal spiral channel has no negative impact on cell growth and identity.

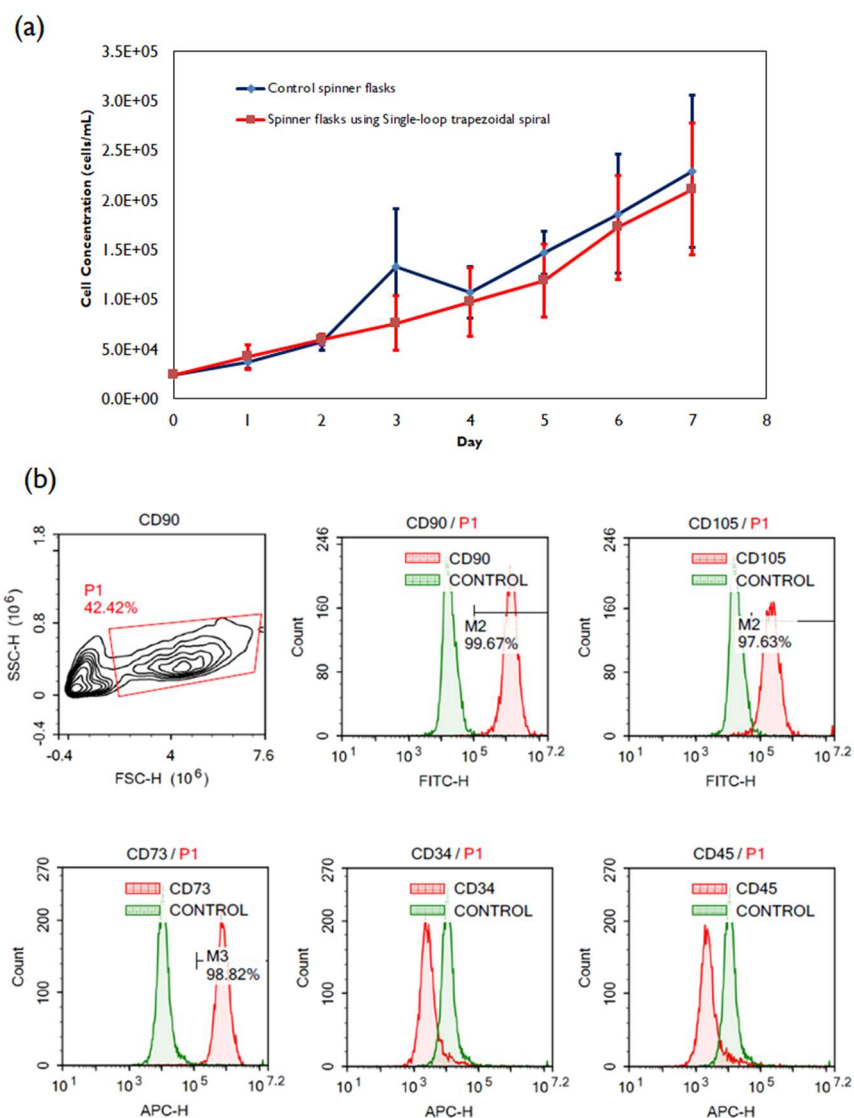


Figure 5-9 (a) 7-day cell growth profile of human Bone Marrow-derived Mesenchymal Stem Cells cultured on Cytodex 3 microcarriers in spinner flasks. (b) Histograms of cells' surface markers expression harvested at day 7.

Qualitatively smaller MSCs-MCs clumps have been observed, compared to control spinner flask cultures, when using the single-loop spiral channel for longer period (at day 7, running for ~20 min). This potentially can be of interest for large scale bioreactor because smaller clump size makes separation and harvesting of cells easier at the end of cell expansion.

5.7 Summary

A series of experiment is carried out to investigate Dean-coupled inertial focusing in scaled-up channels. The established focusing map shows minimum particle confinement ratio of 0.17 is required. Moreover, an inflection point focusing without the aid of sheath flow is demonstrated using the scaled-up trapezoidal channel with large slant ($\tan(\alpha)=0.2$, $D_H \approx 1$ mm). A single-loop trapezoidal spiral channel based on the inflection point focusing is developed while it can focus and filter a broad range of particle sizes ($0.086 < K < 1$). Lastly, the single-loop trapezoidal spiral channel is applied for retention of microcarrier-cell complex in suspension cultures. Biological validations prove that the identity of mesenchymal stem cells is preserved.

Chapter 6 High-throughput Separation of Particulates Matter Contamination from Manufactured Cell Products Using Inertial Microfluidics

In cell-based therapeutic products, particulates matter contamination is of great concern, as it adversely affects patient safety and product quality. In contrast to protein-based biologics, manufactured cell products are relatively large (above submicron) and this makes the use of membrane filtration impossible. Thus, a broad range of visible and subvisible particulates cannot be filtered out from the final product. In this chapter, a hybrid method is proposed to remove particulates from the final cell therapy product. In addition to the standard sieving process that excludes presumably a diverse range of particulates, inertial-based filtration is performed after sieving to alleviate the particulates count. High-throughput spiral inertial microfluidic channels were designed and demonstrated to filter a broad range of particulates from 75 μm down to 25 μm from mesenchymal stem cell (MSC) suspensions with an efficiency of greater than 95%. Simultaneously, the proposed method fractionated the MSC population to harvest the medium- to small-sized subpopulations ($d \leq 20 \mu\text{m}$) that are the most multipotent and least senescence-associated subpopulations.

6.1 Introduction

As cell therapies from numerous clinical studies advance towards commercialization, new challenges are presented to the cell therapy (CT) industry [154]. The manufacturing process of these cell therapies must comply with regulations to ensure efficacy and patient safety. With the growing number of

clinical trials, particulate contamination in the final formulation of CT products is raising greater concerns with regards to patient safety [166, 172]. Since the manufactured cells are mostly administered intravenously, adverse events such as blood flow occlusion and inflammatory responses introduce serious risks to the recipients [165, 216]. Furthermore, the presence of particulates could impact the quality of the cell therapy itself. Although microfiltration is a routine step in manufacturing of biologics, it cannot be implemented for cell therapies as cells are much larger with diameters that are above submicron. This distinguishes the manufacturing process for CT manufacturing from that of other biological products [166, 175].

Recently, a paradigm shift towards single-use systems is evident in biomanufacturing as well as cell manufacturing. Single-use systems offer attributes such as eliminating the need for washing and sterilization of lot, and boosting the speed for product development in patient-specific or off-the-shelf cell therapy. However, particulates, extractable and leachable materials are inevitably introduced into the final products when single-use systems are deployed [161, 167, 175, 184]. While the development of advanced materials that produce less extractables and leachables is underway, establishing particulate-free cell therapy products seems unachievable with current technologies [175]. In particular, in addition to inherent and intrinsic particulates which originate from cell products such as cell debris [217], formulation and packaging, there are unavoidable and extrinsic sources of particulates such as personnel activities and hair [166].

Membrane-based filtration is an attractive means of downstream processing due to its ease of implementation. However, there are restrictions on pore size due to the size and sensitivity of cells to shear stress. Recently, it was shown that removal of large-sized particles such as microcarriers ($>100\text{ }\mu\text{m}$) from stem cell suspensions, using mesh size $\sim 30\text{ }\mu\text{m}$ causes low cell yields of 70% [189]. The smallest mesh size that could keep high yield while sustaining cell integrity and morphology is approximately $50\text{-}60\text{ }\mu\text{m}$ [188, 190]. Risk of filtration fouling remains high when

smaller screen sizes are used. Therefore, despite removal of a broad range of large-sized particulates greater than 70 μm (diagonal size of opening) using presumably 50- μm sieves, another broad spectrum of visible and subvisible particulates together with cells can pass through the filtration process. It is of vital interest to minimize the particulates burden by a novel filtration approach that does not make use of physical membranes (exclusion methods).

Inertial microfluidics has been demonstrated in recent years as an alternative filtration method to membrane- and centrifugation-based filtration methods [2, 3, 142, 212]. Among various label-free and passive cell/particle sorting techniques that are suitable at micron scale, inertial focusing can potentially be scaled up comparatively easily as its mechanism is based solely on hydrodynamic forces. This feature is particularly advantageous when processing biological products at scale of liters per minute. While Dean-coupled inertial focusing involves curved channels in general, the spiral structure in particular has been widely used to separate particles and cells based on their sizes [43-45, 50, 96, 129, 134, 146]. In addition, trapezoidal spiral channels outperform rectangular spiral channels when processing samples with high concentrations ($\sim 10^6$ cells/mL) as it exhibits greater separation resolution [48, 49].

This work demonstrates separation of particulates from mesenchymal stem cells (MSC) suspensions; cell therapies using MSCs make up a large portion of clinical trials compared to other cell types [155, 156, 218]. MSC therapies are being trialed for several diseases such as cardiovascular, autoimmune and gastrointestinal diseases [155]; more than 500 MSC-related clinical trials are registered on NIH clinical trials database as of April 2016 [219]. One of the major challenges in removing particulates from MSCs using inertial microfluidics is that MSCs have a wide cell size distribution ranging from 10 to 30 μm [220]. To validate the feasibility of using spiral inertial microfluidics to remove particulates from cultured cells, a series of spiral channels were first characterized experimentally, and then a high-

throughput channel was implemented to filter particulates between 25 μm to 75 μm . This removes particulates larger than the average MSC size of 20 μm .

6.2 Material and methods

6.2.1 Microchannel design and fabrication

A series of trapezoidal spirals were fabricated (Figure 6-1) to focus particles ranging from 25 μm to 75 μm near the inner wall (IW) and smaller cells at the outer wall (OW). To avoid clogging and defocusing, the lowest channel height (H) of the IW is approximately 160 μm . The corresponding largest particle clogging ratio ($K=a/H_{min}$) is 0.47 and must be kept below $K=0.5$. The channel width (W) varied from 800 μm to 1600 μm that corresponds to channel aspect ratio ($AR=W/H_{min}$) of 5 to 10. A moderate slope of slanted wall ($\tan(\alpha)=(H_{OW}-H_{IW})/W\approx 0.08 < 0.1$) was used for size-based separation [49, 212]. The spiral device has eight loops with innermost radius of 7.5 mm and pitch of $1.75\times W$. Standard soft lithography technique was used to fabricate microchannels in polydimethylsiloxane polymer (PDMS, Sylgard 184 Silicone Elastomer Kit, Dow Corning) with curing agent at 10:1 ratio. An Aluminum master mold was made by micro-milling (Whits Technologies, Singapore). A semi-cured PDMS channel replica was bonded to another semi-cured thick PDMS layer to form a channel [212].

6.2.2 Cell culture and biological assays

Human mesenchymal stem cells (hMSCs) derived from bone marrow (Lonza Singapore) were used at passage 10. The cells were cultured on T175 tissue culture flasks in D10 medium. D10 medium was made up with high-glucose Dulbecco's modified Eagle's medium (DMEM, Life Technologies Holdings Pte Ltd, Singapore), and supplemented with 10% v/v fetal bovine serum (FBS, Life Technologies Holdings Pte Ltd., Singapore) and 1% v/v Penicillin-Streptomycin (10,000 U/mL, Life Technologies Holdings Pte Ltd). Details and specific condition

of the monolayer cell culture and reagents used have been previously presented in Chapter 4.

Trilineage differentiation assay was performed to test the multipotency of the filtrated hMSCs. Cells were differentiated for 28 days into the three lineages and stained with the lineage-specific stains. hMSCs were positively stained by (i) Oil Red O (ii) Alcian Blue (iii) Alizarin Red S to indicate differentiation into adipocytes, chondrocytes and osteocytes respectively. Details of the trilineage differentiation test have previously been presented in Chapter 4.

To characterize the cells, phenotypic analysis of surface marker expression was determined by flow cytometry. Harvested cells were resuspended in cold flow cytometry buffer which is made up PBS supplemented with 1% v/v Bovine Serum Albumin (Sigma Aldrich, USA). Cell count was performed using Nucleocounter (Nucleocounter NC-250, Chemometec, Denmark). Final cell concentration of 10^6 cells/mL was used. 100 μ L ($N=10^5$ cells) of the cell suspension was transferred into 96-well v-bottom plate (Thermo Scientific, USA) and then stained with (i) 1 μ L anti-human CD34 conjugated with Alexa Fluor 647 (Biolegend, USA), (ii) 1 μ L anti-human CD90 conjugated with FITC (Biolegend, USA), (iii) 1 μ L anti-human CD45 conjugated with Alexa Fluor 647 (Biolegend, USA), (iv) 1 μ L anti-human CD105 conjugated with FITC and (v) 1 μ L anti-human CD73 conjugated with Alexa Fluor 647 (Biolegend, USA), separately. The plate was covered with aluminum foil and incubated for 30 minutes on ice. Thereafter, the plate was centrifuged at 2800 rpm for 3 minutes. The cell pellets were resuspended with 200 μ L of cold flow cytometry buffer and analyzed using flow cytometry (Novocyte, ACEA Biosciences Inc, USA).

6.2.3 Experimental setup and sample preparation

To characterize the experimental spiral channel designs, fluorescent polystyrene microparticles were used to observe the inertial focusing effect. 10 μ m to 30 μ m

fluorescent particles were resuspended in DI water at concentration of $\sim 10^4$ particles/mL. Concentration of 43 μm and 75 μm particles were $\sim 10^3$ particles/mL (FITC-fluorescent 10 μm , 20 μm and 43 μm beads, Polysciences, Inc. USA; Orange-fluorescent 30 μm beads Phosphorex, Inc. USA; and 75 μm polystyrene particle, SpheroTech, Inc. USA). A syringe pump (Chemyx, F200, USA) along with 10 mL BD plastic syringes were used to feed the particle/cell samples into channels. 50 fluorescent images were averaged to identify the fluorescence particle streaks using 100-200 ms exposure time (16-bit CMOS camera, optiMOS, QImaging). For experiments involving cells, the spiral channels were first sterilized with 70% ethanol, followed by washing with sterile PBS.

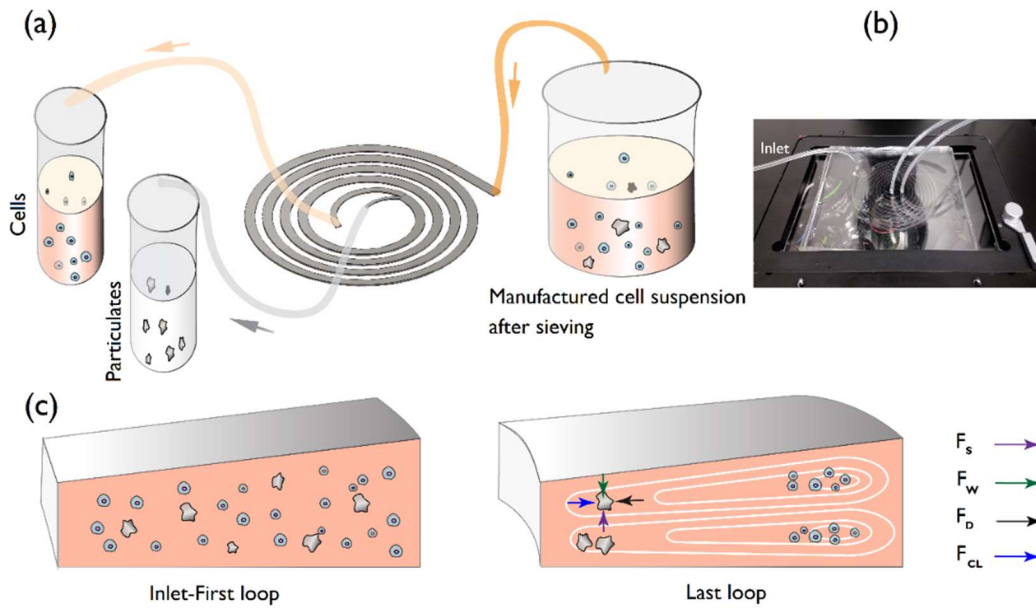


Figure 6-1 (a) Schematic diagram illustrates removal of particulates from manufactured cell suspensions using inertial microfluidics. (b) The optical picture of fabricated trapezoidal spiral channel with large AR=10 mounted on the fluorescence microscope. (c) The relatively smaller cells are trapped at vortex cores while the larger particles equilibrate near the inner wall (IW) due to the interplay between shear-gradient lift force (F_s), wall-effect lift force (F_{CL}), wall-induced lift force (F_w) and secondary drag force (F_D).

6.3 Results and discussion

MSC population is heterogeneous in size (Figure S6-1) and varies from 10 μm to 30 μm with an average of $15.4 \pm 3.5 \mu\text{m}$. The concentration of manufactured stem cell population is high and can approach 10^6 cells/mL [157]. Conversely, the particulates contamination in background cell suspension is very low (~ 100 particles/mL) if good manufacturing practice (GMP) condition is maintained [173]. To achieve a high-throughput trapezoidal spiral, the largest channel hydraulic diameter, D_H , is established. As such, cells are mainly influenced by secondary flow and thus do not experience focusing, but are trapped at Dean vortex cores located at the outer half of channel cross section; the corresponding particle confinement ratio ($C=a/D_H$) is: $0.01 < C < 0.05$ [49]. On the other hand, relatively larger particles (25-75 μm) equilibrate near the inner wall due to the interplay between net inertial lift force and secondary drag force (Figure 6-1) [25, 84, 194].

6.3.1 Particle focusing

Figure 6-2a illustrates the inertial focusing of diverse particle sizes in a trapezoidal spiral with large channel aspect ratio of $AR=10$. The channel hydraulic diameter is 394 μm . Particles with diameters of 10 μm to 20 μm that are surrogate MSCs are mainly dispersed and focused respectively at the outer half of channel cross section at flow rates of greater than 6 mL/min ($Re \sim 109$). Intravenously administered cell therapy products comply with USP<788> Particulate matter in injection [221] which dictates that for large parenteral drug container (>100 mL) the number of 10 μm and 25 μm particles cannot exceed 12 and 2 particles/mL respectively. Therefore, 25 μm was chosen as the threshold particle-size for filtration to determine the appropriate working flow rate. The inertial focusing and the corresponding intensity line scans of the 25 μm particles are shown in Figure 6-2a&b respectively. The focusing close to the IW starts to transition to the OW when the flow rate goes beyond 6 mL/min. Figure 6-2c displays the equilibrium of diverse particle sizes and the separation quality at flow rate of 6 mL/min. Although some 20- μm particles

were still swept back to the IW, the removal of broad range of particles down to 25 μm is of the priority here. Moreover, inertial focusing of larger particle sizes of greater than 30 μm shows that, although the secondary drag force is proportional with particle size ($F_D \sim a$), the movements of large particles lag behind the smaller particles when moving towards the IW. This mainly originates from the wall-effect lift force in a trapezoidal channel that is a power law function of particle size ($F_{CL} \sim a^n$, $n > 1$) [195]. Reducing the channel hydraulic diameter by using lower channel AR=7.5 brings this gap down (See Appendix D, Figure S6-2b). This implies the existence of an upper limit for channel AR. Increased channel height, i.e. reduction of particle clogging ratio, causes further dispersion of smaller 10- μm particles and defocusing of 25- μm particles near IW (Figure S6-3).

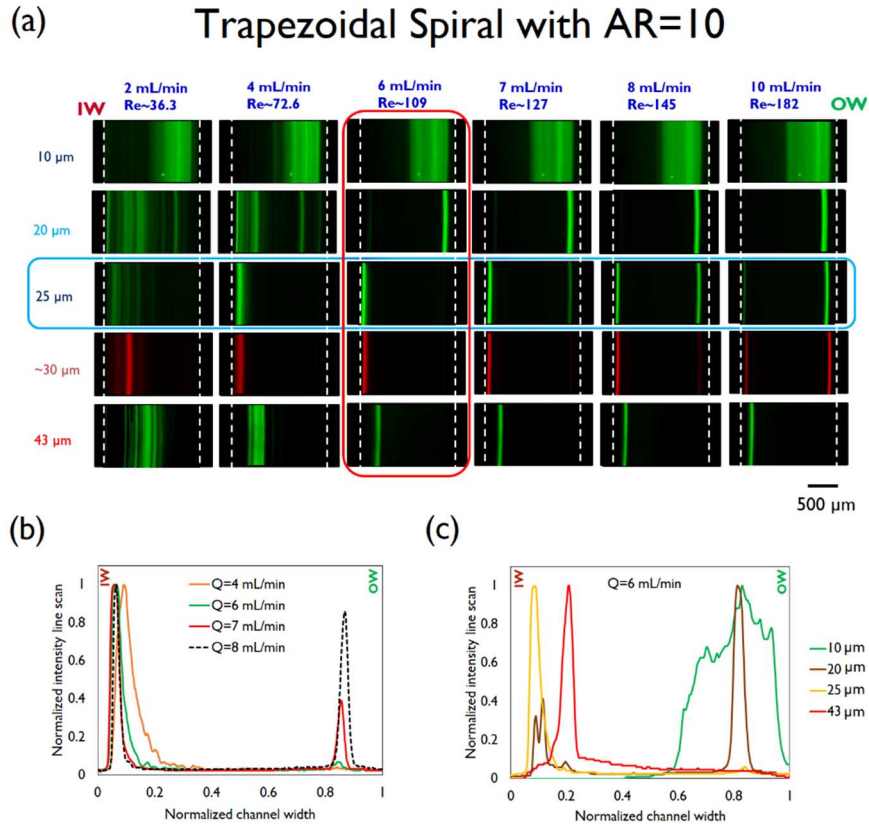


Figure 6-2 (a) Inertial focusing of fluorescent particles in the trapezoidal spiral channels H160-290 μm -W1600 μm and (b) the corresponding intensity line scans for 25- μm particles. It shows that the transition takes place at flow rates higher than 6 mL/min. (c) Intensity line scans of different-sized particles at flow rate of 6 mL/min ($Re \sim 109$).

6.3.2 Removal of particulates using the trapezoidal spiral channel

To quantify performance of the spiral channel, a case model was prepared by spiking bone marrow-derived MSCs suspensions with fluorescent particles of sizes 25 μm ($\sim 10^4$ particles/mL), 30 μm ($\sim 10^3$ particles/mL) and 43 μm ($\sim 10^3$ particles/mL) and polystyrene 75- μm particles ($\sim 10^2$ particles/mL). To evaluate the effect of cell-particle interaction on particle focusing, different cell concentrations are examined. In the absence of cells, particles ($a > 20 \mu\text{m}$) are shown to reach a focusing point near the IW (Figure 6-2a). Figure 6-3a shows that beyond $\sim 0.8 \times 10^6$ cells/mL (at flow rate of 6 mL/min) the interaction between cells and $\sim 30\text{-}\mu\text{m}$ particles causes widening and dispersion of $\sim 30\text{-}\mu\text{m}$ particles. This device achieved 96.4% removal of 30- μm particles from the IW outlet and $\sim 79\%$ MSCs harvesting from the OW outlet at 6 mL/min ($Re \sim 109$) based on measured concentration and collected volumes. Increasing flow rate to 8 mL/min ($Re \sim 145$) enhanced cell harvesting yield to 95% but reduced particle removal efficiency for 30- μm particles to 11.7% at cell concentration of 0.8×10^6 cells/mL as shown in Figure 6-3b. A trade-off exists between the smallest particle cutoff size isolated from the IW and the cell harvesting efficiency. Increasing flow rate to 8 mL/min increased particle cutoff size to greater than 30 μm and cell harvesting efficiency to $\sim 94.5\%$. Figure S6-4 displays inertial focusing of 30- μm and 43- μm fluorescent particles in the presence of MSCs with concentration of 0.8×10^6 cells/mL at flow rate of 8 mL/min. The focusing of 30- μm particles underwent transition between the IW and the OW, but all 43- μm particles are focused and isolated from the IW outlet.

The particle removal efficiency from the IW outlet for different particle sizes is shown in Figure 6-3c using flow rate of 6 mL/min ($Re \sim 109$). Overall, the efficiency for removal of particles from the IW outlet is directly proportional to particle size as evident in the 99% isolation of 43- μm particles compared to 83.4% isolation of 25 μm particles. For the large 75- μm particles with extremely high clogging ratio $K = a/H_{min} \approx 0.47$, the corresponding filtration efficiency dropped to 95.42% due to lagging and distant equilibrium position from the IW. The viability of sorted MSCs

compared to the control sample decreased by 5% ($n=3$) and remained at 90% with trypan blue assay (Figure 6-3d). The collected samples from the IW and OW outlet as displayed in Figure 6-3e show removal of a broad range of particle sizes from 25 to 75 μm via the IW outlet. Given that the efficiency of cell harvesting is highly dependent on target cell size, due to heterogeneity of MSC population, some MSCs equal or greater than cut-off size ($\geq 25 \mu\text{m}$) are lost through IW outlet. For MSCs whose sizes range between 20 to 25 μm , recycling the sample at the IW outlet could enhance the total yield [212]. Moreover, fractionating MSCs population based on cell size to harvest smaller MSCs is of interest in cell-based therapeutic products. The suspended MSC size was disclosed recently as a biophysical marker that is required but not sufficient for identifying multipotent adult MSCs. Small-sized hMSCs subpopulations ($a < 20 \mu\text{m}$) possess higher degree of stemness or multipotency compared to that of the larger size hMSCs subpopulation showing only unipotency [222]. MSCs subpopulation of larger sizes has also been shown to correlate directly with higher levels of senescence [220]. Hence this device is essentially versatile; it can not only be used to remove particulates contamination but also fractionate MSC subpopulations simultaneously to achieve higher efficacy in MSC-based cell therapy.

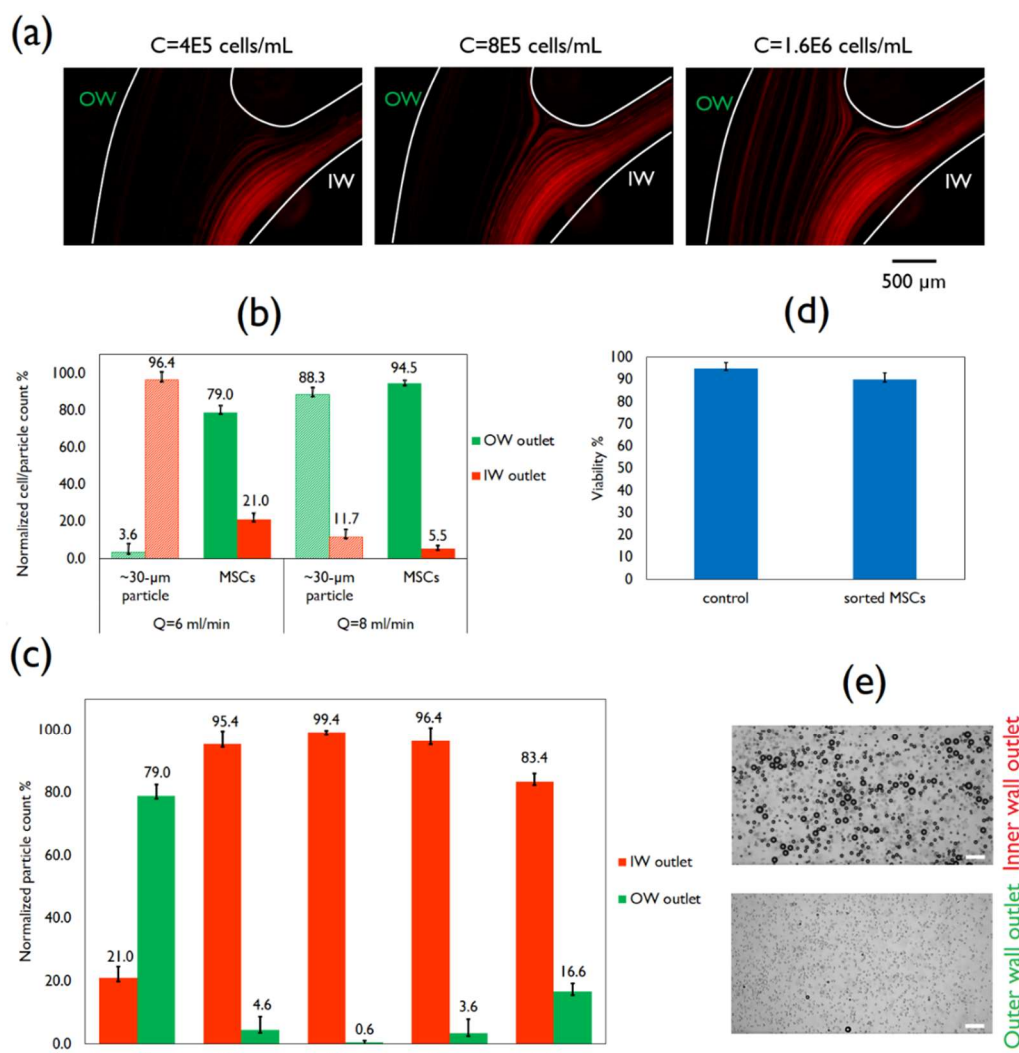


Figure 6-3 (a) Inertial focusing of $\sim 30\text{-}\mu\text{m}$ fluorescent particles in the presence of MSCs for various concentrations at flow rate of 6 mL/min ($Re \sim 109$). It shows the effect of cell-particle interactions on inertial focusing. Separation performance of the spiral channel using 0.8×10^6 MSCs/mL spiked with (b) $\sim 30\text{-}\mu\text{m}$ particles at two different flow rates of 6 and 8 mL/min and (c) various particle sizes at flow rate of 6 mL/min . (d) viability of MSCs before and after sorting and (e) the corresponding collected samples from the IW and OW outlet using the trapezoidal spiral channel at flow rate of 6 mL/min ($Re \sim 109$).

6.3.3 Validation of harvested MSCs

MSCs harvested by means of spiral inertial microfluidics were subsequently cultured in vitro. Cultured MSCs exhibit the spindle-like morphology at day 3 and proliferation rates were comparable to that of the control qualitatively (Figure 6-4a). Multipotency testing (trilineage differentiation) was done after monolayer culture of harvested hMSCs, using protocols described in 4.3.5.2. Lipid vacuoles from adipocytes stained by Oil Red O, glycosaminoglycan from chondrocytes complexed with Alcian Blue and mineralized matrix from osteocytes stained by Alizarin Red S. Positively stained cells indicated successful differentiation into the respective lineages (Figure 6-4b).

Immunophenotyping flow cytometry was also performed to validate MSCs. High percentages of sorted cells presenting CD73, CD90 and CD105 and not CD34 and CD45 shown in Figure 6-4c indicates that the sorted cells retained their MSC characteristics [204] compared to the control sample without sorting, using the spiral inertial microfluidics (Figure S6-5). These results strongly suggest that the cell harvesting process by means of the trapezoidal spiral did not alter the MSC properties.

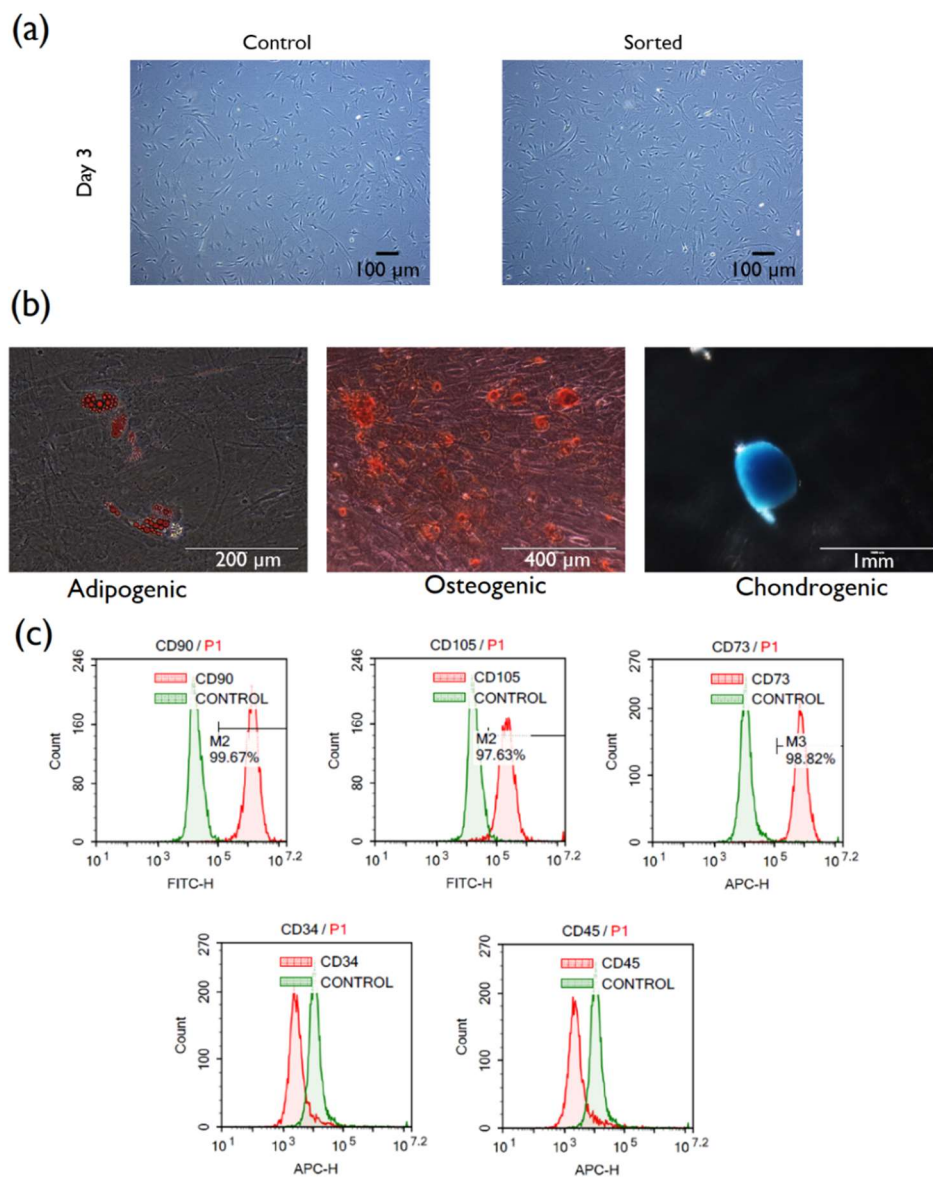


Figure 6-4 (a) Monolayer culture of MSCs after harvesting using the trapezoidal spiral channel and control sample at day 3. (b) Demonstration of trilineage differentiation of harvested MSCs to adipogenic, osteogenic and chondrogenic lineages. (c) Immunophenotype of harvested MSCs using the trapezoidal spiral; it shows the positive expression for CD90, CD105 and CD73.

6.4 Summary

A high-throughput method using trapezoidal spiral inertial microfluidics (6 mL/min, $Re \approx 109$) is demonstrated to remove subvisible particulates ($25 \mu\text{m} < a \leq 75 \mu\text{m}$) from manufactured cell products with efficiency of greater than $\approx 95\%$ at downstream. The developed spiral channel fractionates simultaneously mesenchymal stem cell populations and harvest the small- to medium-sized subpopulations with yield of 80 %.

Chapter 7 Conclusions and Future Work

7.1 Conclusions

This thesis investigates the fundamental characteristics of inertial fluidics in straight and trapezoidal channels for scale up applications in manufactured cell products and uses Dean-coupled inertial focusing principles to design a device that can clarify cell suspensions at high throughput. These proof-of-concept devices can harvest MSCs from a suspension spiked with microcarriers and particulates at a throughput of ~ 30 mL/min and 6 mL/min, respectively. Further investigations show that the harvested cells remain highly viable and retain multipotency. Some main parameters affect inertial focusing in scaled-up channels are (i) significant variation in curvature ratio (ii) broader particle size distributions, i.e., larger coefficient of variation ($CV > 5\%$) and (iii) emerging impact of particle weight.

7.1.1 Inertial focusing in trapezoidal straight channels

To better comprehend the inertial lift force solely in the absence of Dean flow, the inertial particle focusing dynamics in trapezoidal straight microchannels is investigated first for a broad range of channel Reynolds number ($20 < Re < 800$) and various slopes of slanted walls. Increasing the aspect ratio (AR) from 2 to 4 enhances the off-center lateral focusing position from the middle of channel cross-section, up to ~ 20 percent of the channel width. A size-dependent lateral focusing position first shifted toward the longer side wall and then moved back toward the shorter side wall when Re is progressively increased ($Re > 50$). The focusing point is spoiled near the slanted wall due to the dissymmetry; the focusing is mainly developed near the bottom wall or fluctuates between the channel center and the bottom wall, depending on the slanted wall and Re ($Re < 100$, channel aspect ratio 4:1). Remarkably, an almost complete shift in major focusing from the longer side wall to the shorter side wall is found for the large particle clogging ratio of $K \sim 0.9$ ($K = a/H_{min}$) when Re increases noticeably to ~ 650 . Eventually, the trapezoidal

straight channel ($AR \sim 4$ and $\tan(\alpha) \approx 0.45$) along with a bifurcation is used for continuous filtration of a broad range of particle size ($0.3 < K < 1$) exiting through the longer wall outlet with an efficiency of $\sim 99\%$ ($Re < 100$). Finally, filtration of large-sized particles with $K \sim 0.9$ through the shorter wall outlet is shown at extremely high $Re \sim 1100$ with $\sim 82\%$ efficiency and ~ 2.5 -fold concentration.

7.1.2 Inertial-based filtration method for removal of microcarriers from mesenchymal stem cell suspensions

A scaled-up trapezoidal spiral channel (at millimeter dimensions) is developed that removes microcarriers from cell suspensions. A series of trapezoidal and rectangular spirals are investigated. All channels possess minimum height of 0.5 mm, i.e. particle clogging ratio of $K \approx 0.35$, since any smaller channel height increases the potential of clogging of the channel. It is found that elevating the average channel height by 0.2 mm, while reducing the average particle clogging ratio ($K = a/H$) from 0.26 to 0.20, caused MC partial focusing only at a noticeably low Re number of ~ 56 though there is no theoretical constraint yet reported. A trapezoidal spiral with ultra-low-slope ($\tan(\alpha) = 0.0375$) develop MC focusing near the inner wall at high Re numbers ranging from ~ 300 to ~ 400 . This contributes to a high-throughput device while maintaining high MC filtration efficiency ($E \approx 99\%$) as a crucial trait. The present channel is implemented to remove MCs from hMSC suspension at ~ 30 mL/min ($Re \approx 326.5$) with total yield of $\sim 94\%$ after two passes. Overall cell viability is maintained at $95.3 \pm 1.15\%$ ($n=3$) and $93.16 \pm 2\%$ ($n=3$) after the first and the second pass, respectively. Harvested cells demonstrate all potential trilineage differentiations and morphology as expected.

7.1.3 Scaled-up inertial microfluidics: Retention system for microcarrier-based suspension cultures

In this study, the impacts of scaling up channels on Dean flow and subsequent particle focusing in spiral channels with rectangular and trapezoidal cross-sections are investigated in detail. A “focusing map” is established that can be used as a

foundation for design of new microfluidic systems. Unlike the micron scale, the minimum particle confinement ratio ($C=a/D_H$) required is found $C \geq 0.2$ and $C \geq 0.17$ for rectangular and trapezoidal channels respectively, showing notably stringent limitation on C ratio (the minimum C reported for micron-scale particle is greater than 0.07). Scaling up the channel hydraulic diameter by one order of magnitude from ~ 0.1 mm (micron scale) to ~ 1 mm (millimeter scale) quenches the inertia of flow for a given channel Re number ($Re \leq 500$), as a result existence of Dean-coupled inertial focusing is deteriorated ($D_H > \sim 1$ mm).

In addition, a unique focusing based on an inflection point without the aid of sheath flow is explored in the scaled-up trapezoidal channel with large slant ($\tan(\alpha)=0.2$, $D_H \approx 1$ mm). Accordingly, a single-loop trapezoidal spiral is proposed for particle filtration or concentration. Investigation of particle volume fraction demonstrated that the capacity of conventional focusing adjacent to the outer wall in trapezoidal spirals is limited to dilute suspensions with low particle volume fraction ($V_f < 0.42\%$). Regardless, the single-loop trapezoidal spiral with a considerably smaller footprint and higher throughput ($Re \geq 200$) shows remarkable performance, based on inflection point focusing, even at relatively high particle volume fractions ($V_f \sim 3.4\%$) and a broad range of particle clogging ratio ($0.086 < K < 1$). The utility of this device as a high-throughput and continuous retention system for cell-microcarrier suspension culture is showcased. Biological validation assays show that the growth rate as well as the identity of MSCs in culture were unaffected and were comparable to that of conventional spinner flask culture.

7.1.4 Separation of particulates matter contamination from manufactured cell products by inertial microfluidics

Inertial microfluidics is also demonstrated for removal of particulates from manufactured cell products. A high-throughput spiral inertial (6 mL/min, $Re \approx 109$) is established for separation of a broad range of particle size ($25 \mu\text{m} < a \leq 75 \mu\text{m}$) with efficiency of greater than $\approx 95\%$. A case model, mesenchymal stem cell (MSC) type was chosen due to its promising clinical results in allogenic cell therapy and broad applications in tissue regenerative applications. Due to the heterogeneity of

in vitro cultured MSCs, a large-sized MSCs subpopulation ($a > 20 \mu\text{m}$) is separated together with contaminant particles. Removal of particulates and fractionation of MSCs population simultaneously is of interest as subpopulations of MSCs are known to exhibit different characteristics based on size. In addition, the developed spiral chip can also be used for enriching particulate matter for further analysis.

7.2 Future Work

Inertial fluidics is at this time, not efficient for suspensions with high particle volume fractions. This needs to be further improved if such devices were to be employed at industry scale. For example, the microcarrier volume fraction used for cell culture is projected to reach $\sim 10\%$ or even higher for scaled-up bioreactors. Inflection point focusing in combination with a new channel cross-sectional shape could develop a curved channel which can handle suspensions of higher particle volume fractions.

Scaling out the designed channels to achieve a relevant volumetric throughput of Liter per minute is of great interest for the biomanufacturing industry. Although scaling out through parallelization and multiplexing channels may seem straightforward, the major focusing phenomenon needs to be evaluated further. Swift switching of size-dependent focusing between inner and outer wall of a trapezoidal spiral decays when using decreasing-Dean mode spirals, as the Dean number progressively decreases when the radius of curvature increases. This is found to play a key role in the loss of high-quality separation resolution and efficiency. However, the increasing Dean mode spiral channel structure has less potential for multiplexing and scaling up throughput.

Moreover, in depth studies of the microcarrier-based cell culture system is necessary in order to apply the scaled-up inertial-based cell-microcarrier retention system for continuous removal of unwanted byproducts such as particulates matter contamination and cell debris from a bioreactor.

Lastly, particulates characterization during cell expansion at the upstream along with enhanced filtration efficiency to deal with higher cell concentrations in bioreactors are ongoing steps that pave the way for adoption of inertial-based filtration methods in bioprocessing in future.

References

- [1] E.K. Sackmann, A.L. Fulton, D.J. Beebe. *Nature*. **2014**, 507, 181-189.
- [2] M.E. Warkiani, A.K.P. Tay, G. Guan, J. Han. *Sci. Rep.* **2015**, 5, 11018.
- [3] M.E. Warkiani, L. Wu, A.K.P. Tay, J. Han. *Annu. Rev. Biomed. Eng.* **2015**, 17, 1-34.
- [4] G. DR, W. WM, M. AJ, H. SC, T. HTK. *Anal. Bioanal. Chem.* **2010**, 397, 3249.
- [5] A. Bhagat, H. Bow, H. Hou, S. Tan, J. Han, C. Lim. *Med Biol Eng Comput.* **2010**, 48, 999-1014.
- [6] N. Pamme, A. Manz. *Analytical chemistry*. **2004**, 76, 7250-7256.
- [7] S.N. Murthy. *Die Pharmazie*. **1999**, 54, 377-379.
- [8] J. Kralj, L. M, S. M, J. K. *Anal. Chem.* **2006**, 78, 5019–5025.
- [9] J. Zhu, T. T-RJ, X. X. *Electrophoresis*. **2010**, 31, 1382.
- [10] J. Voldman. *Annu. Rev. Biomed. Eng.* **2006**, 8, 425.
- [11] X. Hu, P.H. Bessette, J. Qian, C.D. Meinhart, P.S. Daugherty, H.T. Soh. *Proc. Natl. Acad. Sci.* **2005**, 102, 15757-15761.
- [12] F. Petersson, Å. L, S.-N. AM, L. T. *Anal. Chem.* **2007**, 79, 5117.
- [13] A. Nilsson, F. Petersson, H. Jonsson, T. Laurell. *Lab Chip*. **2004**, 4, 131-135.
- [14] G. Destgeer, K.H. Lee, J.H. Jung, A. Alazzam, H.J. Sung. *Lab Chip*. **2013**, 13, 4210-4216.
- [15] Z. Ma, D.J. Collins, Y. Ai. *Anal. Chem.* **2016**, 88, 5316-5323.
- [16] F. Petersson, A. Nilsson, C. Holm, H. Jonsson, T. Laurell. *Analyst*. **2004**, 129, 938-943.
- [17] T. Laurell, F. Petersson, A. Nilsson. *Chemical Society Reviews*. **2007**, 36, 492-506.
- [18] D.D. Carlo. *Lab Chip*. **2009**, 9, 3038-3046
- [19] H. Tsutsui, C.-M. Ho. *Mechanics research communications*. **2009**, 36, 92-103.
- [20] A. Karimi, S. Yazdi, A.M. Ardekani. *Biomicrofluidics*. **2013**, 7, 021501.
- [21] S. Choi, S. Song, C. Choia, J.-K. Park. *Lab Chip*. **2007**, 7, 1532-1538.
- [22] M. Yamada, M. Nakashima, M. Seki. *Anal. Chem.* **2004**, 76, 5465-5471.
- [23] M. Yamada, M. Seki. *Lab Chip*. **2005**, 5, 1233-1239.

- [24] J.A. Davis, D.W. Inglis, K.J. Morton, D.A. Lawrence, L.R. Huang, S.Y. Chou, J.C. Sturm, R.H. Austin. *Proc. Natl. Acad. Sci.* **2006**, 103, 14779-14784.
- [25] D. Di Carlo, I. D. T. R, T. M. *Proc. Natl. Acad. Sci. USA.* **2007**, 104, 18892-18897.
- [26] J.M. Martel, M. Toner. *Annu. Rev. Biomed. Eng.* **2014**, 16, 371-396.
- [27] H. Amini, W. Lee, D. Di Carlo. *Lab Chip.* **2014**, 14, 2739-2761.
- [28] J. Zhang, S. Yan, G. Alici, N.-T. Nguyen, D. Di Carlo, W. Li. *RSC Advances.* **2014**, 4, 62076-62085.
- [29] J. Zhang, D. Yuan, Q. Zhao, S. Yan, S.-Y. Tang, S.H. Tan, J. Guo, H. Xia, N.-T. Nguyen, W. Li. *Sensors and Actuators B: Chemical.* **2018**, 267, 14-25.
- [30] G. Segré, A. Silberberg. *Nature.* **1961**, 189, 209-210.
- [31] G. Segré, A. Silberberg. *J. Fluid Mech.* **1962**, 14, 136-157.
- [32] A.E. Reece, J. Oakey. *Physics of fluids.* **2016**, 28, 043303.
- [33] A. Bhagat, S. Kuntaegowdanahalli, I. Papautsky. *Lab Chip.* **2008**, 8, 1906-1914
- [34] M. Rafeie, J. Zhang, M. Asadnia, W. Li, M.E. Warkiani. *Lab Chip.* **2016**, 16, 2791-2802.
- [35] S.C. Hur, H.T. Tse, D. Di Carlo. *Lab Chip.* **2010**, 10, 274-280.
- [36] J. Zhou, G. PV, K. S, P. I. *Lab Chip.* **2013**, 13, 1919-1929
- [37] A.A.S. Bhagat, S.S. Kuntaegowdanahalli, I. Papautsky. *Microfluid. Nanofluid.* **2008**, 7, 217-226.
- [38] A. Bhagat, K. S, P. I. *Phys. Fluids.* **2008**, 20, 101702.
- [39] J. Zhou, I. Papautsky. *Lab Chip.* **2013**, 13, 1121-1132
- [40] J. Zhang, W. Li, M. Li, G. Alici, N.-T. Nguyen. *Microfluid. Nanofluid.* **2014**, 17, 305-316.
- [41] Z. Wu, Y. Chen, M. Wang, A.J. Chung. *Lab Chip.* **2016**, 16, 532-542.
- [42] N. Xiang, Z. Ni. *Biomedical microdevices.* **2015**, 17, 110.
- [43] H. HW, W. ME, K. BL, L. ZR, S. RA. *Sci. Rep.* **2013**, 3, 1259.
- [44] M.E. Warkiani, G. Guan, K.B. Luan, W.C. Lee, A.A.S. Bhagat, P. Kant Chaudhuri, D.S.-W. Tan, W.T. Lim, S.C. Lee, P.C.Y. Chen, C.T. Lim, J. Han. *Lab Chip.* **2014**, 14, 128-137.

- [45] M.E. Warkiani, B.L. Khoo, D.S.-W. Tan, A.A.S. Bhagat, W.-T. Lim, Y.S. Yap, S.C. Lee, R.A. Soo, J. Han, C.T. Lim. *Analyst*. **2014**, 139, 3245-3255.
- [46] A. Sarkar, H.W. Hou, A.E. Mahan, J. Han, G. Alter. *Sci Rep*. **2016**, 6, 23589.
- [47] H.W. Hou, R.P. Bhattacharyya, D.T. Hung, J. Han. *Lab Chip*. **2015**, 15, 2297-2307.
- [48] L. Wu, G. Guan, H.W. Hou, A.A.S. Bhagat, J. Han. *Anal. Chem*. **2012**, 84, 9324-9331.
- [49] G. Guan, W. L, B. AA, L. Z, C. PCY. *Sci. Rep*. **2013**, 3, 1495.
- [50] M. EW, G. G, K. BL, L. WC, B. AAS. *Lab Chip*. **2013**, 14, 128.
- [51] A.A.S. Bhagat, H. Bow, H.W. Hou, S.J. Tan, J. Han, C.T. Lim. *Med. Biol. Eng. Comput*. **2010**, 48, 999-1014.
- [52] M.E. Warkiani, C.-P. Lou, H.-B. Liu, H.-Q. Gong. *Biomedical microdevices*. **2012**, 14, 669-677.
- [53] A.A.S. Bhagat, H. Bow, H.W. Hou, S.J. Tan, J. Han, C.T. Lim. *Medical & biological engineering & computing*. **2010**, 48, 999-1014.
- [54] S.C. Hur, A.J. Mach, D. Di Carlo. *Biomicrofluidics*. **2011**, 5, 022206.
- [55] A.A.S. Bhagat, S.S. Kuntaegowdanahalli, N. Kaval, C.J. Seliskar, I. Papautsky. *Biomedical microdevices*. **2010**, 12, 187-195.
- [56] C. Situma, M. Hashimoto, S.A. Soper. *Biomolecular engineering*. **2006**, 23, 213-231.
- [57] L. Wang, P.C. Li. *Analytica chimica acta*. **2011**, 687, 12-27.
- [58] H. Chen, L. Wang, P.C. Li. *Lab on a Chip*. **2008**, 8, 826-829.
- [59] A.P. Sudarsan, V.M. Ugaz. *Lab Chip*. **2006**, 6, 74-82.
- [60] A.P. Sudarsan, V.M. Ugaz. *Proc. Natl. Acad. Sci*. **2006**, 103, 7228-7233.
- [61] J. Zhang, S. Yan, D. Yuan, G. Alici, N.T. Nguyen, M. Ebrahimi Warkiani, W. Li. *Lab Chip*. **2016**, 16, 10-34.
- [62] P. Sajeesh, A.K. Sen. *Microfluidics and nanofluidics*. **2014**, 17, 1-52.
- [63] M. J-P, M. JF. *J. Fluid Mech*. **2004**, 515, 171.
- [64] M. J, G. V, G. É, M. J. *Phys. Fluids*. **2004**, 16, 4192.
- [65] H. Amini, S. E, W. WM, D.C. D. *Proc. Natl. Acad. Sci. USA*. **2012**, 109, 11593-11598.

- [66] S. Rubinow, J. Keller. *J. Fluid Mech.* **1961**, 11, 447.
- [67] K. Hood, S. Lee, M. Roper. *J. Fluid Mech.* **2015**, 765, 452-479.
- [68] M. J, M. J, G. É. *Oil Gas Sci. Technol.* **2004**, 59, 59.
- [69] S. PG. *J. Fluid Mech.* **1965**, 22, 385.
- [70] B. Ho, L. Leal. *J. Fluid Mech.* **1974**, 65, 365.
- [71] P. Vasseur, R. Cox. *J. Fluid Mech.* **1976**, 78, 385.
- [72] E. Asmolov. *J. Fluid Mech.* **1999**, 381, 63.
- [73] L. Zeng, N. F, B. S, F. P. *Phys. Fluids.* **2009**, 21, 033302.
- [74] H. Lee, S. Balachandar. *J. Fluid Mech.* **2010**, 657, 89-125.
- [75] D. Di Carlo, E. J, H. K, S. H, T. M. *Phys. Rev. Lett.* **2009**, 102, 094503.
- [76] K. Hood, S. Kahkeshani, D. Di Carlo, M. Roper. *Lab Chip.* **2016**, 16, 2840-2850.
- [77] J. Feng, H.H. Hu, D.D. Joseph. *Journal of fluid mechanics.* **1994**, 277, 271-301.
- [78] F. J, H. H, J. D. *J. Fluid Mech.* **1994**, 277, 271.
- [79] C. Liu, G. Hu, X. Jiang, J. Sun. *Lab Chip.* **2015**, 15, 1168-1177.
- [80] C. Liu, C. Xue, J. Sun, G. Hu. *Lab Chip.* **2016**, 16, 884-892.
- [81] S. J, L. M, L. C, Z. Y, L. D. *Lab Chip.* **2012**, 12, 3952.
- [82] J. Zhang, S. Yan, R. Sluyter, W. Li, G. Alici, N.-T. Nguyen. *Sci. Rep.* **2014**, 4, 4527.
- [83] D. WR. *Proc. R. Soc. A Math. Phys. Eng. Sci.* **1928**, 121, 402.
- [84] M. JM, T. M. *Sci. Rep.* **2013**, 3, 3340.
- [85] V. HJD. *J. Fluid Mech.* **1981**, 107, 423.
- [86] B. S, T. L, Y. L. *Annu. Rev. Fluid Mech.* **1983**, 15, 461.
- [87] D.C. D, E. J, I. D, T. R, T. M. *Anal. Chem.* **2008**, 80, 2204.
- [88] R. A, G. A, N. S, C. D, E. J, T. M. *New J. Phys.* **2009**, 11, 075025.
- [89] O. S, H. R, S. D, O. K. *Chem. Eng. J.* **2004**, 101, 171.
- [90] H. SC, H.-M. NK, M. ERB, D.C. D. *Lab Chip.* **2011**, 11, 912.
- [91] H.W. Hou, A.A. Bhagat, A.G. Chong, P. Mao, K.S. Tan, J. Han, C.T. Lim. *Lab Chip.* **2010**, 10, 2605-2613.
- [92] J. Nam, H. Lim, D. Kim, H. Jung, S. Shin. *Lab Chip.* **2012**, 12, 1347-1354.

- [93] M. M, S. E, A. H, M. W, C. K. *Phys. Rev. X*. **2012**, 2, 031017.
- [94] M. Li, H.E. Muñoz, K. Goda, D. Di Carlo. *Sci. Rep.* **2017**, 7, 10802.
- [95] *Applied Physics Letters*. **2011**, 99, 044101.
- [96] M.E. Warkiani, B.L. Khoo, L. Wu, A.K.P. Tay, A.A.S. Bhagat, J. Han, C.T. Lim. *Nat. Protocols*. **2016**, 11, 134-148.
- [97] B. Chun, A.J.C. Ladd. *Physics of Fluids*. **2006**, 18, 031704.
- [98] C. Y-S, S. K-W, L. S-J. *Lab Chip*. **2011**, 11, 460.
- [99] J. Zhou, P.V. Giridhar, S. Kasper, I. Papautsky. *Biomicrofluidics*. **2014**, 8, 044112.
- [100] X. Wang, C. Liedert, R. Liedert, I. Papautsky. *Lab Chip*. **2016**, 16, 1821-1830.
- [101] X. Wang, M. Zandi, C.-C. Ho, N. Kaval, I. Papautsky. *Lab Chip*. **2015**, 15, 1812-1821.
- [102] J. Kim, J. Lee, C. Wu, S. Nam, D. Di Carlo, W. Lee. *Lab Chip*. **2016**, 16, 992-1001.
- [103] J.-a. Kim, J.-R. Lee, T.-J. Je, E.-c. Jeon, W. Lee. *Anal. Chem.* **2018**, 90, 1827-1835.
- [104] A. Mach, D. Di Carlo. *Biotechnol. Bioeng.* **2010**, 107, 302.
- [105] M. AJ, K. JH, A. A, H. SC, D.C. D. *Lab Chip*. **2011**, 11, 2827.
- [106] H. SC, M. AJ, D.C. D. *Biomicrofluidics*. **2011**, 5, 022206.
- [107] S. E, G. DE, C. J, G. DR, O.B. S. *Lab Chip*. **2014**, 14, 63.
- [108] W. X, Z. J, P. I. *Biomicrofluidics*. **2013**, 7, 044119.
- [109] X. Wang, I. Papautsky. *Lab Chip*. **2015**, 15, 1350-1359.
- [110] P. JS, J. HI. *Anal. Chem.* **2009**, 81, 8280.
- [111] T.S. Sim, K. Kwon, J.C. Park, J.G. Lee, H.I. Jung. *Lab Chip*. **2011**, 11, 93-99.
- [112] M.G. Lee, S. Choi, J.-K. Park. *Journal of Chromatography A*. **2011**, 1218, 4138-4143.
- [113] M.G. Lee, J.H. Shin, C.Y. Bae, S. Choi, J.-K. Park. *Anal. Chem.* **2013**, 85, 6213-6218.
- [114] J.-S. Park, S.-H. Song, H.-I. Jung. *Lab on a Chip*. **2009**, 9, 939-948.
- [115] D. Lee, S.M. Nam, J.-a. Kim, D. Di Carlo, W. Lee. *Anal. Chem.* **2018**, 90, 2902-2911.

- [116] B.R. Mutlu, J.F. Edd, M. Toner. *Proc. Natl. Acad. Sci.* **2018**, 115, 7682-7687.
- [117] J. Zhou, C. Tu, Y. Liang, B. Huang, Y. Fang, X. Liang, I. Papautsky, X. Ye. *Sci. Rep.* **2018**, 8, 9411.
- [118] F. Jiang, K. Drese, S. Hardt, M. Küpper, F. Schönfeld. *AIChE journal.* **2004**, 50, 2297-2305.
- [119] J.P.B. Howell, D.R. Mott, J.P. Golden, F.S. Ligler. *Lab Chip.* **2004**, 4, 663-669.
- [120] S. Ookawara, D. Street, K. Ogawa. *Chemical Engineering Science.* **2006**, 61, 3714-3724.
- [121] I. Gregoratto, C.J. McNeil, M.W. Reeks, Micro-devices for rapid continuous separation of suspensions for use in micro-total-analysis-systems (μ TAS), in: MOEMS-MEMS 2007 Micro and Nanofabrication, SPIE, 2007, pp. 8.
- [122] G. DR, C. DD. *Anal. Chem.* **2009**, 81, 8459.
- [123] S. J, L. M, K. A. *Appl. Phys. Lett.* **2007**, 91, 033901.
- [124] J. Seo, M.H. Lean, A. Kole. *Journal of Chromatography A.* **2007**, 1162, 126-131.
- [125] K. SS, B. AAS, K. G, P. I. *Lab Chip.* **2009**, 9, 2973.
- [126] J.M. Martel, M. Toner. *Phys. Fluids.* **2012**, 24, 032001.
- [127] N. Nivedita, I. Papautsky. *Biomicrofluidics.* **2013**, 7, 054101.
- [128] T.H. Kim, H.J. Yoon, P. Stella, S. Nagrath. *Biomicrofluidics.* **2014**, 8, 064117.
- [129] B.L. Khoo, M.E. Warkiani, D.S.-W. Tan, A.A.S. Bhagat, D. Irwin, D.P. Lau, A.S. Lim, K.H. Lim, S.S. Krisna, W.-T. Lim. *PloS one.* **2014**, 9, e99409.
- [130] J. Sun, C. Liu, M. Li, J. Wang, Y. Xianyu, G. Hu, X. Jiang. *Biomicrofluidics.* **2013**, 7, 011802.
- [131] X. N, C. K, S. D, W. S, Y. H, N. Z. *Microfluid. Nanofluid.* **2012**, 14, 89.
- [132] N. Xiang, Z. Shi, W. Tang, D. Huang, X. Zhang, Z. Ni. *RSC Adv.* **2015**, 5, 77264-77273.
- [133] H. Ramachandraiah, S. Ardabili, A.M. Faridi, J. Gantelius, J.M. Kowalewski, G. Mårtensson, A. Russom. *Biomicrofluidics.* **2014**, 8, 034117.
- [134] A. Bhagat, K. SS, K. N, S. CJ, P. I. *Biomed. Microdevices.* **2010**, 12, 187.

- [135] M.E. Warkiani, B.L. Khoo, L. Wu, A.K. Tay, A.A. Bhagat, J. Han, C.T. Lim. *Nat Protoc.* **2016**, 11, 134-148.
- [136] A. Kulasinghe, T.H.P. Tran, T. Blick, K. O'Byrne, E.W. Thompson, M.E. Warkiani, C. Nelson, L. Kenny, C. Punyadeera. *Sci. Rep.* **2017**, 7, 42517.
- [137] W. Marnie, H. Tristan, R. Meysam, N. Vy, Z.-F. Deirdre, E.W. Majid, T. Benjamin. *Advanced Materials Technologies.* **2018**, 3, 1800066.
- [138] M.S. Syed, M. Rafeie, D. Vandamme, M. Asadnia, R. Henderson, R.A. Taylor, M.E. Warkiani. *Bioresour. Technol.* **2018**, 252, 91-99.
- [139] S.S. Nathamgari, B. Dong, F. Zhou, W. Kang, J.P. Giraldo-Vela, T. McGuire, R.L. McNaughton, C. Sun, J.A. Kessler, H.D. Espinosa. *Lab Chip.* **2015**, 15, 4591-4597.
- [140] W.C. Lee, H. Shi, Z. Poon, L.M. Nyan, T. Kaushik, G. Shivashankar, J.K. Chan, C.T. Lim, J. Han, K.J. Van Vliet. *Proceedings of the National Academy of Sciences.* **2014**, 111, E4409-E4418.
- [141] W.C. Lee, A.A.S. Bhagat, S. Huang, K.J. Van Vliet, J. Han, C.T. Lim. *Lab Chip.* **2011**, 11, 1359-1367.
- [142] T. Kwon, H. Prentice, J. De Oliveira, N. Madziva, M.E. Warkiani, J.-F.P. Hamel, J. Han. *Sci. Rep.* **2017**, 7, 6703.
- [143] M. Jimenez, B. Miller, H.L. Bridle. *Chemical Engineering Science.* **2017**, 157, 247-254.
- [144] M. Jimenez, H. Bridle. *Journal of Microbiological Methods.* **2016**, 126, 8-11.
- [145] C. Tesauro, B. Ferrando, X. Ma, M. Jepsen, A. Ivarsen, R. Fröhlich, T. Stevnsner, B. Knudsen, Y. Ho. *RSC Advances.* **2017**, 7, 23735-23741.
- [146] D. Huang, X. Shi, Y. Qian, W. Tang, L. Liu, N. Xiang, Z. Ni. *Analytical Methods.* **2016**, 8, 5940-5948.
- [147] H.W. Hou, C. Petchakup, H.M. Tay, Z.Y. Tam, R. Dalan, D.E.K. Chew, K.H.H. Li, B.O. Boehm. *Sci. Rep.* **2016**, 6, 29410.
- [148] A. Schaap, J. Dumon, J.d. Toonder. *Microfluid. Nanofluid.* **2016**, 20, 125.
- [149] H. Song, J.M. Rosano, Y. Wang, C.J. Garson, B. Prabhakarapandian, K. Pant, G.J. Klarmann, L.M. Alvarez, E. Lai. *Microfluid. Nanofluid.* **2017**, 21, 64.

- [150] N. Xiang, X. Shi, Y. Han, Z. Shi, F. Jiang, Z. Ni. *Anal. Chem.* **2018**, 90, 9515-9522.
- [151] S. Sofela, S. Sahloul, M. Rafeie, T. Kwon, J. Han, M.E. Warkiani, Y.-A. Song. *Lab Chip.* **2018**, 18, 679-687
- [152] L.M. Lee, J. Rosano, Y. Wang, G.J. Klarmann, C.J. Garson, B. Prabhakarapandian, K. Pant, L.M. Alvarez, E. Lai. *Analytical Methods.* **2018**, 10, 713-721.
- [153] J. Son, K. Murphy, R. Samuel, B.K. Gale, D.T. Carrell, J.M. Hotaling. *Analytical Methods.* **2015**, 7, 8041-8047.
- [154] A. Aijaz, M. Li, D. Smith, D. Khong, C. LeBlon, O.S. Fenton, R.M. Olabisi, S. Libutti, J. Tischfield, M.V. Maus, R. Deans, R.N. Barcia, D.G. Anderson, J. Ritz, R. Preti, B. Parekkadan. *Nature Biomedical Engineering.* **2018**, 2, 362-376.
- [155] A. Trounson, C. McDonald. *Cell Stem Cell.* **2015**, 17, 11-22.
- [156] E. Buzhor, L. Leshansky, J. Blumenthal, H. Barash, D. Warshawsky, Y. Mazor, R. Shtrichman. *Regenerative medicine.* **2014**, 9, 649-672.
- [157] A.K.-L. Chen, S. Reuveny, S.K.W. Oh. *Biotechnol. Adv.* **2013**, 31, 1032-1046.
- [158] R. J, A. E, C. A, B. H, O. S. *BioProcess International.* **2012**, 10, 16-22.
- [159] P. J, V. H, L. L, R. J.A. *BioProcess International.* **2013**, 11, 38-46.
- [160] A.M. de Soure, A. Fernandes-Platzgummer, C.L. da Silva, J.M.S. Cabral. *Journal of Biotechnology.* **2016**, 236, 88-109.
- [161] S. Eaker, E. Abraham, J. Allickson, T.A. Brieva, D. Baksh, T.R.J. Heathman, B. Mistry, N. Zhang. *Cytotherapy.* **2017**, 19, 9-18.
- [162] F. Kadir, P. Ives, A. Luitjens, E. van Corven, Production and Purification of Recombinant Proteins, in: A.D.J. Crommelin, D.R. Sindelar, B. Meibohm (Eds.) *Pharmaceutical Biotechnology: Fundamentals and Applications*, Springer New York, New York, NY, 2013, pp. 47-67.
- [163] N. Liu, R. Zang, S.-T. Yang, Y. Li. *Engineering in Life Sciences.* **2014**, 14, 4-15.
- [164] P. Gupta, M.Z. Ismadi, P.J. Verma, A. Fouras, S. Jadhav, J. Bellare, K. Hourigan. *Cytotechnology.* **2016**, 68, 45-59.

- [165] S. Bukofzer, J. Ayres, A. Chavez, M. Devera, J. Miller, D. Ross, J. Shabushnig, S. Vargo, H. Watson, R. Watson. *PDA journal of pharmaceutical science and technology / PDA*. **2015**, 69, 123-139.
- [166] D. Clarke, J. Stanton, D. Powers, O. Karnieli, S. Nahum, E. Abraham, J.-S. Parisse, S. Oh. *Cytotherapy*. **2016**, 18, 1063-1076.
- [167] D.S. Mark Szczypka, Heather Woolls, and Harvey Brandwein. *BioProcess International*. **2014**, 12, 54-64.
- [168] K.C. Keong, U. Yuichiro, K. Asifiqbal, G. Katharina, E. Süleyman, H. Antoine, S.A. C., R. Martha, E. Frank. *J. Tissue Eng. Regener. Med*. **2018**, 12, 1076-1087.
- [169] D. Clarke. *BioProcess Int*. **2013**, 11, 12-17.
- [170] M.W. Johnson. *bioprocess international*. **2014**, 12, 22-28.
- [171] J.D. Vogel, K. Wormuth. *BioProcess International*. **2017**, 15, 16-22.
- [172] D. Clarke, D. Harati, J. Martin, J. Rowley, J. Keller, M. McCaman, M. Carrion, O. Karnieli, R. Maziarz, R. Perry, S. Oh, J. Stanton. *Cytotherapy*. **2012**, 14, 1032-1040.
- [173] S.E. Langille. *PDA journal of pharmaceutical science and technology*. **2013**, 67, 186-200.
- [174] M.A.H. Fernanda Masri, Paul A De Sousa & Nicholas A Willoughby. *Cell Gene Therapy Insights*. **2017**, 3, 447-467.
- [175] D. Clarke. *CELL & GENE THERAPY INSIGHTS*. **2018**, 4, 187-196.
- [176] A. Chung, G. DR, D.C. D. *Small*. **2012**, 9, 685.
- [177] J.F. Edd, D. Di Carlo, K.J. Humphry, S. Koster, D. Irimia, D.A. Weitz, M. Toner. *Lab Chip*. **2008**, 8, 1262-1264.
- [178] J. Oakey, A. R, A. E, D.C. D. *Anal. Chem*. **2010**, 82, 3862.
- [179] E. Majid, G. G, K. BL, L. WC, B. AAS. *Lab Chip*. **2013**, 14, 128.
- [180] J. Feng, H.H. Hu, D.D. Joseph. *J. Fluid Mech*. **1994**, 261, 95-134.
- [181] M.E. Warkiani, C.-P. Lou, H.-Q. Gong. *Journal of Micromechanics and Microengineering*. **2011**, 21, 035002.
- [182] L. Sensebé, M. Gadelorge, S. Fleury-Cappellesso. *Stem Cell Research & Therapy*. **2013**, 4, 66.

- [183] V. Bunpetch, H. Wu, S. Zhang, H. Ouyang. *Stem cells and development*. **2017**, 26, 1662-1673.
- [184] A.S. Simaria, S. Hassan, H. Varadaraju, J. Rowley, K. Warren, P. Vanek, S.S. Farid. *Biotechnol. Bioeng.* **2014**, 111, 69-83.
- [185] S. Hassan, A.S. Simaria, H. Varadaraju, S. Gupta, K. Warren, S.S. Farid. *Regenerative medicine*. **2015**, 10, 591-609.
- [186] S.A. S., H. Sally, V. Hemanthram, R. Jon, W. Kim, V. Philip, F.S. S. *Biotechnol. Bioeng.* **2014**, 111, 69-83.
- [187] V. Jossen, R. Pörtner, S.C. Kaiser, M. Kraume, D. Eibl, R. Eibl. **2014**.
- [188] T. Lawson, D.E. Kehoe, A.C. Schnitzler, P.J. Rapiejko, K.A. Der, K. Philbrick, S. Punreddy, S. Rigby, R. Smith, Q. Feng. *Biochem. Eng. J.* **2017**, 120, 49-62.
- [189] B. Cunha, C. Peixoto, M.M. Silva, M.J.T. Carrondo, M. Serra, P.M. Alves. *Journal of Membrane Science*. **2015**, 478, 117-129.
- [190] A.W. Nienow, Q.A. Rafiq, K. Coopman, C.J. Hewitt. *Biochem. Eng. J.* **2014**, 85, 79-88.
- [191] J.P. Dijkshoorn, M.A.I. Schutyser, R.M. Wagterveld, C.G.P.H. Schroën, R.M. Boom. *Separation and Purification Technology*. **2017**, 173, 86-92.
- [192] B. Miller, M. Jimenez, H. Bridle. *Sci. Rep.* **2016**, 6, 36386.
- [193] Y.S. Choi, K.W. Seo, S.J. Lee. *Lab Chip*. **2011**, 11, 460-465.
- [194] N. Nivedita, P. Ligrani, I. Papautsky. *Sci. Rep.* **2017**, 7, 44072.
- [195] R. Moloudi, S. Oh, C. Yang, M. Ebrahimi Warkiani, M.W. Naing. *Microfluid. Nanofluid.* **2018**, 22, 33.
- [196] N. Pradyot, D.D. P., L.S. M. *ELECTROPHORESIS*. **2010**, 31, 1414-1422.
- [197] T. Nguyen, R. Pei, M. Stojanovic, Q. Lin. *Microfluid. Nanofluid.* **2008**, 6, 479.
- [198] D. Schop, R. van Dijkhuizen-Radersma, E. Borgart, F.W. Janssen, H. Rozemuller, H.J. Prins, J.D. de Bruijn. *J. Tissue Eng. Regen. Med.* **2010**, 4, 131-140.
- [199] A.K.-L. Chen, X. Chen, A.B.H. Choo, S. Reuveny, S.K.W. Oh. *Stem Cell Res.* **2011**, 7, 97-111.

- [200] C.J. Hewitt, K. Lee, A.W. Nienow, R.J. Thomas, M. Smith, C.R. Thomas. *Biotechnol. Lett.* **2011**, 33, 2325.
- [201] Q.A. Rafiq, K.M. Brosnan, K. Coopman, A.W. Nienow, C.J. Hewitt. *Biotechnol. Lett.* **2013**, 35, 1233-1245.
- [202] S. Sart, A. Errachid, Y.J. Schneider, S.N. Agathos. *J. Tissue Eng. Regener. Med.* **2013**, 7, 537-551.
- [203] J. Hupfeld, I.H. Gorr, C. Schwald, N. Beaucamp, K. Wiechmann, K. Kuentzer, R. Huss, B. Rieger, M. Neubauer, H. Wegmeyer. *Biotechnol. Bioeng.* **2014**, 111, 2290-2302.
- [204] M. Dominici, K. Le Blanc, I. Mueller, I. Slaper-Cortenbach, F. Marini, D. Krause, R. Deans, A. Keating, D.J. Prockop, E. Horwitz. *Cytotherapy.* **2006**, 8, 315-317.
- [205] O.K. Lee, T.K. Kuo, W.-M. Chen, K.-D. Lee, S.-L. Hsieh, T.-H. Chen. *Blood.* **2004**, 103, 1669-1675.
- [206] J.L. Ramírez-Zacarias, F. Castro-Muñozledo, W. Kuri-Harcuch. *Histochemistry.* **1992**, 97, 493-497.
- [207] S. Bjornsson. *Analytical Biochemistry.* **1993**, 210, 282-291.
- [208] C.A. Gregory, W. Grady Gunn, A. Peister, D.J. Prockop. *Analytical Biochemistry.* **2004**, 329, 77-84.
- [209] A. Tamura, J. Kobayashi, M. Yamato, T. Okano. *Biomaterials.* **2012**, 33, 3803-3812.
- [210] A. Tamura, J. Kobayashi, M. Yamato, T. Okano. *Acta biomaterialia.* **2012**, 8, 3904-3913.
- [211] J.M. Martel, K.C. Smith, M. Dlamini, K. Pletcher, J. Yang, M. Karabacak, D.A. Haber, R. Kapur, M. Toner. *Sci. Rep.* **2015**, 5, 11300.
- [212] R. Moloudi, S. Oh, C. Yang, K.L. Teo, A.T.-L. Lam, M.E. Warkiani, M.W. Naing. *Sci. Rep.* **2018**, 8, 12481.
- [213] a. H K Moffatt, A. Tsinober. *Annu. Rev. Fluid Mech.* **1992**, 24, 281-312.
- [214] D. Degani, A. Seginer, Y. Levy. *AIAA Journal.* **1990**, 28, 1347-1352.
- [215] D. Lee, S.M. Nam, J.-a. Kim, D. Di Carlo, W. Lee. *Analytical chemistry.* **2018**, 90, 2902-2911.

-
- [216] L. Doessegger, H.-C. Mahler, P. Szczesny, H. Rockstroh, G. Kallmeyer, A. Langenkamp, J. Herrmann, J. Famulare. *Journal of Pharmaceutical Sciences*. **2012**, 101, 2635-2644.
- [217] T. Kwon, R. Yao, J.-F.P. Hamel, J. Han. *Lab Chip*. **2018**, 18, 2826-2837.
- [218] T.R. Heathman, A.W. Nienow, M.J. McCall, K. Coopman, B. Kara, C.J. Hewitt. *Regenerative medicine*. **2015**, 10, 49-64.
- [219] L.-T. Wang, C.-H. Ting, M.-L. Yen, K.-J. Liu, H.-K. Sytwu, K.K. Wu, B.L. Yen. *Journal of Biomedical Science*. **2016**, 23, 76.
- [220] L. Yin, Y. Wu, Z. Yang, C.A. Tee, V. Denslin, Z. Lai, C.T. Lim, E.H. Lee, J. Han. *Lab Chip*. **2018**, 18, 878-889.
- [221] USP788. *Rockville, MD: USP*. **2007**.
- [222] W.C. Lee, H. Shi, Z. Poon, L.M. Nyan, T. Kaushik, G.V. Shivashankar, J.K.Y. Chan, C.T. Lim, J. Han, K.J. Van Vliet. *Proc. Natl. Acad. Sci*. **2014**, 111, 4409-4418.

Appendices

Appendix A. Supplementary Information: inertial particle focusing dynamics in a trapezoidal straight microchannel

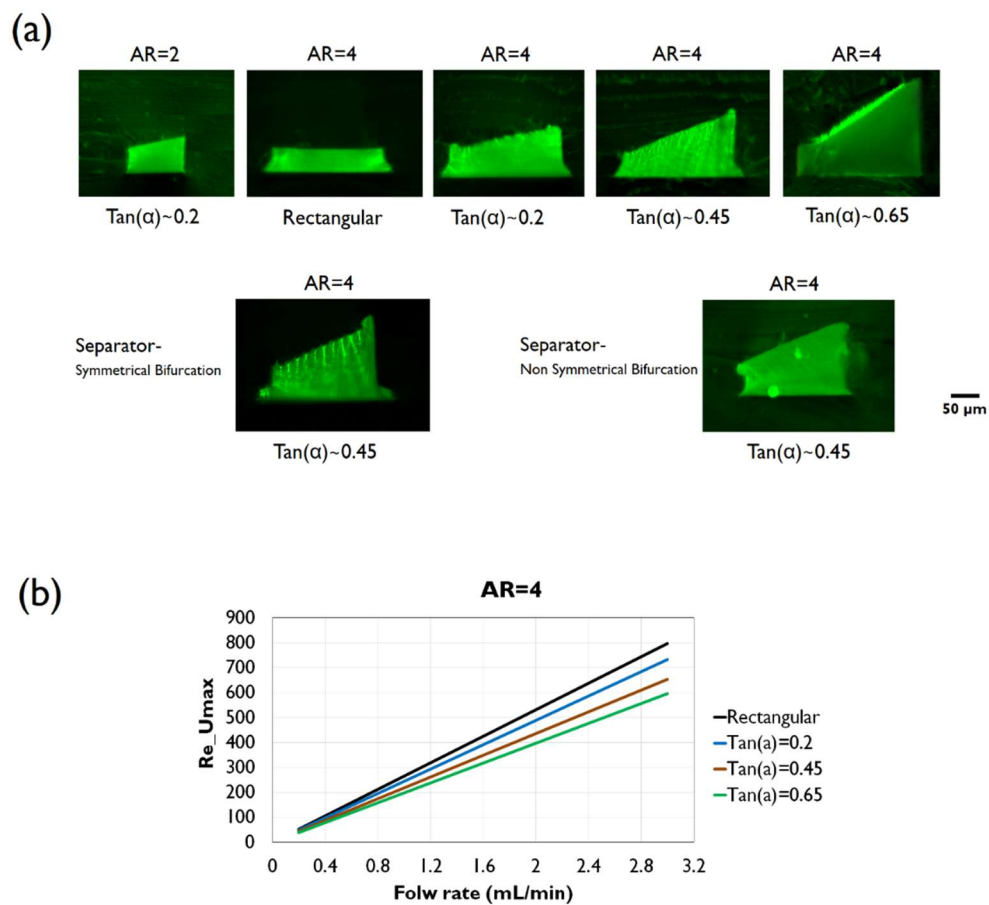


Figure S3-1 (a) The cross-sectional images of channels fabricated. (b) The channel Re number based on maximum velocity ($\sim 2X$ average velocity) versus flow rate for different trapezoid cross-sections studied.

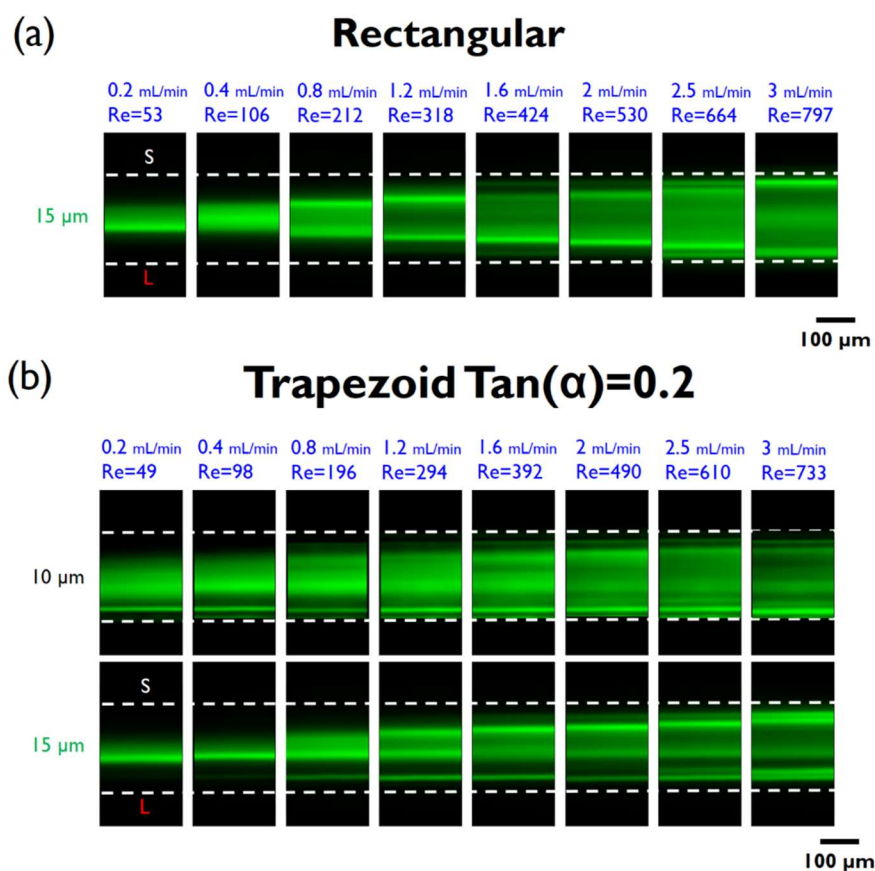


Figure S3-2 Fluorescent images of (a) the rectangular channel for 15- μm particles ($K\sim 0.3$) and (b) the trapezoid with $\text{Tan}(\alpha)=0.2$ for 10- μm particles ($K\sim 0.2$) and 15- μm particles ($K\sim 0.3$).

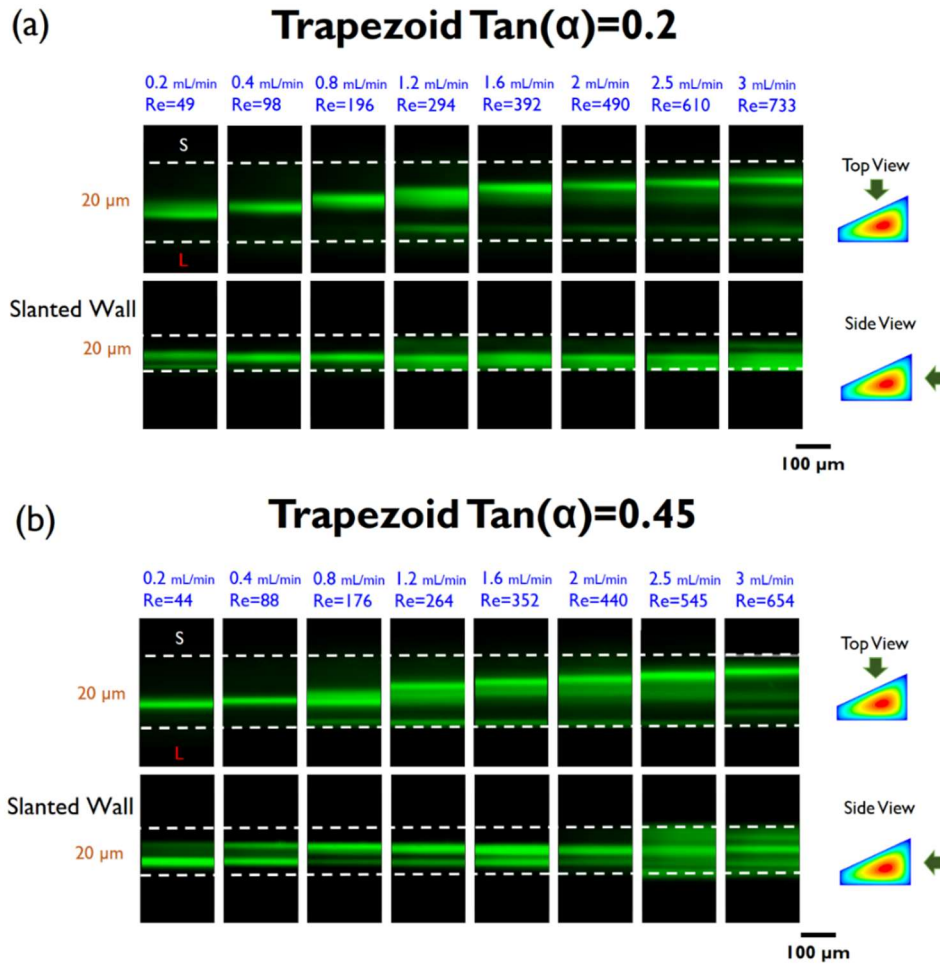


Figure S3-3 Top and side view of focusing of particles with $K \sim 0.4$ (20 μm) in the trapezoid channel (a) $\tan(\alpha)=0.2$ and (b) $\tan(\alpha)=0.45$. It shows that particle focusing near the slanted wall is demolished for $\tan(\alpha)=0.2$ ($Re < 294$) and its fluctuation between center and the bottom wall for the large-slant trapezoid $\tan(\alpha)=0.45$ ($Re < 88$).

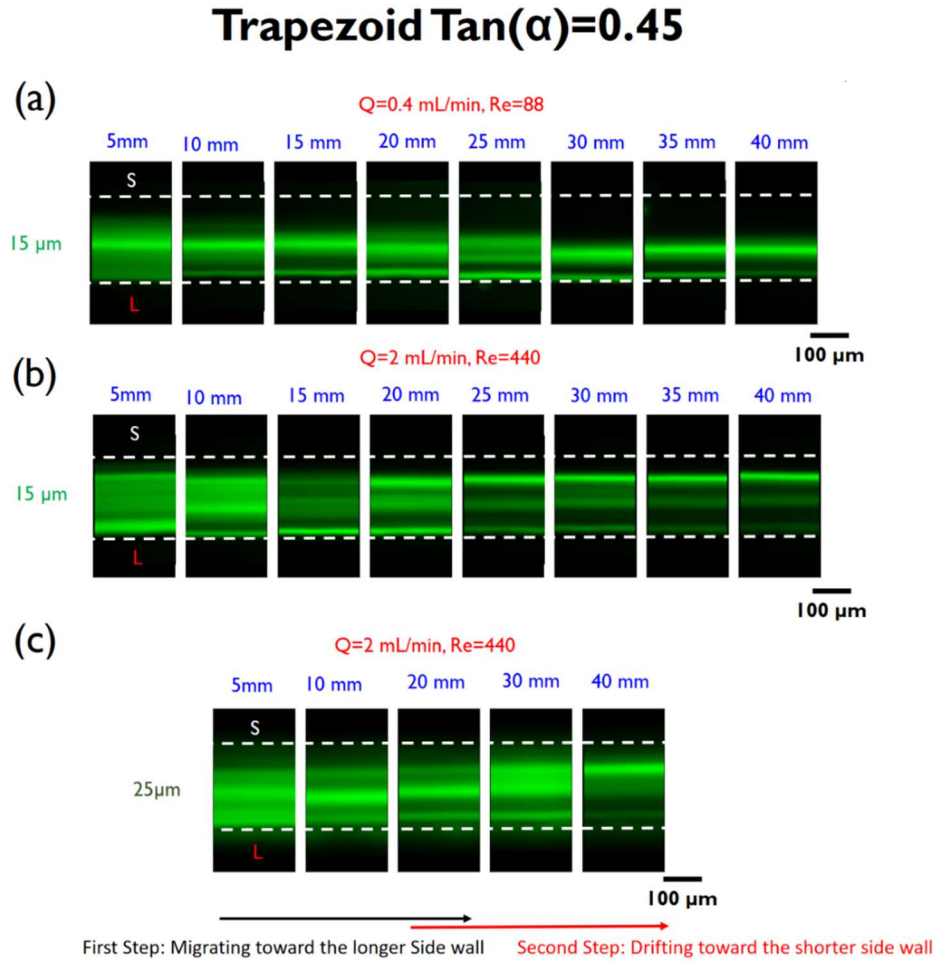


Figure S3-4 Transient lateral focusing of (a-b) 15- μm particles and (c) 25- μm particles. It demonstrates gradual migration of particles toward the longer side wall for low- Re flow ($Re < 100$). For higher Re flow regardless of particle size, it shows that the major lateral focusing shift from the longer side wall to the shorter side wall.

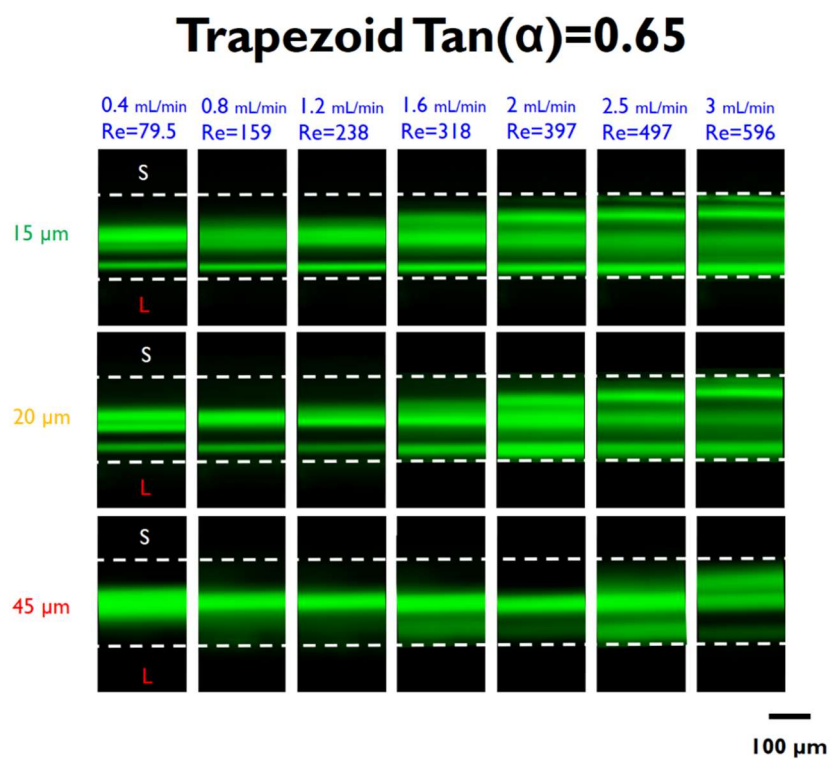


Figure S3-5 Fluorescent images of the lateral focusing in the trapezoid with $\tan(\alpha)\sim 0.65$ for 15- μm particles ($K\sim 0.3$), 20- μm particles ($K\sim 0.4$) and 45- μm particles ($K\sim 0.9$). Generally, it displays a broader particle band width compared to the slanted wall with lower slope.

Appendix B. Supplementary Information: Inertial-based filtration method for removal of microcarriers from mesenchymal stem cell suspensions

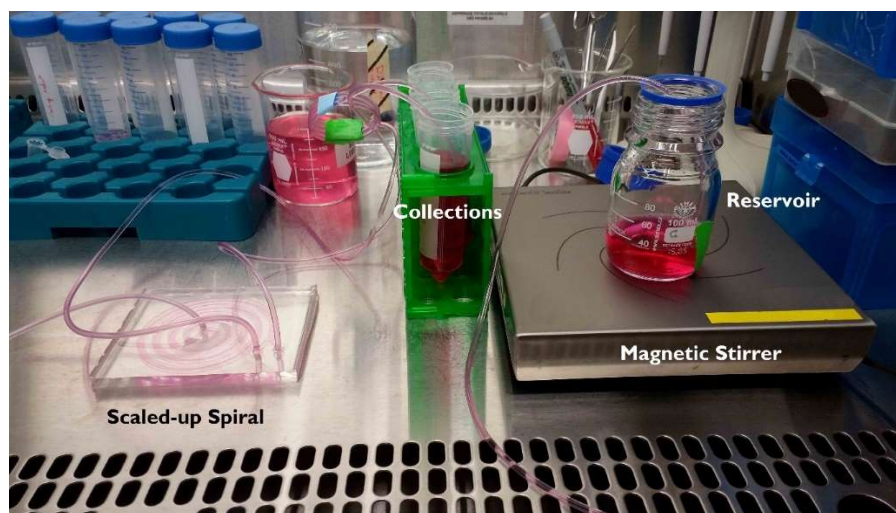


Figure S4-1 Experimental set up for separation of microcarriers from hMSCs

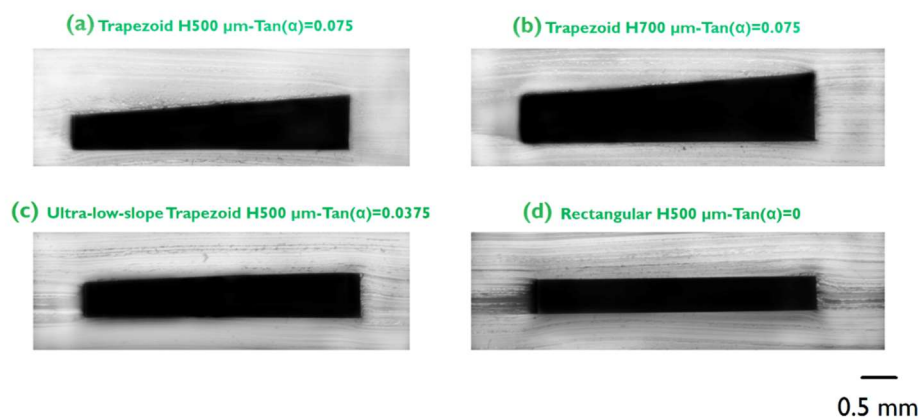


Figure S4-2 The cross-sections of fabricated trapezoid and rectangular spiral channels. All channel's widths are fixed at 4 mm.

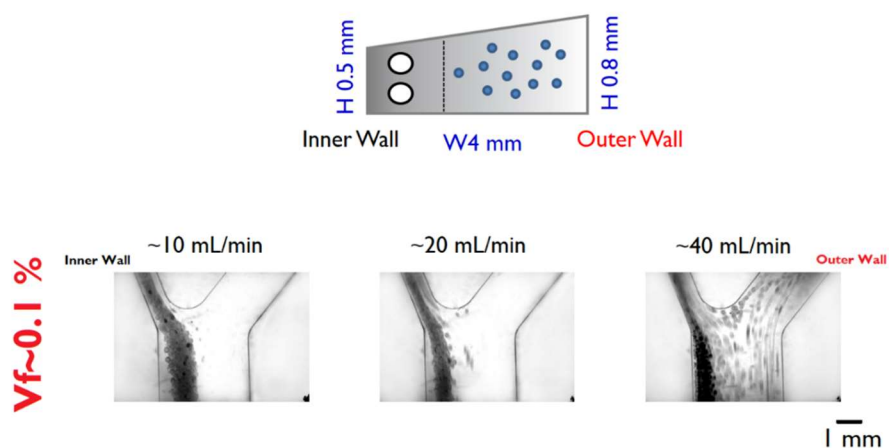


Figure S4-3 Microcarrier focusing dynamics at the bifurcation of trapezoid spiral channel with $H=500\ \mu\text{m}$, $\text{Tan}(\alpha)=0.075$ when the MC volume fraction is as low as $\sim 0.1\%$. It shows good-focusing and separation of MCs from the inner wall outlet at $\sim 20\ \text{mL/min}$.

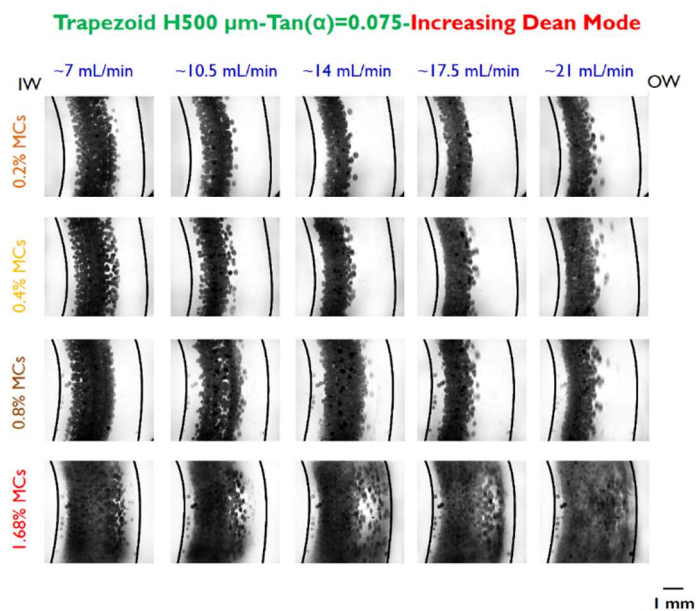


Figure S4-4 Microcarrier focusing dynamics in trapezoid spiral channel with $H=500\ \mu\text{m}$, $\text{Tan}(\alpha)=0.075$ when Dean number increases across the spiral channel.

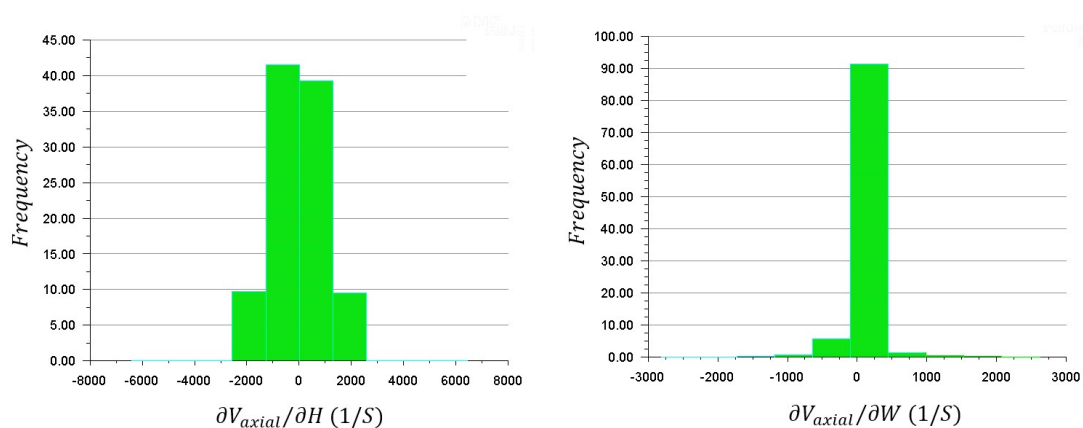


Figure S4-5 Histogram of two major shear rates across the ultra-low-slope trapezoid spiral channel, $H=500\ \mu\text{m}$, $\text{Tan}(\alpha)=0.0375$.

Table S4-1. MC count from the outer wall outlet sample ($n=3$) using the ultra-low-slope trapezoidal spiral

MC volume fraction %	0.2	0.4	0.8	1.6
C_o (MCs/mL) Outer wall outlet	0	7.6 ± 2.5	24.3 ± 4	41.6 ± 7.6
C_s (MCs/mL) Reservoir	~ 750	~ 1500	~ 3000	~ 6000
E %	100	99.4	99.19	99.3

Note: To perform microcarrier (MC) count of the outer wall outlet collection, due to low concentration, 1-mL sample was dispersed into a petri dish and subsequently MCs were counted manually on the microscope stage using bright field.

Appendix C. Supplementary Information: Scaled-up Inertial Microfluidics: Retention System for Microcarrier-based Suspension Cultures

These vortex structures in a spiral channel for laminar flow originates from curvature-induced secondary flow captured by helicity density function. The helicity density is $H_d = U \cdot \omega$ where U is the velocity field and the vorticity is $\omega = \nabla \times U$.

The helicity density can be scaled as follows:

$$H_d = U \cdot \omega \approx U_x \omega_x \quad (S5-1)$$

$$\omega_x = \frac{\partial U_z}{\partial y} - \frac{\partial U_y}{\partial z} \quad (S5-2)$$

where U_x and ω_x are the velocity and vorticity of flow along the channel axis respectively. Figure S1 shows precisely the secondary flow structure for both the rectangular and trapezoid spiral at $De \approx 22$.

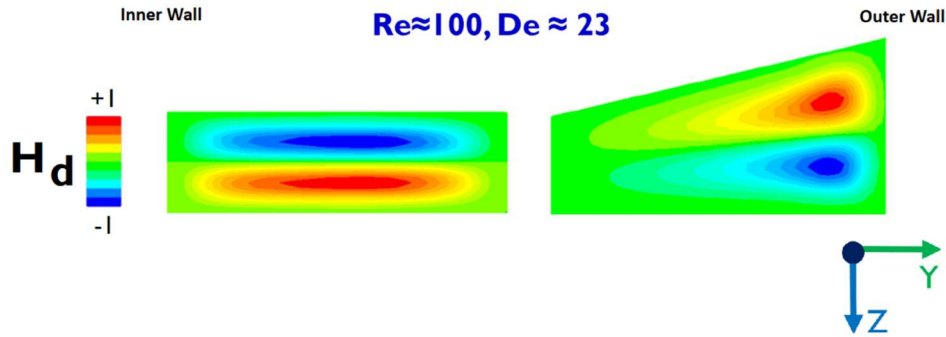


Figure S5-1 Dimensionless helicity density contour shows evolution of Dean vortex structure by transforming the rectangular spiral to the trapezoid.

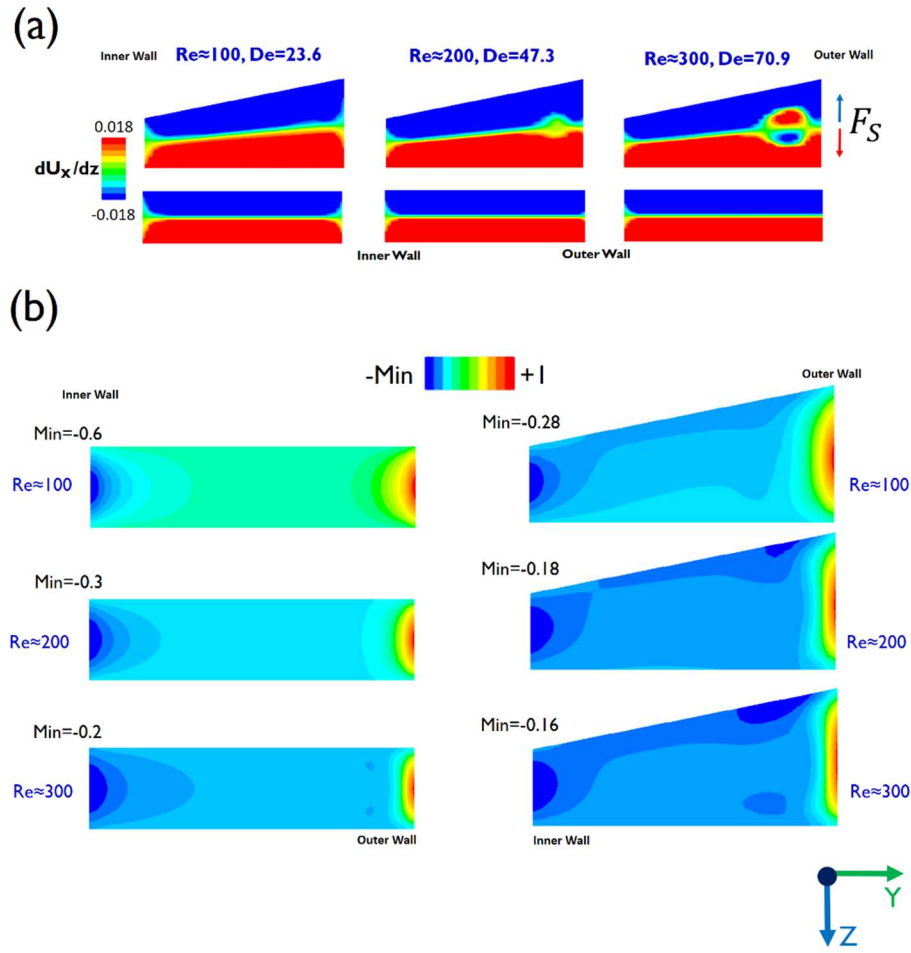


Figure S5-2 (a) Comparison of the dimensionless partial of axial velocity with respect to height of the channel ($\frac{\partial U_{axial}}{\partial z}$) at the first loop in the rectangular and trapezoid spiral (to find out the boundary where the sign of shear rate alternates, its range is lowered). There is no change in the boundary of the shear rate for the rectangular spiral when Dean magnitude increases. (b) Dimensionless derivative of axial velocity along the channel width ($\frac{\partial U_{axial}}{\partial y}$) for the rectangular and trapezoid spiral (the ratio of shear rate over the maximum shear rate for each spiral separately). Transforming the rectangular spiral to the trapezoid with large slant ($\tan(\alpha)=0.2$) results in considerably uniform shear rate field located at the inner half of channel cross-section, i.e. reduction of shear-gradient lift force field.

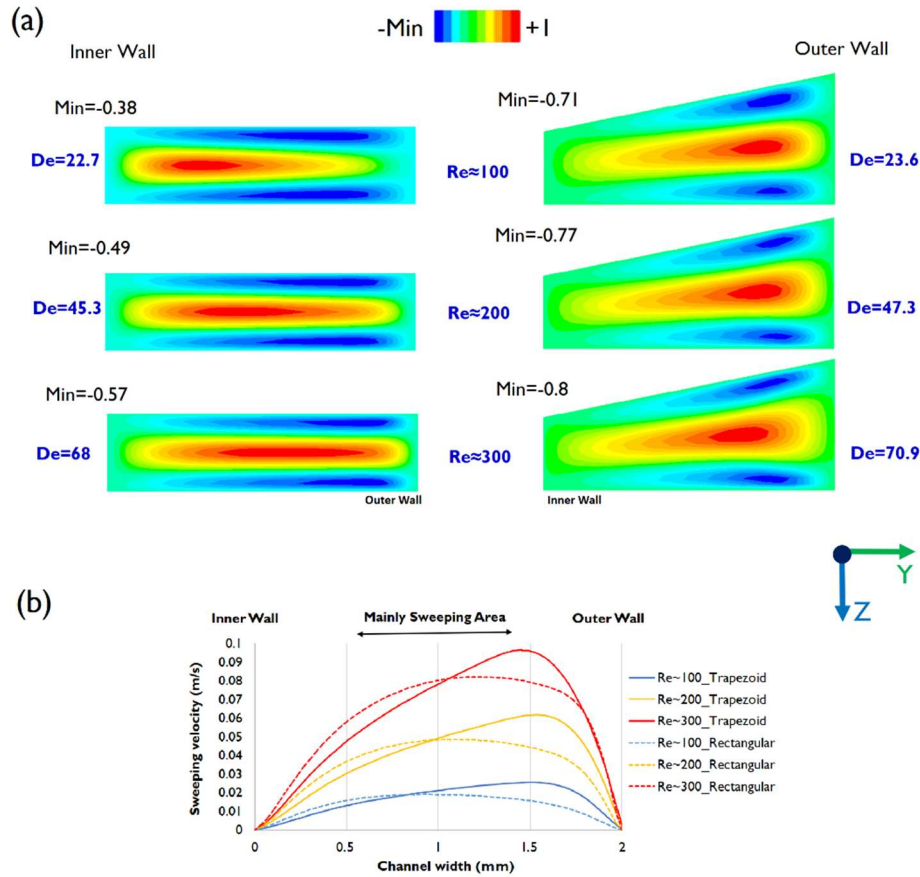


Figure S5-3 Contour of dimensionless secondary velocity (ratio of secondary velocity to maximum secondary velocity for each spiral separately) for the rectangular and trapezoid spiral. Growing De from ~ 22 to ~ 70 leads to increasing the magnitude of negative secondary flow by 50% and 12.6% for the rectangular and trapezoid spiral respectively. Also, the footprint of negative secondary flow which sweeps particles back toward inner wall in the trapezoid spiral is mainly located at the outer half of the channel cross-section compare to the rectangular spiral. In addition, the structure of secondary flow almost remains independent from De magnitude for the trapezoid spiral; however, increasing De for the rectangular spiral results in shifting and stretching of the maximum positive secondary flow toward the outer wall. (b) Comparison of positive secondary velocity of the trapezoid spiral with the rectangular spiral at mid plane. Shown here is a decrease in positive secondary velocity located at the inner half of the channel cross-section for the trapezoidal spiral (maximum -17.5 % for $Re \sim 300$ at 0.5 mm of the channel width), despite boosting maximum secondary velocity at the outer half of the channel cross-section.

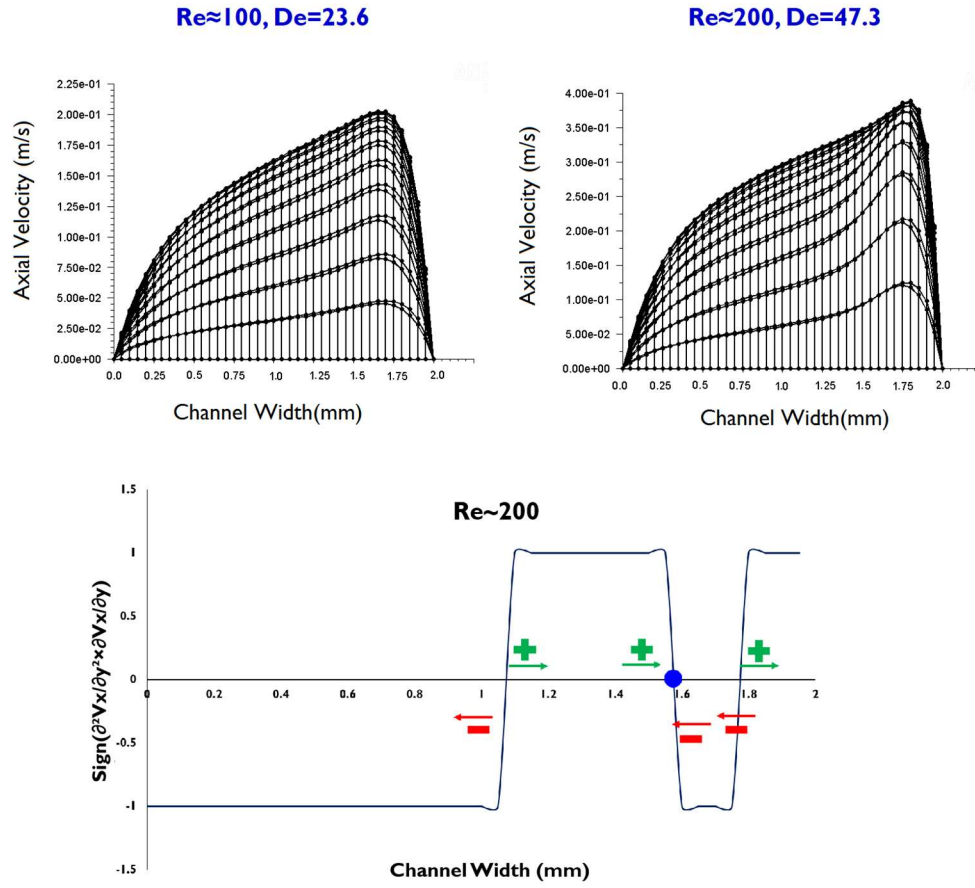


Figure S5-4 Evolution of axial velocity profile of the trapezoid spiral by increasing Dean magnitude. The inflection point is seen on the axial velocity profiles of the trapezoid spiral for high De magnitude of ≈ 47 . On other words, the secondary flow substantially changes the axial velocity profile; consequently, the shear rate field and shear-gradient lift force turns into the dominating factor which is responsible for the fast migration of $K=0.35$ particles at the first loop of the trapezoid spiral.

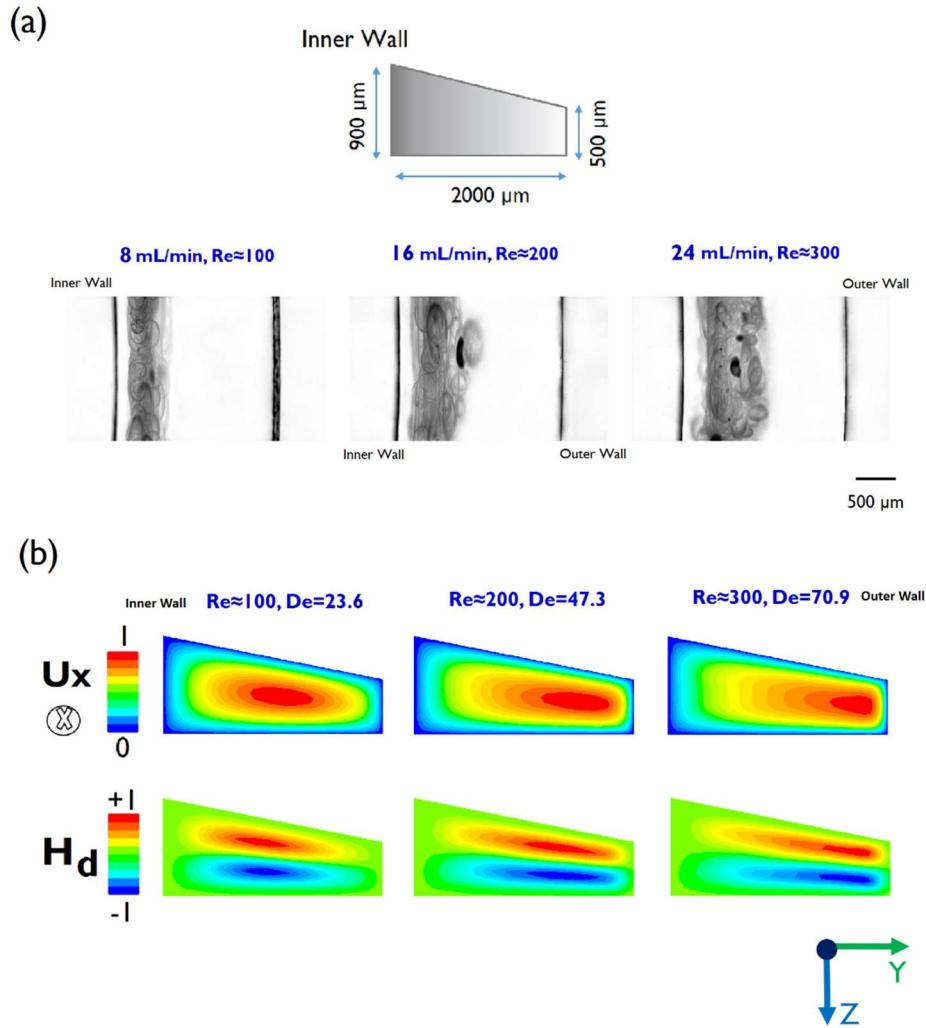


Figure S5-5 (a) Inertial focusing of $K=0.35$ particles (microcarriers) for the trapezoid spiral with larger inner wall at loop 6 ($\sim 0.1\%$ particle volume fraction). (b) Evolution of dimensionless axial velocity and helicity contours displaying Dean vortex structures for the corresponding trapezoid spiral. Growing De magnitude causes the core of maximum axial velocity and vortices shift to the outer wall. As a result, the particles band gets wider for higher $Re \geq 200$ even for low particle volume fraction of $\sim 0.1\%$.

Minimum Channel Hydraulic Diameter (D_H)

The range of particle size, a , considered here is 100 μm to 250 μm . To maintain inertial focusing and also avoid clogging channel the minimum channel height (H_{min}) is calculated as follows:

$$a=100 \mu\text{m}, \text{ max clogging ratio } K=0.4 \quad \longrightarrow \quad H_{min}=250 \mu\text{m}$$

The maximum channel hydraulic diameter when the channel aspect ratio (AR) increases to 8 and beyond is $\sim 2H$. Therefore, the corresponding minimum channel hydraulic diameter is

$$D_H = \frac{4A}{P} \approx 2H = 2 * 0.25 \text{ mm} = 0.5 \text{ mm}$$

The maximum channel hydraulic diameter for $a=100 \mu\text{m}$ particle and typical $K \sim 0.1$ ($H=1 \text{ mm}$) can theoretically reach $D_H \sim 2 \text{ mm}$. For larger particle size, D_H grows rapidly.

Table S5-1. Specifications of scaled-up rectangular and trapezoidal spiral channels

Description		AR	H_{IW} (mm)	H_{OW} (mm)	W (mm)	D_H (mm)	K	C
Rectangular	R1	4	0.5	-	2	0.8	0.35	0.219
	R2	8	0.5	-	4	0.89	0.35	0.197
	R3	4	1	-	4	1.6	0.175	0.109
Trapezoidal	T1	4	0.5	0.9	2	1.03	0.35	0.170
	T2	4	0.9	0.5	2	1.03	0.35	0.170
	T3	8	0.5	0.65	4	1.01	0.35	0.173
	T4	8	0.5	0.8	4	1.12	0.35	0.156
	T5	5.71	0.7	1	4	1.4	0.25	0.125

Larger particle sizes ($250\ \mu\text{m} < a < 500\ \mu\text{m}$)

Since channel Re number scales linearly with D_H and flow Velocity (U) – $Re \propto UD_H$ – and also Re number is itself limited ($Re < 500$), the smaller D_H is preferred to save the inertial influence ($U \propto Re/D_H$). To focus particles with $a = 300\text{--}500\ \mu\text{m}$, a rectangular channel height has to be $H \geq 1.25\ \text{mm}$ ($K < 0.4$). Figure S6 shows that even for moderate $AR = 4$ and $H = 1.25\text{--}2\ \text{mm}$, the particle confinement ratio C cannot meet the criteria $C \geq 0.2$.

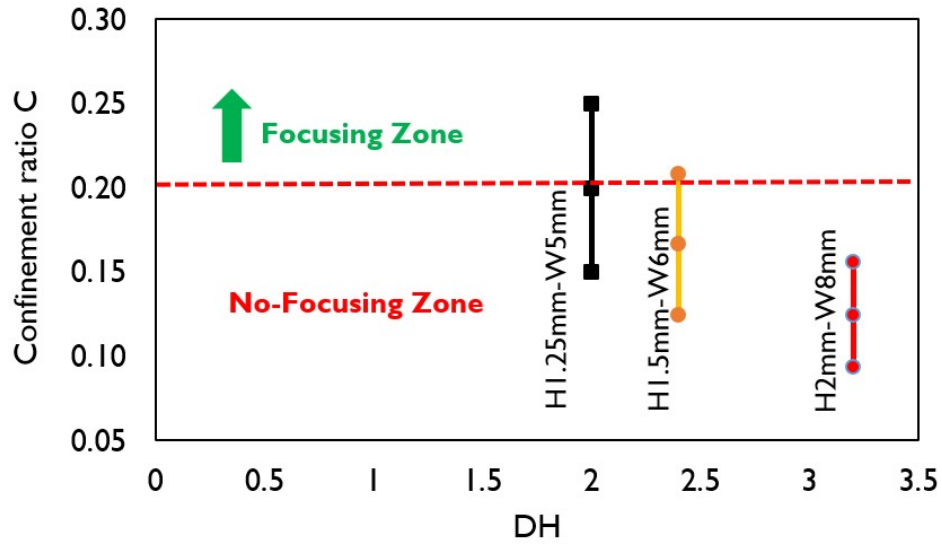


Figure S5-6 Variation of particle confinement ratio ($a = 300\text{--}500\ \mu\text{m}$) for scaled-up rectangular channels with $H = 1.25\ \text{mm}$, $H = 1.5\ \text{mm}$ and $H = 2\ \text{mm}$. The aspect ratio is $AR = 4$ for all channels. The red dash line ($C = 0.2$) displays the lower threshold for focusing at mm-scale rectangular channels.

Moreover, Figure S7 shows that the corresponding flow velocities of the scaled-up channels (at Figure 2) go below $20\ \text{cm/s}$ even at large channel $Re \sim 400$. In practice, when the inertial element of flow is hindered by large channel hydraulic diameter (although Re is high), existence of inertial focusing will be deteriorated.

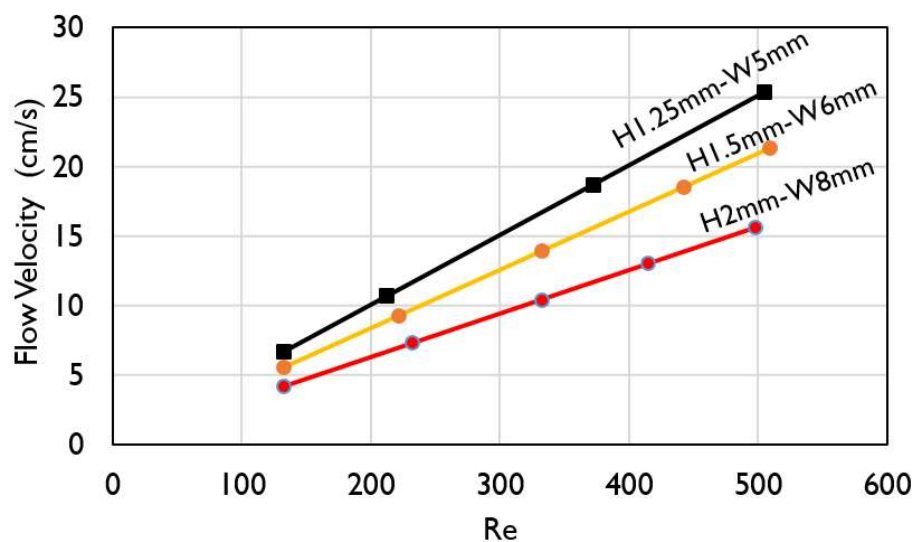


Figure S5-7 Flow velocity vs. channel Re number for channel hydraulic diameter $D_H \geq 2$ mm. Deterioration of flow velocity (inertial factor) is taken place when D_H increases ($Re < 600$). This factor determines the upper limit for inertial focusing.

Rectangular Spiral

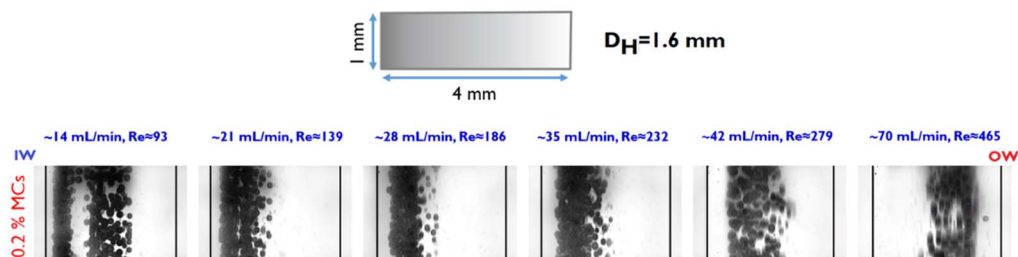


Figure S5-8 Inertial equilibrium of $K=0.175$ particles (microcarriers) for rectangular spiral with larger channel height of 1 mm ($D_H=1.6$ mm). It shows that focusing (even for low particle volume fraction ~ 0.1 - 0.2%) cannot be established except rough equilibrium at $Re \sim 186$.

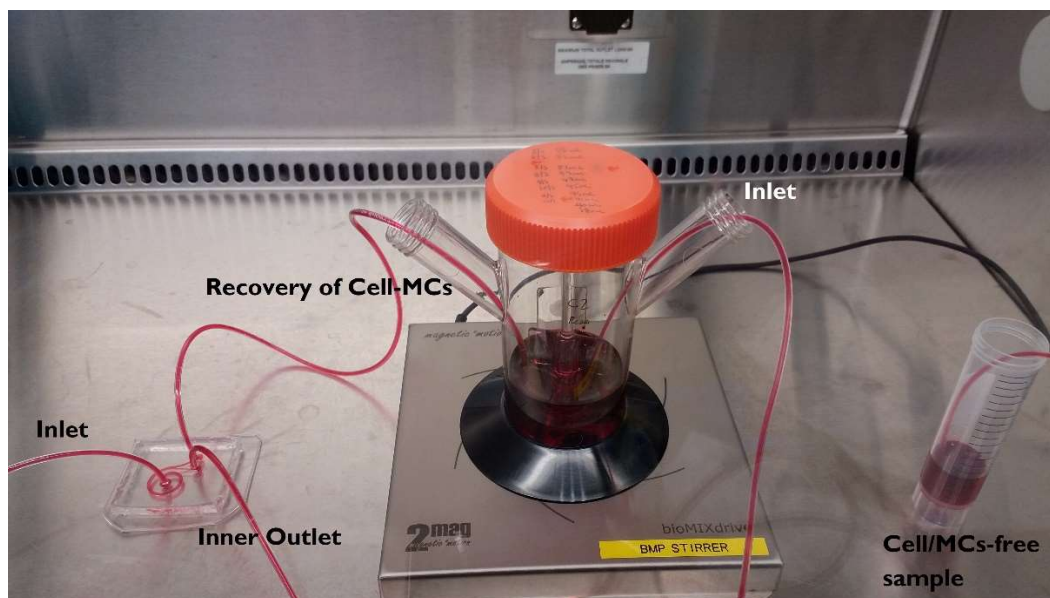


Figure S5-9 Experimental setup of cell-microcarrier suspension culture retention system. For better visualization, the system stained with red dye.

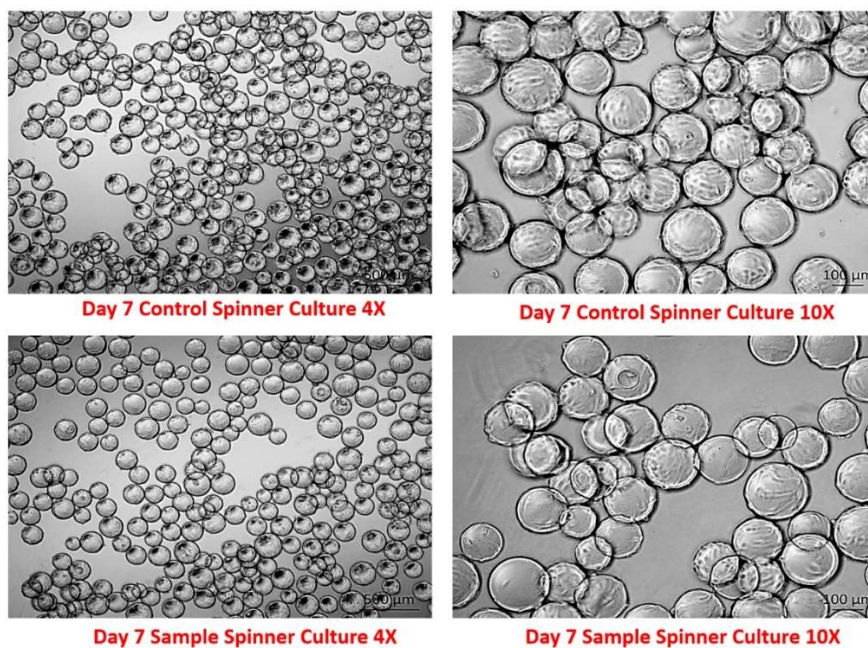


Figure S5-10 MSCs-Microcarriers spinner flask cultures (4X and 10X magnification), showing formation of Cell-MCs clumps for both culture setups.

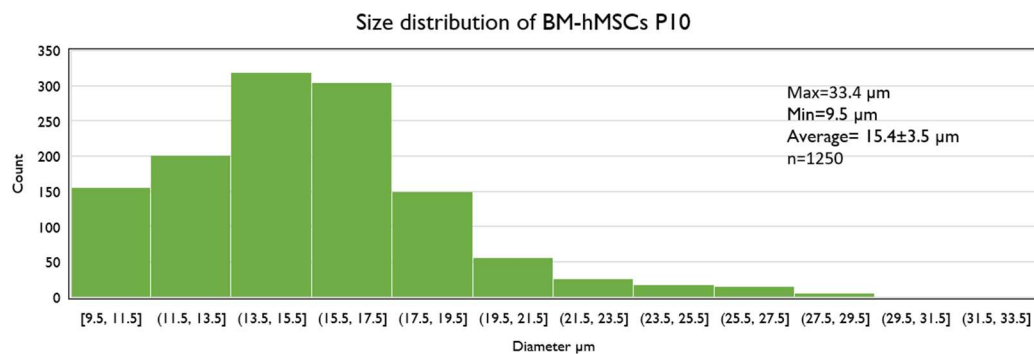
Appendix D. Supplementary Information: High-throughput Separation of Particulates Contamination from Manufactured Cell Products Using Inertial Microfluidics

Figure S6-1 Size distribution of BM-hMSCs (P10) in suspension state

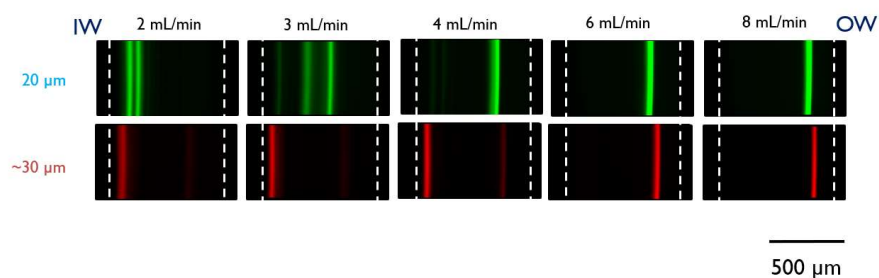
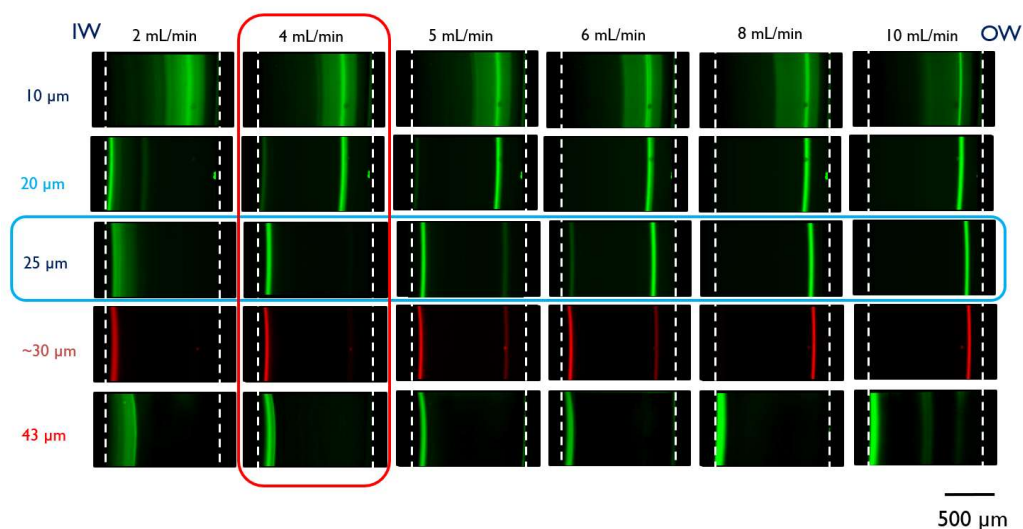
(a) Trapezoid H160-225 μm -W800 μm (AR5)(b) Trapezoid H160-260 μm -W1200 μm (AR7.5)

Figure S6-2 Inertial focusing of fluorescent particle in trapezoidal spirals with (a) AR=5 and (b) AR=7.5 with fixed $H_{IW}=160\ \mu\text{m}$ and slope of slanted wall. A separation between 20 μm and $\sim 30\ \mu\text{m}$ particle is not found using trapezoidal channels with AR lower than 10.

Trapezoid H200-300 μm -W1200 μm (AR6)

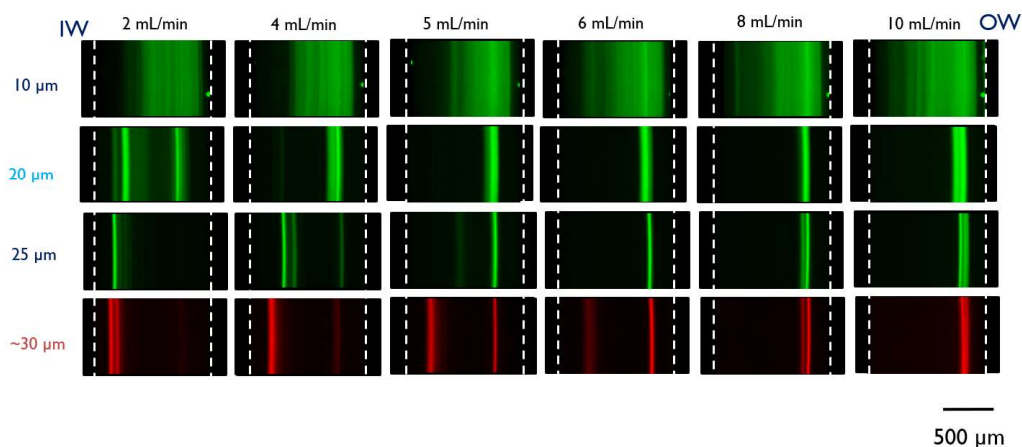


Figure S6-3 Inertial focusing of fluorescent particle in trapezoidal spiral with increased channel height to $H_{IW}=200\text{ }\mu\text{m}$, $H_{OW}=300\text{ }\mu\text{m}$ and $W=1200\text{ }\mu\text{m}$.

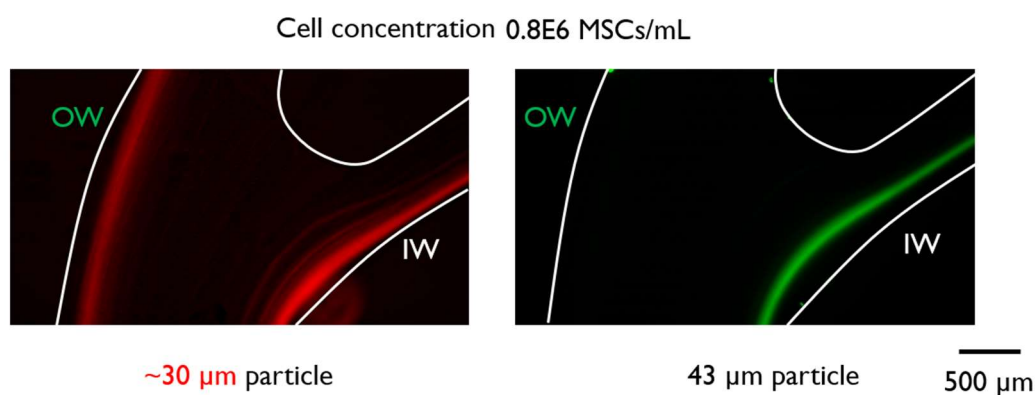


Figure S6-4 Inertial focusing of $\sim 30\text{-}\mu\text{m}$ and $43\text{-}\mu\text{m}$ fluorescent particles at flow rate of 8 mL/min in the trapezoidal spiral ($H_{IW}=160\text{ }\mu\text{m}$, $H_{OW}=290\text{ }\mu\text{m}$ and $W=1600\text{ }\mu\text{m}$) in the presence of MSCs with concentration of 0.8×10^6 cells/mL.

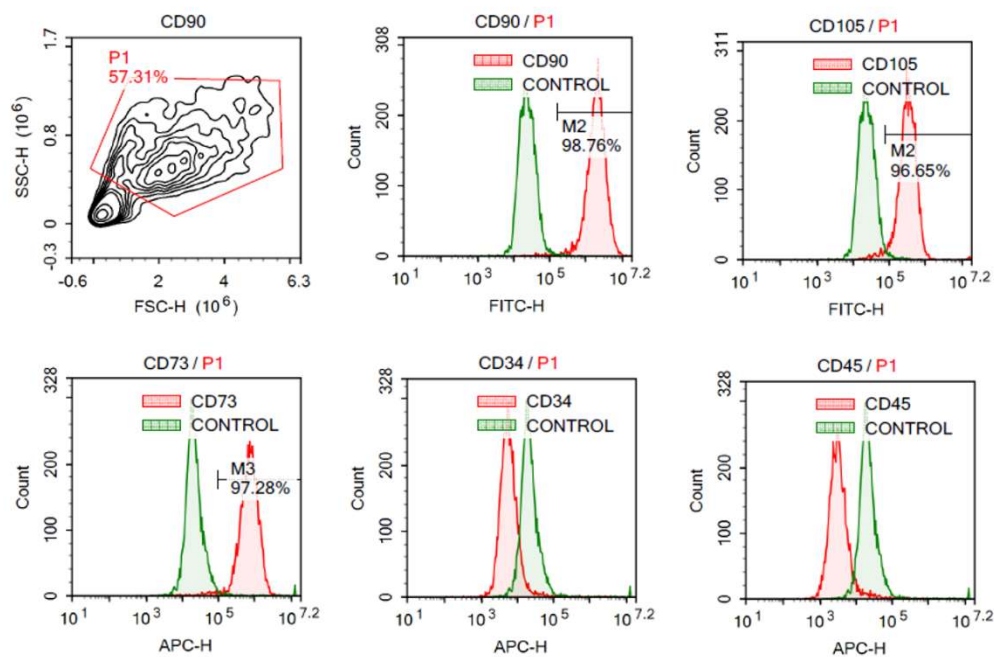


Figure S6-5 Immunophenotype of control MSCs without using the trapezoidal spiral; it shows the positive expression for CD90, CD105 and CD73 and negative expression for CD34 and CD45.